1967

Piezoresistance of n-type magnesium stannide

Leon Duane Crossman
Iowa State University

CROSSMAN, Leon Duane, 1939-
PIEZORESISTANCE OF N-TYPE MAGNESIUM STANNIDE.

Iowa State University, Ph.D., 1967
Physics, solid state

University Microfilms, Inc., Ann Arbor, Michigan

PIEZORESISTANCE OF N-TYPE MAGNESIUM STANNIDE

by

Leon Duane Crossman

A Dissertation Submitted to the
Graduate Faculty in Partial Fulfillment of
The Requirements for the Degree of
DOCTOR OF PHILOSOPHY

Major Subject: Physics

Approved:

Signature was redacted for privacy.

In Charge of Major Work

Signature was redacted for privacy.

Head of Major Department

Signature was redacted for privacy.

Dean of Graduate College

Iowa State University
Of Science and Technology
Ames, Iowa

1967

TABLE OF CONTENTS

LIST OF TABLES

LIST OF TABLES (Continued)

LIST OF FIGURES

LIST OF FIGURES (Continued)

LIST OF FIGURES (Continued)

LIST OF FIGURES (Continued)

LIST OF FIGURES (Continued)

ABSTRACT

The piezoresistance tensor components for n-type Mg_2Sn have been measured from 50 to 300°K. The piezoresistance effect in Mg_2Sn is larger than the piezoresistance effect in germanium or silicon. From these measurements and the elastic constants of Davis *et al.*, the elastoresistance tensor components were obtained and found to satisfy $m_{11} = -2m_{12}$, m_{11} large and m_{44} small, in the temperature range 50 to 200°K. These relationships confirm that n-type Mg_2Sn is a many-valley semiconductor with constant energy ellipsoids in the <100> direction. The fact that m_{11} and m_{12} were both linear in the temperature range 60-175°K indicates that inter-valley scattering is unimportant in the extrinsic temperature region. The small value of the volume coefficient, $(m_{11} + 2m_{12})/3$, indicates that carrier mobility in n-type Mg_2Sn is relatively insensitive to changes in sample volume. The deformation potential was determined from a combination of these piezoresistance results and Umeda's magnetoresistance data and found to satisfy the relation $\Xi_u = \Xi_u^o(1+\alpha T)$, where $\Xi_u^o = 10.1$ ev and $\alpha = (-4.3 \pm 0.6) \times 10^{-4}\ ^oK^{-1}$. High stress piezoresistance measurements yielded a deformation potential of $\Xi_u = 18$ ev and mobility anisotropy of $K = 2.65$ at 77.4°K. Umeda obtained $K = 3.51$. A possible qualitative explanation of these differences can be given in terms of a change with stress of the position of the donor levels with respect to the conduction band.

I. INTRODUCTION

Before 1954 the semiconductors which had been extensively studied were assumed to have conduction band energy structures with an energy minimum at $\underline{k} = 0$ in wave vector space and with spherical constant energy surfaces. However the magnetoresistance and cyclotron resonance measurements made on silicon and germanium in the early part of the 1950's showed a strong directional dependence. A brief review of this early work was published by Kittel (37). Then in 1954 Abeles and Meiboom (1) presented a transport theory based on a model where the conduction band minima were not located at $\underline{k} = 0$ in wave vector space and the constant energy surfaces were ellipsoidal rather than spherical. This theory satisfactorily explained their observed magnetoresistance results. At the same time, Smith (64) reported the first observed directional dependence of resistivity as a function of applied stress. Smith observed large changes in the resistivity of silicon and germanium when oriented samples of these semiconductors were subjected to a uniaxial stress. Based on the simple model, these large stress induced effects could not be explained in terms of strain induced changes in the mobility or in terms of strain induced changes in the energy gap.

In 1955 Herring (21) extended Abeles and Meiboom's work to give a satisfactory explanation of the observed transport properties of silicon and germanium. Herring explained the

directional dependent effects in terms of a many-valley model; where, as in Abeles and Meiboom's model, the conduction energy minima in $\underline{k}$-space were not located at $\underline{k} = 0$ and where the constant energy surfaces were ellipsoidal rather than spherical. The many-valley model of Herring (21) is illustrated in Fig. 1 along with the simple model.

Herring applied the idea of strain induced shifts in the conduction band to explain the large stress induced effects observed in silicon and germanium. He showed that a stress induced change in resistivity depended on three mechanisms; 1) the degree to which the valleys were repopulated, 2) the change in group velocity of the electrons and 3) the change in relaxation times of the electrons. The change in resistivity caused by the last two mechanisms was shown to be negligible when compared to the first. Herring's treatment was restricted to semiconductors in the extrinsic temperature region.

Herring (21) explained the large stress induced effect in silicon by assuming that silicon was a many-valley semiconductor with valleys in the <100> directions. The application of a uniaxial tension stress in the [100] direction, as shown in Fig. 2, shifts the x-valleys upward, while y-valleys are shifted downward. There is a transfer of electrons from x-valleys into y-valleys. The effect of this transfer is shown in Fig. 2 by the dashed curves. In the stressed state, the mobility anisotropy in the y-valleys dominates. The

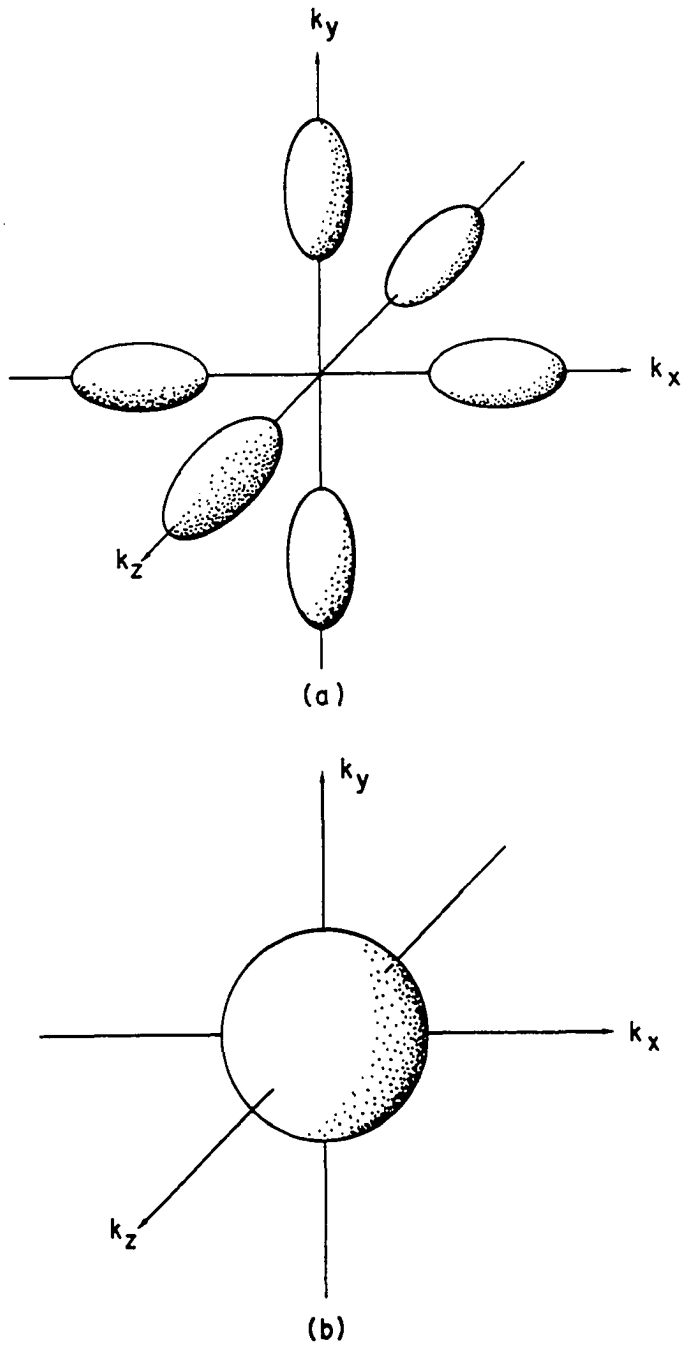

Figure 1. Schematic diagram of (a) Herring's (21) many-valley model with constant energy ellipsoids in the <100> direction and (b) the simple model.

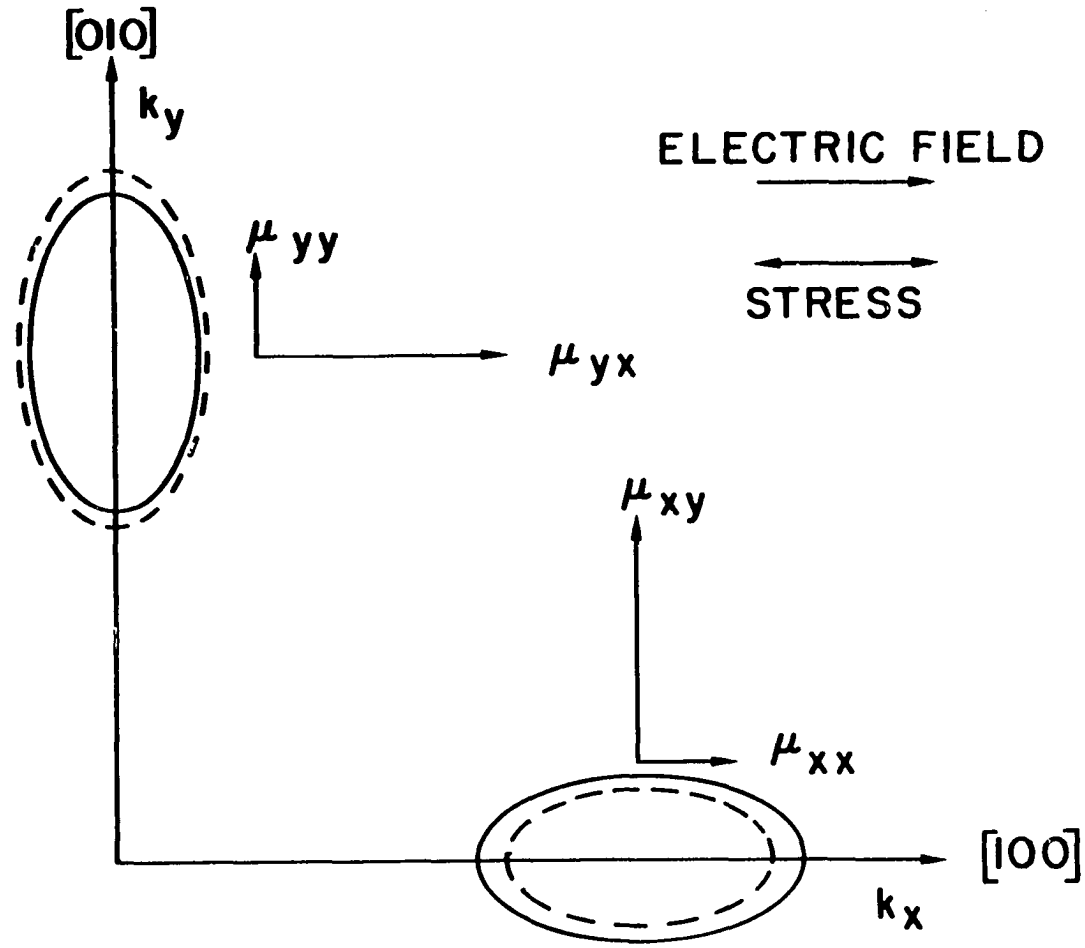

Figure 2. Schematic diagram showing the effect of stress on the constant energy ellipsoids [Figure 2 of Smith's early paper (64)]. The solid line represents the valleys before the application of a stress. The dashed lines represent the valleys after the application of the stress shown in the diagram. The mobility anisotropy is indicated by the arrows.

total mobility in the x-direction increases; causing the resistivity in the x-direction to decrease.

When Smith (64) stressed a silicon sample in the [100] direction he observed $\Delta\rho/\rho$ to be negative (as expected from Herring's model) where ρ is the unstressed resistivity, $\Delta\rho = (\rho_L - \rho)$, and ρ_L is the stressed resistivity. Herring's model also predicted that if silicon was stressed along a diagonal ([111] direction), all valleys would be affected in the same fashion and a small $\Delta\rho/\rho$ would be observed. Smith (64) reported values of $\Delta\rho/\rho$ which were more than an order of magnitude smaller than the [100] values when silicon was stressed in the [111] direction. Smith's results also indicated a <111> many-valley model for germanium.

Herring and Vogt (22) later extended Herring's calculations to include anisotropic relaxation times as well as anisotropic masses and mobilities.

Interpretation of piezoresistance measurements in terms of band structure is independent of the type semiconductor (simple or many-valley), of the scattering mechanisms and of the number of carriers present in the material [see Herring (21)]. Thus, in contrast with most other measurements, piezoresistance measurements can be used to obtain information about band structure in materials of intermediate purity. Magnetoresistance measurements also yield information about band structure in materials of intermediate purity, but they

require more homogeneous crystals than do piezoresistance measurements. As a result, piezoresistance measurements have been used extensively to determine the electronic structure of the intermediate purity semiconductors. Table 1 shows the results of piezoresistance measurements on several cubic semiconducting materials.

Piezoresistance theory has been extended to low symmetry crystals by Drabble and Wolfe (13), Smith (63), and Keyes (33, 34). The semiconductors cadmium antimonide (32,68), rutile (5,24), bismuth telluride (25) and antimony telluride (4) have all been studied using piezoresistance techniques.

At low stresses, readily interpretable results can be obtained on nondegenerate, extrinsic samples. By deliberately making a semiconductor degenerate and extending the piezoresistance measurements to high stress ($\chi > 10^9$ dynes/cm^2) one can obtain information about impurity activation energies. However, the experiments require good control over the number and type of impurities present in the semiconductor. At the present time only silicon (69) and germanium (10,11,30,31,52) have been studied with degenerate materials.

If piezoresistance measurements on non-degenerate semiconductors are extended to high stresses, it is possible to determine both the deformation potential and mobility anisotropy (2,33). One requirement is that the high stress measurements take place in a temperature region where acoustic

Table 1. Results of piezoresistance measurements on cubic semiconductors; references are given in parenthesis

Material	Band structure	Deformation potential (ev)
n-Ge	<111> valleys (17,35,39,48,64,65)	19.2 (10,11)
p-Ge	k=0 maximum (39,48,64)	
n-Si	<100> valleys (48,64)	8.3 (2)
p-Si	k=0 maximum (48,64)	
n-InSb	<000> minimum (8,53)	
p-InSb	like Ge (36,72)	
n-GaSb	<000> minimum, <111> valleys (36,56)	20 (56)
p-GaSb	like Ge (70)	
n-AlSb	<100> valleys (20)	5 (20)
p-AlSb	like Ge (20)	
n-PbTe	<111> valleys (26)	5.5 (26)
p-PbTe	<111> maxima (23,26,27)	8 (26,27)
n-Mg_2Sn	<100> valleys (present)	10.1(present)
p-Mg_2Sn	like Ge (29)	
p-ZnTe	like Ge (59,61)	
p-PbSe	like Ge (26)	
n-CdTe	<000> minimum (60)	
n-InP	<000> minimum (57)	
n-PbS	<111> valleys (15)	6.9 (15)
n-GaAs	<000> minimum (58,62)	
n-InAs	<000>minimum (73)	
n-Mg_2Si	<100> valleys (75)	
n-$SrTiO_3$	<000> minimum (71)	

mode scattering is dominant.

The purpose of the present investigation is to; 1) measure the piezoresistance tensor components of the semiconductor Mg_2Sn to determine whether or not it is a many-valley semiconductor, and if so, in what directions do the valleys lie, 2) combine the results of these piezoresistance measurements with the results of magnetoresistance measurements made by Umeda (74) to determine the deformation potential and 3) extend the piezoresistance measurements to high stress to determine an independent value for the deformation potential and mobility anisotropy.

II. MAGNESIUM STANNIDE

Magnesium stannide is a II-IV compound semiconductor of the Mg_2X family, where X can be Si, Ge, Sn or Pb. The Mg_2X compounds are cubic with the fluorite structure. A unit cell of Mg_2Sn is shown in Fig. 3. The lattice constant of Mg_2Sn is 6.7630 Å at 26°C (66) with a temperature coefficient[1] of 9.9×10^{-6} (T^{-1}) at 300°K.

Many of the electrical, optical and thermal properties of Mg_2Sn have already been studied. A good review of the literature has been given by Martin (46). A brief summary along with the appropriate references will be given here.

Reported values for the energy gap, mobility and effective masses of Mg_2Sn are given in Table 2 together with the names of the investigators and the experimental techniques which they employed. The accepted value for the energy gap of Mg_2Sn is 0.34 ev at 0°K. However, as can be seen in Table 2, there is a factor of two difference between the energy gap obtained from electrical and optical studies. This difference is not understood at the present time. The recent Hall measurements on Mg_2Sn show a $T^{-1.5}$ temperature dependence for the Hall mobility in the extrinsic temperature region, which

---

[1]Shanks, H. R., Iowa State University, Ames, Iowa. Private communication. 1966.

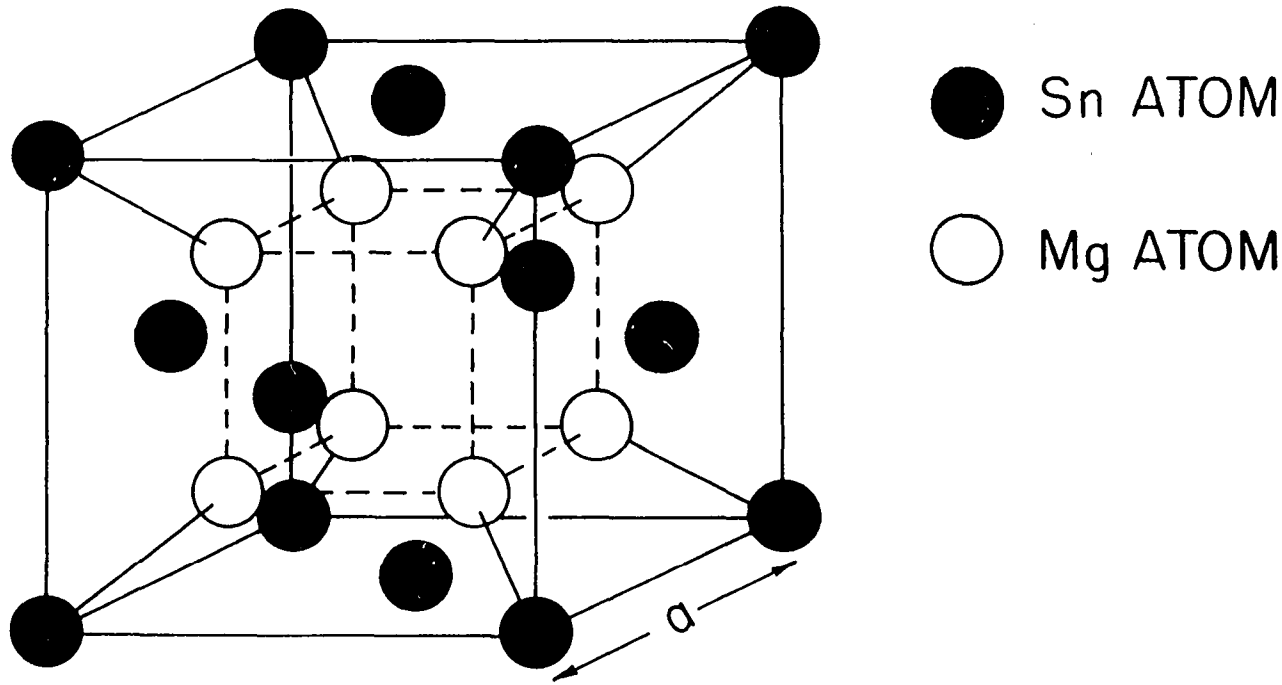

Figure 3. Crystal structure of Mg_2Sn.

Table 2. Results of some previous studies on the transport properties of Mg_2Sn

Investigator	Energy gap Method	Value at 0^oK (ev)	Mobility Intrinsic temperature dependence of mobility	Mobility Extrinsic temperature dependence of mobility	Mobility ratio (μ_e/μ_h)	Effective masses Electron (electron rest mass)	Effective masses Hole (electron rest mass)
Winkler	Resistivity Hall effect Seebeck effect	0.36	$T^{-2.5}$		1.4	2.3	2.6
Blunt et al.	Hall effect optical	0.33		$T^{-2.2}$	1.23	1.2	1.3
Nelson	Hall effect	0.36					
Lawson et al.	Hall effect optical	0.34 0.18					
Lipson & Kahan	Optical	0.18			1.23	1.2	1.3
Geick et al.	Optical		$T^{-2.5}$	$T^{-1.5}$			
Licter	Hall effect		$T^{-2.5}$	$T^{-1.7}$	1.21		

is consistent with acoustic mode scattering. The low temperature (4-77°K) resistivity was investigated by Frederikse et al. (16).

Busch and Schneider (9) measured the thermal conductivity of Mg_2Sn from 73-437°K, while Martin (46) measured the thermal conductivity from 4.2-300°K. Busch and Schneider's results did not indicate an electronic contribution to the thermal conductivity. Martin found that above 150°K the thermal conductivity showed a T^{-1} temperature dependence, which is characteristic of lattice thermal conductivity.

The Seebeck effect was studied by Boltacks (7), Winkler (76) and Martin (46). Some n-type Mg_2Sn samples (46) were found to have a Seebeck effect as high as 3000 μv/deg at low temperatures.

Davis et al. (12) determined the elastic constants in the temperature range 77-300°K. The room temperature elastic constants are, $C_{11} = 8.24 \times 10^{-11}$, $C_{12} = 2.08 \times 10^{-11}$, and $C_{44} = 3.87 \times 10^{-11}$ dynes/cm^2. A small temperature variation in the elastic constants between 300 and 77°K was observed. Also Davis et al. (12) found that the phonon dispersion curves calculated from a shell model gave the best fit to the Debye temperature versus temperature curve obtained from the heat capacity measurements of Jelinek et al. (28). Jelinek et al. report a Debye temperature of 310°K at 77°K for Mg_2Sn.

Infrared reflectivity measurements of McWilliams and

Lynch (45) on Mg_2Sn indicate a high frequency dielectric constant of $\varepsilon_\infty = 17.0$.

The magnetoresistance measurements of Umeda (74) indicate that n-type Mg_2Sn is a many-valley semiconductor with valleys in the <100> direction. Umeda also reported that his results on p-type Mg_2Sn suggested a many-valley valence band with maxima in the <100> directions. Although he admitted that his results were not conclusive in regard to the existence of a many-valley valence band. However, Kaiser and Kearney (29) report that their piezoresistance results on p-type Mg_2Sn show a valence band similar to germanium. Thus, there is a conflict between the magnetoresistance and piezoresistance results as to whether there is a many-valley valence band in Mg_2Sn or not.

Umeda (74) found a mobility anisotropy ratio K = 3.51 at 77.4°K for samples with a carrier concentration of 1.5×10^{16} carriers/cm^3. For his sample with a carrier concentration of 9×10^{17} carriers/cm^3 he found K = 2.8.

III. THEORY

A. Piezoresistance Theory

In general, the physical properties of a solid depend on its state of strain. In particular, the electrical resistivity of a solid is a function of applied stress. The change in resistivity with the application of a stress is called the piezoresistance effect. The object of this section is to develop a mathematical description of the peizoresistance effect and to show how it can be used to determine the direction of constant energy ellipsoids in a many-valley semiconductor. The development will be limited to cubic crystals and follows the work of Smith (64) and Keyes (33).

The starting point for the development of piezoresistance theory is Ohm's law,

$$\underline{E} = \bar{\rho} \cdot \underline{J}, \tag{1}$$

where $\underline{E}$ is the electric field, $\bar{\rho}$ the resistivity and $\underline{J}$ the current density. For cubic symmetry ρ is a scaler in the unstrained case. However, under an applied strain the cubic symmetry may be destroyed and $\bar{\rho}$ must be considered as a second rank tensor. Equation 1 can be written as,

$$E_k = \sum_l \rho_{kl} j_l \cdot \tag{2}$$

If, in the special case of constant current density, which applies in the experiment described here; the resistivity changes because of an applied stress, Eqn. 2 becomes

$$\delta E_k = \sum_l \delta \rho_{kl} j_l , \qquad (3)$$

where δE_k is the change in electric field and $\delta \rho_{kl}$ is the change in resistivity. For convenience, Eqn. 3 is divided by the unstrained value of the resistivity ρ, which is a scaler. Consequently

$$\frac{\delta E_k}{\rho} = \sum_l \frac{\delta \rho_{kl}}{\rho} j_l = \sum_l \Delta_{kl} j_l , \qquad (4)$$

where

$$\Delta_{kl} = \frac{\delta \rho_{kl}}{\rho} .$$

Since a change in sample resistivity results from the application of a stress, the Δ_{kl} are related to the stress by the piezoresistance tensor,

$$\Delta_{kl} = \sum_{mn} \pi_{klmn} \chi_{mn} , \qquad (5)$$

where χ_{mn} are components of the stress tensor and π_{klmn} are components of the fourth rank piezoresistance tensor. Equation 5 holds for a general reference axis, however it will be used in the following development for a system with the cubic axes in the [100], [010] and [001] directions.

Since the second rank tensors presented here are used in connection with a cubic system, the tensors are symmetric about the diagonal. Equation 5 can be simplified by the following notation [see, for example, Keyes (33) and Smith (64)],

$$\begin{pmatrix} 11 & 12 & 13 \\ 21 & 22 & 23 \\ 31 & 32 & 33 \end{pmatrix} = \begin{pmatrix} 1 & 6 & 5 \\ 6 & 2 & 4 \\ 5 & 4 & 3 \end{pmatrix}. \qquad (6)$$

With the above simplification, the second rank resistivity and stress tensors become 1 x 6 column matrices.

$$\Delta_{kl} = \begin{pmatrix} \Delta_{11} \\ \Delta_{22} \\ \Delta_{33} \\ \Delta_{23} \\ \Delta_{13} \\ \Delta_{12} \end{pmatrix} \qquad \chi_{mn} = \begin{pmatrix} \chi_{11} \\ \chi_{22} \\ \chi_{33} \\ \chi_{23} \\ \chi_{13} \\ \chi_{12} \end{pmatrix} \qquad (7)$$

The piezoresistance tensor components are then written as [see, for example, Keyes (33) and Smith (63,64)],

$$\begin{aligned} \pi_{1111} &= \pi_{11}, \\ \pi_{1122} &= \pi_{12}, \text{ etc.} \end{aligned} \qquad (8)$$

A factor of two must be introduced if the second index of $\pi_{\omega\lambda}$ is 4, 5 or 6; for example

$$\begin{aligned} \pi_{14} &= 2\pi_{1132}, \\ \pi_{26} &= 2\pi_{2212}, \text{ etc.} \end{aligned} \qquad (9)$$

For cubic systems, the fourth rank piezoresistance tensor reduces to

$$\pi_{\omega\lambda} = \begin{pmatrix} \pi_{11} & \pi_{12} & \pi_{12} & 0 & 0 & 0 \\ \pi_{12} & \pi_{11} & \pi_{12} & 0 & 0 & 0 \\ \pi_{12} & \pi_{12} & \pi_{11} & 0 & 0 & 0 \\ 0 & 0 & 0 & \pi_{44} & 0 & 0 \\ 0 & 0 & 0 & 0 & \pi_{44} & 0 \\ 0 & 0 & 0 & 0 & 0 & \pi_{44} \end{pmatrix}. \tag{10}$$

With the above notation Eqn. 5 becomes,

$$\Delta_\omega = \sum_{\lambda=1}^{6} \pi_{\omega\lambda} X_\lambda \tag{11}$$

In order to determine where the valleys of a many-valley semiconductor are located, one must experimentally find values for the π's. To determine the three π's in Eqn. 10, three independent measurements must be made. There are only two simple types of stress which can be conveniently applied to a solid [see Keyes (33)]: a) hydrostatic stress and b) uniaxial tension or compression.

Hydrostatic stress applied to a crystal does not change the crystal symmetry. It can be represented (33) by

$$\bar{X} = P\bar{1}, \tag{12}$$

where P is the magnitude of the applied stress. When this is substituted in Eqn. 11, one has

$$\Delta_\omega = P \sum_{\lambda=1}^{6} \pi_{\omega\lambda} . \tag{13}$$

Under a hydrostatic stress the resistivity matrix is still diagonal with all diagonal components equal; that is,

$\Delta_1 = \Delta_2 = \Delta_3 = \Delta$. Equation 13 becomes

$$\frac{\Delta\rho}{\rho P} = \pi_{11} + 2\pi_{12} \cdot \qquad (14)$$

Hydrostatic pressure measurements can be used to determine the volume effect $\pi_{11} + 2\pi_{12}$. In the experiment described here, hydrostatic measurements were not made.

In the case of uniaxial stress there are three different stress-electrode configurations that can be employed to determine the piezoresistance tensor components. In one of these arrangements (longitudinal), the stress and the resistance probes are parallel to each other; in the other two arrangements (transverse) they are at right angles. A minimum of two configurations must be used to determine a complete set of piezoresistance tensor components.

Figure 4a shows the longitudinal arrangement. This arrangement permits the most accurate measurements and allows a direct determination of the resistivity, ρ, as well as the change in resistivity, $\Delta\rho$.

Figure 4b shows one transverse arrangement. For this configuration, a large area low resistance electrical contact must be made to the sample. To minimize end effects the length of the area contact should be at least three times as great as the width of the contact. In addition, the contact should not extend to the ends of the sample. As for the longitudinal measurement, this transverse configuration allows one to determine both the resistivity and the change in resistivity

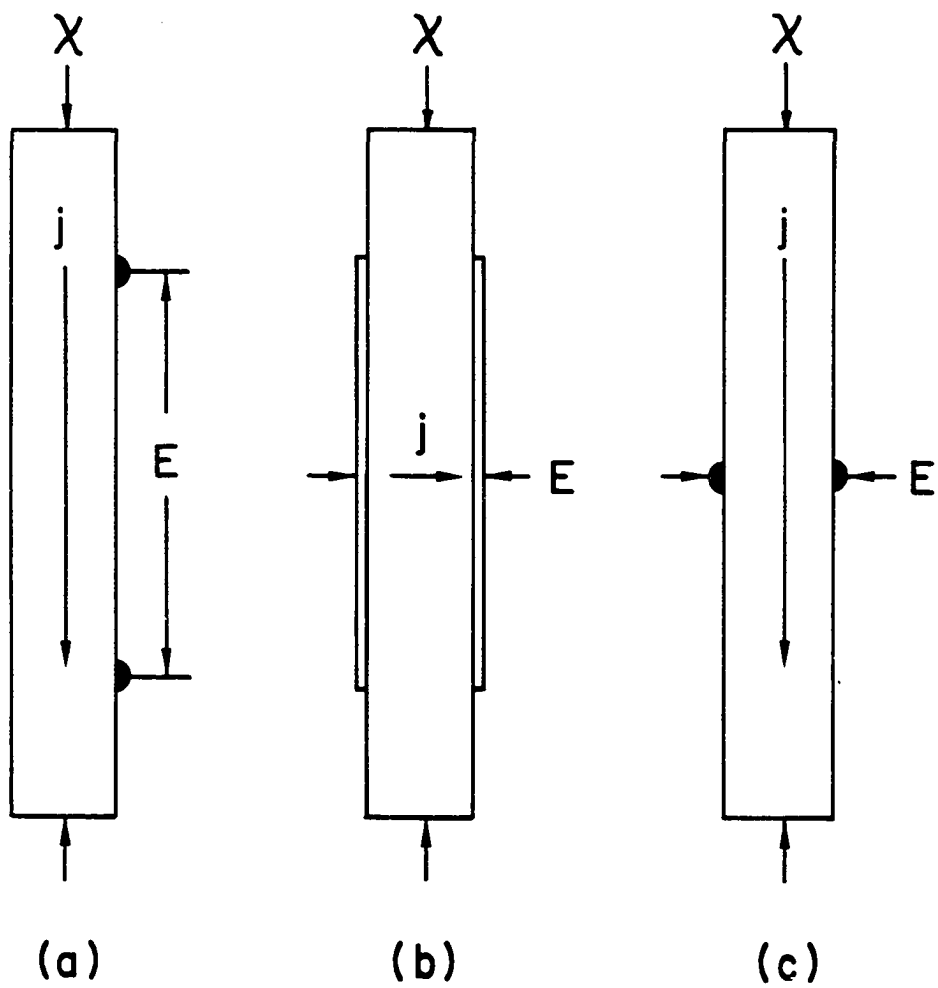

Figure 4. Three possible uniaxial stress-electrode configurations that can be employed to determine the piezoresistance tensor components [Fig. 1 in Keyes (33)]. The longitudinal arrangement is given in (a) and the two possible transverse arrangements are given in (b) and (c).

with the same set of electrodes.

Figure 4c shows the other transverse arrangement. However, this arrangement does not lend itself to making simultaneous resistivity and change in resistivity measurements. In this configuration the resistivity must be measured with a set of electrodes different than those used to measure the change in resistivity. If the sample is inhomogeneous, the measured sample resistivity is likely to be different than the resistivity at the point where the change in resistivity was measured. Therefore, we did not employ this arrangement in our measurements. A complete discussion of the different stress-electrode arrangements is given in an article by Keyes (33).

The sample orientations which were used in connection with the various stress-electrode arrangements are shown in Fig. 5. The configurations 5a,b,c were employed for our determination of the three piezoresistance tensor components. Configurations 5d and 5e were used for an internal check on the other three.

For configuration 5a the applied stress is χ_{11} and the fractional change in resistivity is Δ_{11}; that is, $\Delta\rho/\rho$ is measured parallel to the stress. Equation 5 becomes

$$\Delta_{11} = \pi_{1111}\,\chi_{11},$$

and according to the notation of Eqn.8 and the definition of Δ from Eqn. 4,

$$\frac{\Delta\rho}{\rho\chi} = \pi_{11}. \qquad (15)$$

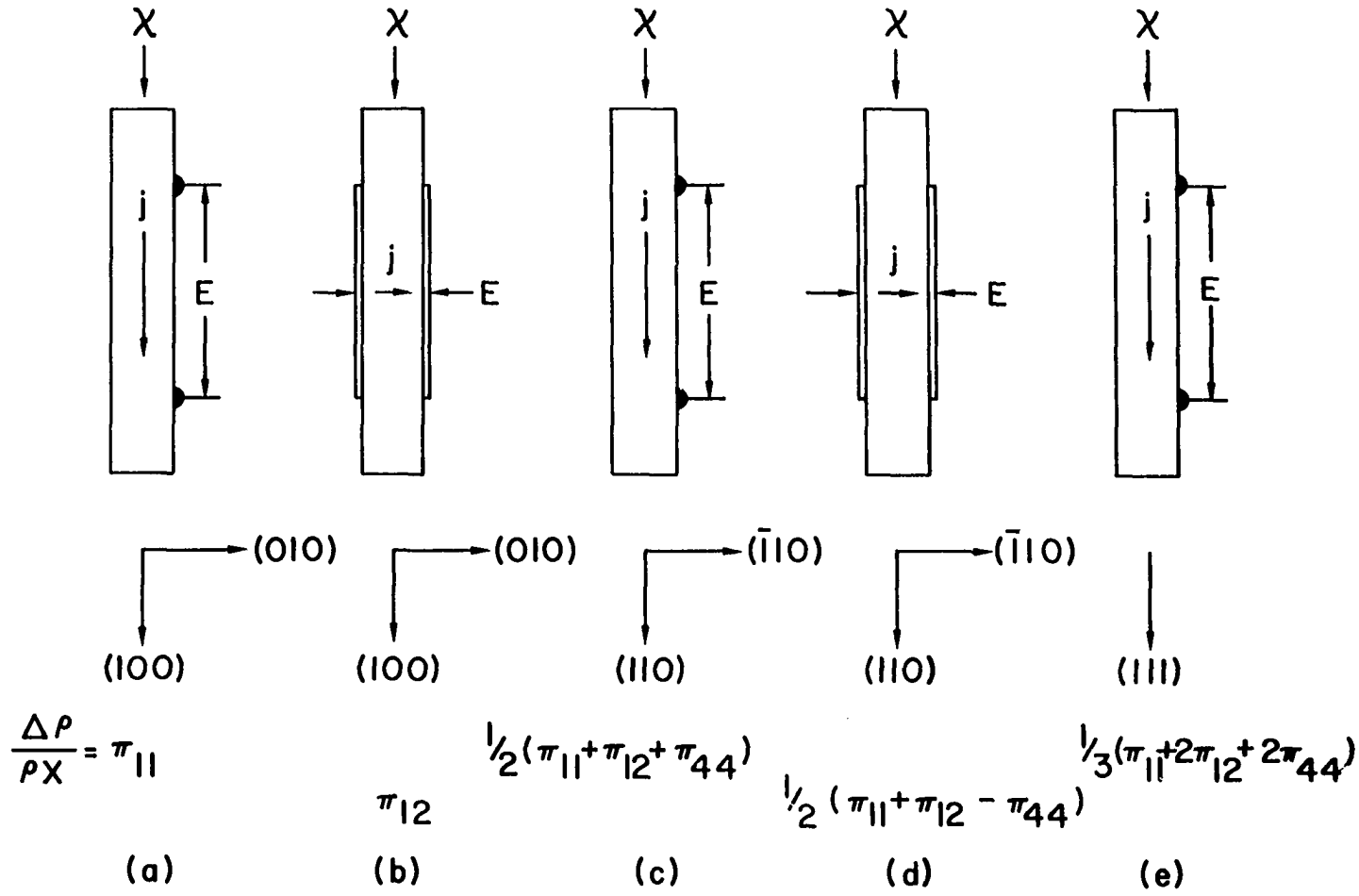

Figure 5. Sample orientations which were employed in connection with the various stress-electrode configurations. Orientations (a), (b), and (c) were used to determine the three piezoresistance tensor components, while orientations (d) and (e) were used for an internal check on the other three.

Similarly, one finds

$$\frac{\Delta\rho}{\rho\chi} = \pi_{12} \tag{16}$$

when the change in resistivity is measured perpendicular to the applied stress on a [100] oriented sample (Fig. 5b).

To determine the tensor component obtained from configuration 5c, the piezoresistance tensor (Eqn. 10) must be transformed to a new coordinate system, obtained by rotating the old coordinate system about the [100] axis. The $[0\bar{1}1]$, [011] and [100] directions are used as the reference axes in the new system. The transformation is given by

$$\pi'_{ijkl} = \sum_{m,n,p,q} C_{im}C_{jn}C_{p}C_{lq}\pi_{mnpq}, \tag{17}$$

where the C_{rs} are components of the rotation matrix about the [100] axis of rotation. For configuration 5c the longitudinal electrode arrangement allows a measurement of Δ_{11} when a stress χ_{11} is applied. Equation 5 becomes

$$\Delta_{11} = \pi'_{1111}\,\chi_{11}. \tag{18}$$

where Eqn.17 gives $\pi'_{1111} = \frac{1}{2}(\pi_{11} + \pi_{12} + \pi_{44})$. Thus, configuration 5c allows the measurement of

$$\frac{\Delta\rho}{\rho\chi} = \tfrac{1}{2}(\pi_{11} + \pi_{12} + \pi_{44}). \tag{19}$$

In a similar fashion, configuration 5d allows a measurement of the change in resistivity perpendicular to the applied stress on a [110] oriented sample. Using Eqn. 17 one obtains, for configuration 5d,

$$\frac{\Delta\rho}{\rho\chi} = \tfrac{1}{2}(\pi_{11} + \pi_{12} - \pi_{44}). \tag{20}$$

Similarly, configuration 5e allows the measurement of

$$\frac{\Delta\rho}{\rho\chi} = 1/3(\pi_{11} + 2\pi_{12} + 2\pi_{44}). \qquad (21)$$

Other sample configurations can also be used to determine the piezoresistance tensor components. Mason and Thurston (47) have derived a general expression for $\Delta\rho/\rho\chi$ in cubic crystals. For longitudinal measurements,

$$\left(\frac{\Delta\rho}{\rho\chi}\right)_l = \pi_{11}-2(\pi_{11}-\pi_{12}-\pi_{44})(l_1^2m_1^2+l_1^2n_1^2+m_1^2n_1^2) \qquad (22)$$

where l_1, m_1, n_1 are direction cosines of the current direction with respect to the crystallographic axes. It should be noted that Eqn. 22 always yields a result of the form,

$$\left(\frac{\Delta\rho}{\rho\chi}\right)_l = a\pi_{11} + b(\pi_{12} + \pi_{44}). \qquad (23)$$

From the longitudinal measurements one can only obtain π_{11} and the combination $(\pi_{12} + \pi_{44})$. Therefore a transverse or hydrostatic measurement must be employed to separate π_{12} and π_{44}.

For transverse measurements, Mason and Thurston (47) find

$$\left(\frac{\Delta\rho}{\rho\chi}\right)_t = \pi_{12}+(\pi_{11}-\pi_{12}-\pi_{44})(l_1^2l_2^2+m_1^2m_2^2+n_1^2n_2^2) \qquad (24)$$

where l_1, m_1, n_1 are direction cosines of the current axis and l_2, m_2, n_2 are direction cosines of the stress axis. Pfann and Thurston (51) have tabulated the values $\Delta\rho/\rho\chi)_l$ and $\Delta\rho/\rho\chi)_t$ for several different sample-stress configurations.

Experimentally, one measures the relationship between resistivity and stress to obtain piezoresistance tensor components. Theoretically, it is more feasible to calculate the relationship between conductivity and strain to obtain elastoresistance tensor components [see Keyes (33)]. To compare theory with experiment, a relationship between the piezoresistance tensor and elastoresistance tensor is needed.

As before, the theory presented below comes from Keyes (33) and Smith (64).

The conductivity and strain are connected by the elastoresistance tensor in the same way the resistivity and stress were connected by the piezoresistance tensor. In analogy to Eqn. 5 we have,

$$\Gamma_{ij} = \frac{\delta\sigma_{ij}}{\sigma} = -\sum_{kl} m_{ijkl}u_{kl}, \tag{25}$$

where m_{ijkl} are the elastoresistance tensor components, u_{kl} the strain tensor components and $\delta\sigma_{ij}$ the change in conductivity with the application of a strain. In tensor notation, Eqn. 25 is written as

$$\bar{\Gamma} = -\bar{\bar{m}}:\bar{u}. \tag{26}$$

Now,

$$\bar{\sigma}\cdot\bar{\rho} = 1. \tag{27}$$

If a stress is applied to the crystal, both the resistivity and conductivity change and Eqn. 27 becomes

$$\delta\sigma\cdot\rho = -\sigma\cdot\delta\rho\ . \tag{28}$$

In the unstrained state both σ and ρ are scalers. Equation 28 can be written as

$$\frac{\delta \bar{\sigma}}{\sigma} = - \frac{\delta \bar{\rho}}{\rho} . \tag{29}$$

Equation 26 becomes

$$- \bar{\Gamma} = \bar{\Delta} = \bar{\bar{m}}:\bar{\bar{u}} = \bar{\bar{\pi}}:\bar{\bar{\chi}} . \tag{30}$$

The strain and stress are connected by the elastic constants [for example, see Kittel (38) page 89];

$$\bar{\bar{\chi}} = \bar{\bar{C}}:\bar{\bar{u}} \tag{31}$$

where C is the elastic constant tensor. Equation 30 can be written as

$$\bar{\bar{m}} = \bar{\bar{\pi}}:\bar{\bar{C}} . \tag{32}$$

The tensor form of both $\bar{\bar{m}}$ and $\bar{\bar{C}}$ are similar to the tensor form of $\bar{\bar{\pi}}$. Equation 32 can be solved for the m's in the form

$$m_{11} = \pi_{11}C_{11} + 2\pi_{12}C_{12}, \tag{33}$$

$$m_{12} = \pi_{12}C_{11} + \pi_{11}C_{12} + \pi_{12}C_{12} , \tag{34}$$

$$m_{44} = \pi_{44}C_{44} . \tag{35}$$

To make use of the elastoresistance tensor components in determining the direction of valleys in a many-valley semiconductor, one must discuss the fundamental strain coefficients [see, for example, Ziman p. 445 (77)]. The three fundamental strain coefficients are the volume coefficient and two pure shear strain coefficients (Fig. 6). The volume coefficient is the change in conductivity due to a volume dilatation (Fig. 6a). The volume coefficient can be obtained directly from hydrostatic measurements and from Eqn. 14 is

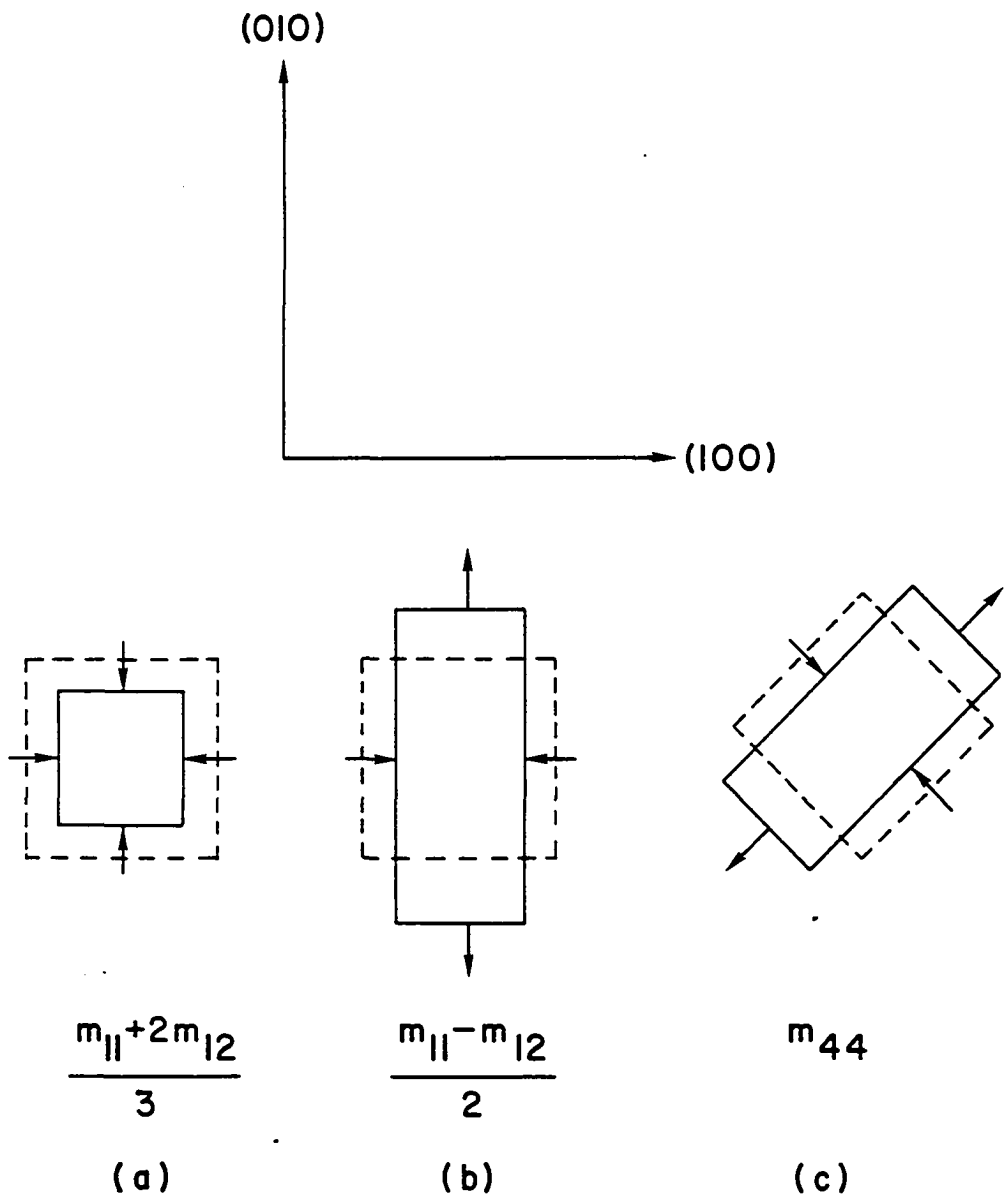

Figure 6. Definition of the fundamental strain coefficients, after Ziman (77) page 445.

found to be

$$\frac{\Delta\sigma}{\sigma} = \frac{m_{11} + 2m_{12}}{3} . \tag{36}$$

Under dilatation all valleys are affected in the same manner and $(m_{11} + 2m_{12})/3$ should be small.

One of the shear coefficients (Fig. 6b) has a strain matrix of the form

$$\bar{u} = \begin{pmatrix} u/2 & 0 & 0 \\ 0 & -u/4 & 0 \\ 0 & 0 & -u/4 \end{pmatrix} . \tag{37}$$

This is a strain system which preserves the volume of the sample. The applied strains are along the cubic axes of the crystal. From Eqns. 26 and 37 one obtains

$$\frac{\Delta\sigma}{\sigma} = \frac{m_{11} - m_{12}}{2} \tag{38}$$

as one of the shear coefficients. If valleys are along the <100> axes, $(m_{11} - m_{12})/2$ would be greater than zero. If, however, the valleys are along the <111> axes; this type shear would affect all valleys in the same manner and $(m_{11} - m_{12})/2$ would be small.

The other shear coefficient is composed of a tensile stress in the [110] direction and a corresponding stress perpendicular to the [110] direction (Fig. 6c). This type shear strain gives

$$\frac{\Delta\sigma}{\sigma} = m_{44} . \tag{39}$$

For <100> oriented valleys m_{44} would be small. A stress in the [110] direction is applied along a line which bisects the crystal axes. Valleys in the <111> direction would give a finite value to m_{44}. Those valleys in the plane of the tensile stress would be affected more than those out of the plane. For valleys in the <110> direction m_{44} would be large. Also m_{44} would be larger than $(m_{11} - m_{12})/2$ because $(m_{11} - m_{12})/2$ results from a pure shear stress in the <100> direction.

The following criteria, then, determined in what direction the energy ellipsoids lie:

<100> valleys;

$$\begin{aligned} m_{11} &= -2m_{12}, \\ m_{44} &= 0, \\ \frac{m_{11} - m_{12}}{2} &\text{ large}, \end{aligned} \tag{40}$$

<111> valleys;

$$\begin{aligned} m_{11} &= m_{12} = 0, \\ m_{44} &\text{ large}, \end{aligned} \tag{41}$$

<110> valleys;

$$\begin{aligned} \frac{m_{11} + 2m_{12}}{3} &= 0, \\ m_{44} &> \frac{m_{11} - m_{12}}{2} \text{ large} . \end{aligned} \tag{42}$$

For spheroidal energy surfaces at the origin, all factors

would be small. There would be no electron transfer mechanism to affect the change in resistivity.

It must be emphasized that the preceding discussion depends only on which valleys are present in the crystal. The result is independent of scattering mechanisms and of the number and types of impurities which are present in the material.

If acoustic mode scattering dominates, one can determine explicit expressions for the elastoresistance components in terms of the mobility anisotropy and deformation potential. Acoustic mode scattering is necessary in order to introduce the deformation potential. Bardeen and Shockley (3) and later Dumke (14) introduced the deformation potential. In their work it was shown that the deformation potential is useful in the temperature region where acoustic mode scattering dominates. Herring and Vogt (22) obtained explicit expressions for the elastoresistance tensor components by assuming the deformation potential theory of Bardeen and Shockley (3). The discussion presented below is due to Herring and Vogt (22).

The starting point for the analysis is the following:

$$\frac{\delta \sigma_{\alpha\beta}}{\sigma} = - \sum_{\gamma\delta} m_{\alpha\beta\gamma\delta} \, u_{\gamma\delta} \, . \qquad (25)$$

Equation 25 can be written as

$$m_{\alpha\beta\gamma\delta} = -\frac{1}{\sigma}\frac{\partial\sigma_{\alpha\beta}}{\partial u_{\gamma\delta}} \tag{43}$$

The coordinate system is the crystal axes; which is the same for all valleys. The conductivity can be written as

$$\sigma_{\alpha\beta}{}^{(i)} = n^{(i)}\, e\mu_{\alpha\beta}{}^{(i)} , \tag{44}$$

where $\sigma_{\alpha\beta}{}^{(i)}$ are components of the conductivity matrix of the ith valley, $n^{(i)}$ is the number of electrons in the ith valley and $\mu_{\alpha\beta}{}^{(i)}$ are components of the mobility matrix of the ith valley. Herring (21) showed that the main effect is the change in conductivity due to the shift of the valleys. Thus, $\partial\sigma_{\alpha\beta}{}^{(i)}/\partial\epsilon^{(j)}$ is introduced, where $\epsilon^{(j)}$ is the band-edge point of the jth valley. This term indicates the change in conductivity of the ith valley due to a shift in energy of the jth valley. Another term that must be introduced is $\partial\epsilon^{(i)}/\partial u_{\gamma\delta}$; that is, the change in energy of the jth valley due to an applied strain. Equation 44 becomes,

$$m_{\alpha\beta\gamma\delta} = -\frac{1}{\sigma}\sum_{i,j}\frac{\partial\sigma_{\alpha\beta}{}^{(i)}}{\partial\epsilon^{(j)}}\,\frac{\partial\epsilon^{(j)}}{\partial u_{\gamma\delta}} . \tag{45}$$

The terms $\partial\epsilon^{(j)}/\partial u_{\gamma\delta}$ are called the deformation potential constants and are tabulated in Table 3 [Herring and Vogt's Table II (22)]. The deformation potential constants relate the change in energy of a band-edge point to the applied strain. Additional discussion of the deformation potential will be given in the next section.

Table 3. Symmetry restrictions on the deformation potential constants for some simple types of valleys in a cubic semiconductor. Taken from Table II in Herring and Vogt (22)

Deformation potential tensor component	Type of valleys <100>	Type of valleys <111>
$\Xi_1 = \frac{\partial \epsilon(i)}{\partial u_{xx}}$	$\Xi_d + \Xi_u$	$\Xi_d + \frac{1}{3}\Xi_u$
$\Xi_2 = \frac{\partial \epsilon(i)}{\partial u_{yy}}$	Ξ_d	$\Xi_d + \frac{1}{3}\Xi_u$
$\Xi_3 = \frac{\partial \epsilon(i)}{\partial u_{zz}}$	Ξ_d	$\Xi_d + \frac{1}{3}\Xi_u$
$\Xi_4 = \frac{\partial \epsilon(i)}{\partial u_{yz}}$	0	$\frac{1}{3}\Xi_u$
$\Xi_5 = \frac{\partial \epsilon(i)}{\partial u_{xz}}$	0	$\frac{1}{3}\Xi_u$
$\Xi_6 = \frac{\partial \epsilon(i)}{\partial u_{xy}}$	0	$\frac{1}{3}\Xi_u$

To evaluate Eqn. 45, consider first the term $\frac{1}{\sigma}\frac{\partial\sigma_{\alpha\beta}(i)}{\partial\epsilon(j)}$. The conductivity σ is given by

$$\sigma = ne\mu \ , \tag{46}$$

where $\mu = (\mu_{\parallel} + 2\mu_{\perp})/3$, $\mu_{\parallel}$ is the mobility parallel to the valley, $\mu_{\perp}$ the mobility perpendicular to the valley and n the total number of electrons in the conduction band. By Eqn. 44, we have

$$-\frac{1}{\sigma}\frac{\partial\sigma_{\alpha\beta}(i)}{\partial\epsilon(j)} = -\frac{\mu_{\alpha\beta}(i)}{n\mu}\frac{\partial n(i)}{\partial\epsilon(j)} - \frac{n(i)}{n\mu}\frac{\partial\mu_{\alpha\beta}(i)}{\partial\epsilon(j)}. \tag{47}$$

The number of electrons in the i<u>th</u> valley is given by a Maxwell-Boltzmann distribution function,

$$n_i \propto e^{-|\epsilon(i) - \epsilon_f|/kT}, \tag{48}$$

where ϵ_f is the Fermi energy level. Substituting Eqn. 48 into the first term on the right of Eqn. 47 we have

$$\frac{\partial n(i)}{\partial\epsilon(j)} = -\frac{n(i)}{kT}\left(\frac{\partial\epsilon(i)}{\partial\epsilon(j)} - \frac{\partial\epsilon_f}{\partial\epsilon(j)}\right) \ , \tag{49}$$

where $\partial\epsilon^{(i)}/\partial\epsilon^{(j)} = \delta_{ij}$. In the <u>extrinsic temperature region</u> the variation of the Fermi level with strain is the average of the variation from all of the $\epsilon^{(i)}$; that is, some levels are shifted upward and some downward and the readjustment of the Fermi level will be the average of the readjustment of the valley band-edge points. We have

$$\frac{\partial\epsilon_f}{\partial\epsilon^{(j)}} = \frac{\sum_i \frac{\partial\epsilon^{(i)}}{\partial\epsilon^{(j)}}}{N_v} = \frac{1}{N_v} \ , \tag{50}$$

where N_v is the number of valleys. Equation 49 can then be written as

$$\frac{\partial n^{(i)}}{\partial \epsilon^{(j)}} = - \frac{n^{(i)}}{kT} \left(\delta_{ij} - \frac{1}{N_v} \right) . \qquad (51)$$

The electron transfer effect (first term on the right side of 47) becomes

$$- \frac{\mu_{\alpha\beta}{}^{(i)}}{n\mu} \frac{\partial n^{(i)}}{\partial \epsilon^{(j)}} = \frac{\mu_{\alpha\beta}{}^{(i)}}{kT\mu} \left(\frac{\delta_{ij}}{N_v} - \frac{1}{N_v{}^2} \right) . \qquad (52)$$

The second term on the right side of Eqn. 47 can be written as

$$- \frac{n^{(i)}}{n\mu} \frac{\partial \mu_{\alpha\beta}{}^{(i)}}{\partial \epsilon^{(j)}} = \frac{- e}{N_v \mu_m{}^{(i)*}} \frac{\partial \langle \tau^{(i)} \rangle}{\partial \epsilon^{(j)}} \qquad (53)$$

where $\mu_{\alpha\beta}{}^{(i)} = e/m^{(i)*}\langle \tau^{(i)} \rangle$, $\langle \tau^{(i)} \rangle$ is the average of the relaxation time in the ith valley and $m^{(i)*}$ is the effective mass of the electrons in the ith valley. Herring (21) showed that the change of relaxation time under an applied stress is negligible when compared to the effect of repopulation of the valleys. Equation 53 can be set equal to zero. Equation 45 becomes,

$$m_{\alpha\beta\gamma\delta} = \sum_{i,j} \frac{1}{kT} \frac{\mu_{\alpha\beta}{}^{(i)}}{\mu} \left(\frac{\delta_{ij}}{N_v} \frac{1}{N_v{}^2} \right) \frac{\partial \epsilon^{(j)}}{\partial u_{\gamma\delta}} \qquad (54)$$

The deformation potential constants $\partial \epsilon^{(j)}/\partial u_{\gamma\delta}$ are represented in terms of the constants, Ξ_u and Ξ_d. For valleys along the <111> or <100> axes Ξ_d represents a shift in the energy ellipsoids due to a dilatation in the two directions

normal to the [100] axis, while Ξ_u represents the shift due to a uniaxial shear compounded out of a stretch along the [100] axis and a contraction in the two normal directions [see Herring (21)].

As an example of an explicit calculation of an elasto-resistance tensor component, consider an n-type semiconductor with valleys in the <100> direction. In Eqn. 54 the summation is carried out for i, j = 1, 2, 3; and $N_v = 3$. Also

$$\mu_{11}^{(1)} = \mu_{\parallel}, \quad \mu_{11}^{(2)} = \mu_{11}^{(3)} = \mu_{\perp} \tag{55}$$

With the substitution of the deformation potentials and of Eqn. 55 into Eqn. 54 one obtains,

$$m_{1111} = m_{11} = 2/9 \frac{\Xi_\mu}{kT} \frac{(\mu_{\parallel} - \mu_{\perp})}{1/3(\mu_{\parallel} + 2\mu_{\perp})}, \tag{56}$$

$$m_{12} = -1/9 \frac{\Xi_\mu}{kT} \frac{(\mu_{\parallel} - \mu_{\perp})}{1/3(\mu_{\parallel} + 2\mu_{\perp})}, \tag{57}$$

$$m_{44} = 0. \tag{58}$$

Again, we reach the conclusion that for <100> valleys;

$$m_{11} = -2m_{12},$$

$$m_{44} = 0. \tag{59}$$

In a similar fashion one finds for <111> valleys;

$$m_{11} = m_{12} = 0, \tag{60}$$

$$m_{44} = 1/9 \frac{\Xi_\mu}{kT} \frac{(\mu_{\parallel} - \mu_{\perp})}{1/3(\mu_{\parallel} + 2\mu_{\perp})}. \tag{61}$$

which is the same result we obtained in Eqn. 41.

Herring and Vogt (22) reported on explicit calculations for valleys centered on the <110> axes.

Another result from Equations 56-61 is that the elastoresistance components should vary as 1/T if it is assumed that the mobility anisotropy is independent of temperature.

Experimentally, one must measure the piezoresistance tensor components and convert to elastoresistance tensor components with the use of Eqns. 33-35. To determine in what direction the valleys lie, the experimental relationship between the m's must be compared with Eqns 40-42. Also the m's should be linear with respect to 1/T.

More information can be obtained from Eqns 56-61 if one knows the mobility anisotropy ratio, which can be obtained from magnetoresistance data. With the mobility anisotropy ratio one can use the piezoresistance data to obtain a value of the deformation potential.

If one extends the piezoresistance measurements to large stresses ($\chi > 10^9$ dynes/cm^2), the mobility anisotropy ratio and the deformation potential can be obtained from the same experiment on the same sample. Investigation of high stress piezoresistance measurements is the object of the next section.

B. Deformation Potential Theory

One of the major concerns of semiconductor physicists is the explicit determination of the relaxation time. In particular, for many-valley semiconductors one would like to determine the components of the relaxation time matrix, $\tau_{\parallel}$ and $\tau_{\perp}$, where $\tau_{\parallel}$ and $\tau_{\perp}$ are the relaxation time components parallel and perpendicular to the symmetry axis of the valley. If the relaxation time matrix components are known, explicit values for the transport properties can be calculated. For example, the conductivity is given by [see Herring and Vogt (22)],

$$\sigma = \frac{ne^2}{3}\left(\frac{\langle\tau_{\parallel}\rangle}{m_{\parallel}^*} + \frac{2\langle\tau_{\perp}\rangle}{m_{\perp}^*}\right)$$

where $\langle\ \rangle$ denotes a Maxwellian average and m^* is the effective mass. The hall mobility is given by

$$\frac{\mu_H}{\mu} = 3\ \frac{\left(\frac{2\langle\tau_{\parallel}\ \tau_{\perp}\rangle}{m_{\parallel}^* m_{\perp}^*} + \frac{\langle\tau_{\perp}^2\rangle}{m_{\perp}^{*2}}\right)}{\left(\frac{\langle\tau_{\parallel}\rangle}{m_{\parallel}^*} + \frac{2\langle\tau_{\perp}\rangle}{m_{\perp}^*}\right)^2}\ .$$

Similar expressions can be found for carrier mobility and magnetoresistance.

A difficulty arises from the fact that the relaxation time is dependent on the scattering mechanisms present in the material. However, if acoustic mode scattering dominates, the calculations are simplified and expressions for the relaxation times in terms of deformation potential constants can be obtained. For acoustic mode scattering the electron energy

is assumed unchanged.

The deformation potential was first introduced by Bardeen and Shockley (3) to relate the change in energy gap of a semiconductor to an applied stress. Their early work was restricted to non-polar semiconductors with spherical constant energy surfaces located at $\underline{k} = 0$ in wave vector space. Dumke (14) extended Bardeen and Shockley's work to a many-valley model. In his work, Dumke obtained an expression for the relaxation time in terms of the deformation potential, but assumed that the relaxation time was a function of energy only. Herring and Vogt (22) extended the calculations but did not assume that τ was only a function of energy. They also determined explicit expressions for the components of the relaxation time matrix in terms of the deformation potential constants. They found

$$\tau_{\parallel} = \frac{3(m_{\parallel}^{*} m_{\perp}^{*2})^{\frac{1}{2}} kT\ \varepsilon^{\frac{1}{2}}}{2^{3/2}\pi\hbar^{4} c_{l}} (\xi_{\parallel} \Xi_{d}^{2} + \eta_{\parallel} \Xi_{d} \Xi_{u} + \zeta_{\parallel} \Xi_{u}^{2}),$$

and

$$\tau_{\perp} = \frac{3(m_{\parallel}^{*} m_{\perp}^{*2})^{\frac{1}{2}} kT\ \varepsilon^{\frac{1}{2}}}{2^{3/2}\pi\hbar^{4} c_{l}} (\xi_{\perp} \Xi_{d}^{2} + \eta_{\perp} \Xi_{d} \Xi_{u} + \zeta_{\perp} \Xi_{u}^{2}),$$

where ε is the energy relative to the band edge point, $c_l = 1/5(3c_{11} - 2c_{12} - 4c_{44})$ and ξ, η, ζ are functions of the elastic constants, c, and mass ratio, $m_{\perp}^{*}/m_{\parallel}^{*}$. The deformation potential constant Ξ_u can be determined from piezoresistance measurements. To determine Ξ_d one forms the ratio,

$$\frac{\tau_{\parallel}}{\tau_{\perp}} = \frac{a(\Xi_d/\Xi_u)^2 + b(\Xi_d/\Xi_u) + c}{d(\Xi_d/\Xi_u)^2 + e(\Xi_d/\Xi_u) + f} ,$$

where a,..., f are combinations of the ξ, η, and ζ. If the mobility ratio, K, and the effective masses are known the ratio $\tau_{\parallel}/\tau_{\perp}$ can be found. From a plot of $\tau_{\parallel}/\tau_{\perp}$ versus Ξ_d/Ξ_u, one obtains a value for Ξ_d/Ξ_u which allows a determination of Ξ_d. When elastic constants, effective masses and deformation potential constants are known, explicit values for the relaxation time matrix components can be obtained.

In addition, the deformation potential can be used to relate the change in energy gap of a semiconductor to an applied stress.

The object of the development here will be to define the deformation potential and to give an analysis of a high stress piezoresistance measurement which can be used to obtain the deformation potential.

The most useful descriptions of the deformation potential are found in articles by Herring (21), Herring and Vogt (22), Koenig (39), Keyes (33) and Fritzsche (18). The development presented here is taken from the above articles.

The deformation potential is defined by

$$\delta e^{(i)} = \sum_{r,s} \Xi_{rs}^{(i)} u_{rs} . \qquad (62)$$

In terms of the reduced notation (Eqn. 6),

$$\delta e^{(i)} = \sum_{j} \Xi_j u_j , \qquad (63)$$

where the u_{rs} are components of a strain tensor, the Ξ_{rs} are deformation potential constants and the $\delta\epsilon^{(i)}$ represent shifts of the energy levels in the ith valley due to the application of a strain $\bar{u}$.

In cubic semiconductors, axes of symmetry of the valleys usually lie along the axes of three or four-fold symmetry. The second rank tensors associated with the valleys have rotational symmetry and are symmetric about the diagonal. The deformation potential tensor is written as [see Keyes (33) and Koenig (39)],

$$\bar{\bar{\Xi}} = \Xi_d \bar{\bar{1}} + \Xi_u \bar{a}^{(i)}\bar{a}^{(i)}, \qquad (64)$$

where $\bar{a}^{(i)}$ are unit vectors along the symmetry axes of the ith valley. Ξ_d and Ξ_u are uniaxial and dilatation deformation potentials respectively. The change in energy of the ith valley can be described in terms of these two constants. Ξ_d implies a band-edge shift of $\Xi_d u$ due to a dilatation along the two normal directions of the valleys. Ξ_u implies a band-edge shift of $\Xi_u u$ due to a contraction in the two perpendicular directions along with a stretch along the parallel direction.

As an example, consider a semiconductor with <100> valleys. Consider the application of a compressive stress in the [100] direction. For this case $a_1^{(i)} = 1$, $a_2^{(i)} = a_3^{(i)} = 0$ and $\bar{u}$ has only the component $-u_{11}$. The deformation potential tensor becomes,

$$\Xi = \begin{pmatrix} \Xi_d + \Xi_u & 0 & 0 \\ 0 & \Xi_d & 0 \\ 0 & 0 & \Xi_d \end{pmatrix} \tag{65}$$

The change in energy of the valleys parallel to the [100] axis is given by

$$\delta\epsilon_{[100]} = -\Xi_1 u_1 = -(\Xi_d + \Xi_u)u \ . \tag{66}$$

The valley is shifted downward.

We will use the definition of the deformation potential given above, and next turn our attention to the problem of determining the mobility ratio and deformation potential.

Experimentally, one extends the piezoresistance measurements to saturation; that is, to such a large stress that when a still larger stress is applied, the ratio $\Delta\rho/\rho$ remains a constant.

The development of the following is taken from Aubrey et al. (2). These authors used the high stress piezoresistance technique to obtain the deformation potential for silicon. Magnesium stannide and silicon are similar in that they are both many valley semiconductors with valleys in the <100> direction.

The conductivity in the [100] direction of a crystal with <100> valleys is given by

$$\sigma = n_{\parallel} e\mu_{\parallel} + 2n_{\perp} e\mu_{\perp} \ , \tag{67}$$

where $n_{\parallel}$ is the number of electrons in the [100] valleys,

$n_\perp$ is the number of electrons in each of the [010] and [001] valleys and $\mu_{||}$ and $\mu_\perp$ are the respective mobilities. When a compressive uniaxial stress is applied in the [100] direction, the [100] valley is shifted downward by an amount $^{\delta}\epsilon_{[100]}$ and the [001] valley is shifted upward by an amount $^{\delta}\epsilon_{[001]}$. The difference in energy between the two valley band-edge points is given by $^{\delta}\epsilon = {}^{\delta}\epsilon_{[001]} - {}^{\delta}\epsilon_{[100]}$. The stress and strain are related by,

$$u_s = \sum_r S_{sr}\, \chi_r, \tag{68}$$

where the S_{sr} are components of the elastic compliance tensor and can be derived from the elastic constants [see Kittel p. 89 (38)]. Equation 63 can be written as

$$^{\delta}\epsilon^{(i)} = \sum_{r,s} \Xi_s\, S_{sr}\, \chi_r \tag{69}$$

If the uniaxial stress is a compressive stress in the [100] direction, $\chi_r = -\chi_1$. For $^{\delta}\epsilon_{[100]}$ we have

$$^{\delta}\epsilon_{[100]} = -\sum_s \Xi_s\, S_{s1}\, \chi_1. \tag{70}$$

By use of Eqn. 65, Eqn. 70 can be written as

$$^{\delta}\epsilon_{[100]} = -\chi_1[S_{11}(\Xi_d + \Xi_u) + S_{12}\Xi_d + S_{12}\Xi_d]. \tag{71}$$

For $^{\delta}\epsilon_{[001]}$, the stress is written as $\chi_r = -\chi_2$; that is, the stress is perpendicular to the <001> valleys. Therefore,

$$^{\delta}\epsilon_{[001]} = -\chi_2[S_{12}(\Xi_d + \Xi_u) + S_{11}\Xi_d + S_{12}\Xi_d]. \tag{72}$$

By combining Equations 71 and 72 we find the relative shift to be

$$\delta\epsilon = \delta\epsilon_{[001]} - \delta\epsilon_{[100]} = \Xi_u(S_{11} - S_{12})\chi \,, \qquad (73)$$

where $\chi = \chi_1 = \chi_2$.

Assume that it is possible to place a large enough stress on the crystal such that the difference in energy, $\delta\epsilon$, between parallel and perpendicular valleys is great enough to effectively empty the higher valley. At zero stress, $n_{\parallel} = n_{\perp} = N/3$, where N is the total number of electrons. At saturation $n_{\parallel} = N$ and $n_{\perp} = 0$; that is, all the electrons are now in the parallel, or lower, valleys. The ratio of electrons in the two valleys is given by,

$$\frac{n_{\perp}}{n_{\parallel}} = e^{-\delta\epsilon/kT} = e^{-\beta\chi} \,, \qquad (74)$$

where

$$\beta = \frac{\Xi_u(S_{11} - S_{12})}{kT} \qquad (75)$$

At zero stress the conductivity is,

$$\sigma_o = N/3(\mu_{\parallel}^{o} + 2\mu_{\perp}^{o}), \qquad (76)$$

where $\mu_{\parallel}^{o}$ and $\mu_{\perp}^{o}$ are the mobilities in the unstrained state. At saturation the conductivity becomes,

$$\sigma_s = Ne\mu_{\parallel}^{s} \,, \qquad (77)$$

where $\mu_{\parallel}^{s}$ is the parallel mobility in the saturated state. The ratio of Eqns. 76 and 77 is given by

$$\frac{\rho_s}{\rho_o} = \frac{\sigma_o}{\sigma_s} \quad \frac{\mu_{\parallel}^{o} + 2\mu_{\perp}^{o}}{3\mu_{\parallel}^{s}} \,. \qquad (78)$$

Now assume that the stress shifts the energy of all states associated with a given valley by the same amount [see Keyes

(33)]; that is, assume that the valley moves along the energy scale as a unit and the various parameters such as effective masses and relaxation times are unchanged by the application of a stress. With this assumption ($\mu_{\parallel}^{s} = \mu_{\perp}^{o}$), Eqn. 78 becomes

$$\frac{\rho_s}{\rho_o} = 1/3(1+2K), \tag{79}$$

where $K = \mu_{\perp}^{o} / \mu_{\parallel}^{o}$. By going to saturation the mobility anisotropy can be determined.

To determine the deformation potential, consider the following ratio,

$$\frac{\rho}{\rho_o} = \frac{\sigma_o}{\sigma} = \frac{n_{\parallel}^{o} \mu_{\parallel}^{o} + 2n_{\perp}^{o} \mu_{\perp}^{o}}{n_{\parallel} \mu_{\parallel} + 2n_{\perp} \mu_{\perp}} , \tag{80}$$

where ρ is the resistivity under an applied stress. From Eqn. 80 we have

$$\frac{\rho}{\rho_o} = \frac{n_{\parallel}^{o} \mu_{\parallel}^{o} + 2n_{\perp}^{o} \mu_{\perp}^{o}}{(1+2Ke^{-\beta\chi})n_{\parallel} \mu_{\parallel}} = \frac{(1+2K)}{(1+2Ke^{-\beta\chi})} \frac{n_{\parallel}^{o}}{n_{\parallel}} \tag{81}$$

But,

$$n_{\parallel}^{o} = N/3 = \frac{(n_{\parallel}+2n_{\perp})}{3} . \tag{82}$$

By substituting Eqn. 82 into Eqn. 81 we have

$$\frac{\rho}{\rho_o} = \frac{1}{3} \frac{(1+2K)(1+2e^{-\beta\chi})}{(1+2Ke^{-\beta\chi})} \tag{83}$$

With the value of K obtained from Eqn. 79, the parameter β in Eqn. 83 can be adjusted to give a best fit of Eqn. 83 to an

experimental ρ/ρ_o versus χ curve. From this value of β, a value for the deformation potential can be obtained.

IV. MEASUREMENT APPARATUS

The apparatus used in this experiment has been described in detail in a thesis by Paul A. Temple (67). The apparatus was assembled and constructed by P. A. Temple and the author with the grateful assistance of P. H. Sidles and O. M. Sevde of the Ames Laboratory. A short description of the apparatus, along with the appropriate diagrams, will be given here.

A. Loading System

The simplest method of applying stress to a sample is either to place a weight on the sample to compress it or to hang a weight from the sample to stretch it. These methods have two difficulties associated with them. The first difficulty is the problem of placing a weight on the sample. If the weight is not carefully lowered onto the sample, the mechanical impulse given to the sample may be enough to fracture the sample. The second difficulty is one of inflexibility. There are times when it is desirable to change the stressing weight; for example, to check the linearity of $\Delta\rho/\rho$ versus stress or to measure the deformation potential. With the methods suggested above, the vacuum system around the sample holder must be broken in order to change weights. If the linearity or deformation potential is desired at temperatures other than those which can be obtained with fixed temperature baths, difficulty with the maintenance of a

constant sample temperature may be experienced. Another disadvantage is that every time the vacuum is broken there is a chance of water vapor condensing onto the sample. In the case of Mg_2Sn, which oxidizes very readily, the condensing of water vapor on the sample could be disastrous.

The loading apparatus described here and by Temple (67) minimized the difficulties mentioned above. The loading apparatus made use of a differential gas pressure applied across a nickel bellows (Fig. 7). The push rod was attached to the nickel bellows which separated the bellows chamber and the sample chamber. The push rod rested on the sample so that the spring constant of the bellows could be neglected.

The pressure applied to the sample was measured by a single well mercury manometer. Two photo cells were mounted on the manometer to regulate the height of the mercury and thus, regulate the pressure applied to the sample. The pressure applied to the sample could be controlled externally without breaking the vacuum around the sample by a simple adjustment of the position of the photo cells. Thus both the difficulties associated with previous methods were eliminated with the loading system described here.

To begin the loading procedure, solenoid valves 2 and 3 were simultaneously opened. The circuit diagram of the electronics used for controlling the solenoid valves is shown in Fig. 8. With valves 2 and 3 open, gas flowed into

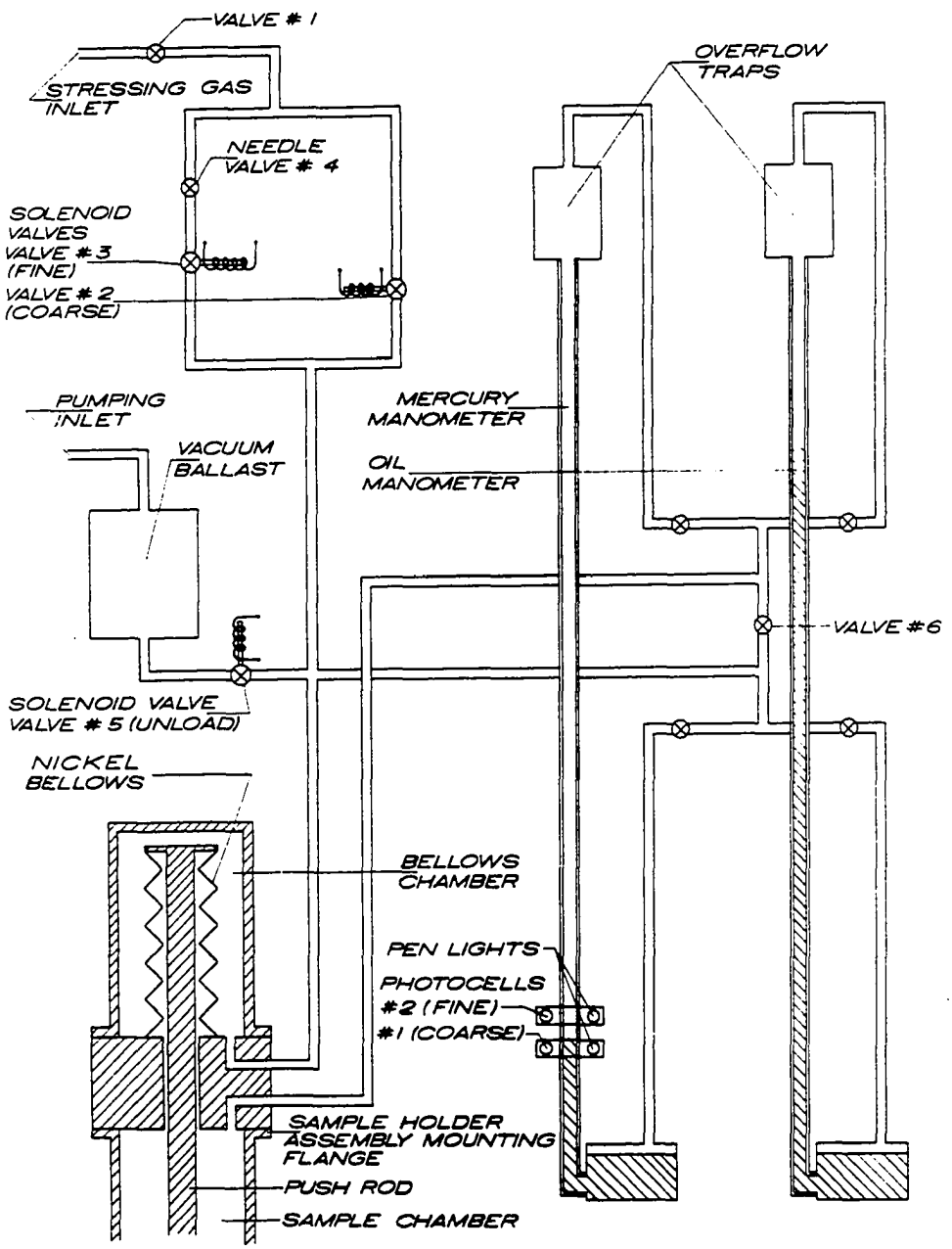

Figure 7. Diagram of the sample stressing apparatus.

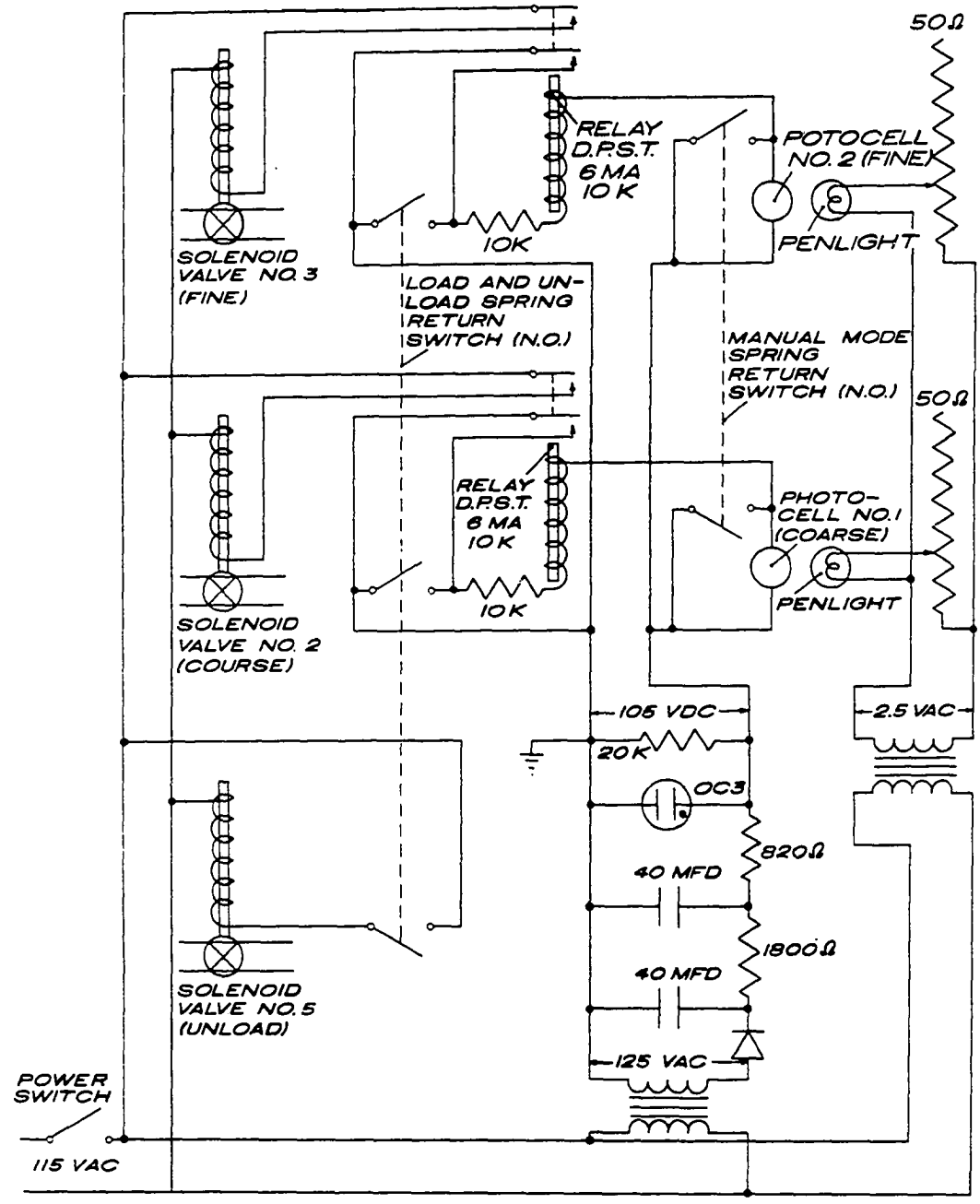

Figure 8. Diagram of the electrical circuit used to control the solenoid valves.

the bellows chamber which caused a stress to be applied, via the push rod, to the sample. As gas flowed into the bellows chamber, the mercury rose past photo cell 1 which caused solenoid valve 2 to close. Valve 1 was adjusted so that the time required to reach a mercury level which corresponded to a 1000 gram load was 10 seconds. After solenoid valve 2 was closed the gas passed through needle valve 4 and solenoid valve 3. The needle valve reduced the flow of gas such that it took 5 seconds for the mercury to reach photo cell 2. After solenoid valve 3 closed, the desired pressure on the sample was obtained. The total time required to load the sample was 15 seconds. The load was applied gradually and not instantaneously, as was the case for previous methods. The second photo cell and solenoid valve were introduced so that the mercury slowly approached the final level. The level of mercury was repeatable to within $\pm$ 0.5 mm. A mercury height of 250 mm corresponded to a load of 1045 grams; which was the pressure used for piezoresistance measurements. The error due to inaccuracy in the mercury level was $\pm$ 0.2%.

The loading system was calibrated by placing the push rod on a beam balance, then by adding gas to the bellows chamber the weight equivalent to one mm of Hg was determined. Several loadings at different pressures were made. The sample load per mm of Hg was determined to be 4.148 $\pm$ 0.017 gm-wt/mm of Hg [see Temple (67)]. A standard deviation treatment of these

data gave a possible error in the calibration of ± 0.4%.

To unload the sample, solenoid valve 5 was opened and the gas in the bellows chamber was pumped out through the vacuum ballast. The time required for unloading was 2 seconds.

Valve 6 (by-pass valve) was introduced so that during initial pump down the entire system (sample chamber plus loading system) could be evacuated at one time. To load the sample the by-pass valve was closed.

To extend the piezoresistance measurements to include a measurement of the deformation potential a modification of the equipment described by Temple (67) was necessary. In the original design a nickel bellows with a 1.0" O.D. and 0.59" I.D. was used. With a 250 cm mercury manometer the original bellows allowed a maximum stress of 4.58×10^8 dynes/cm^2 on a 1.5 x 1.5 mm sample. However, for the deformation potential measurements, a greater stress was necessary. To obtain the high stress, the original nickel bellows was replaced by another nickel bellows with a 1.75" O.D. and 1.58" I.D. The effective cross-sectional area of the bellows chamber was increased by a factor of 4.3. The cross-sectional area of the sample was decreased from 2.25 mm^2 to 1.56 mm^2 (a 1.25 x 1.25 mm sample) to further increase the stress by a factor of 1.4. The total stress available was then 24×10^8 dynes/cm^2.

To calibrate the large bellows we first measured the piezoresistance effect on a [100] oriented Mg_2Sn sample with

the smaller bellows. The ratio $\Delta\rho/\rho_L$ was measured as a function of stress. These measurements were made while the load was increased from 5×10^7 to 4.58×10^8 dynes/cm^2 and then decreased back down to 5×10^7 dynes/cm^2. The measurements were made with both increasing and decreasing loads to show that the hysteresis effect was negligible. The large bellows was then placed in the bellows chamber. Again the ratio $\Delta\rho/\rho_L$ was measured as a function of stress. As for the small bellows, $\Delta\rho/\rho_L$ was measured with both increasing and decreasing loads. Again the hysteresis effect was negligible. After the sample had set for 24 hours a second measurement of $\Delta\rho/\rho_L$ as a function of stress was made with the large bellows. The two trials agreed within experimental error. The large bellows was then removed and replaced with the small bellows. Another measurement of $\Delta\rho/\rho_L$ was made as a function of stress with the small bellows. The second measurement with the small bellows was made to confirm that the sample had not changed. Both measurements of $\Delta\rho/\rho_L$ versus gm-wt for the small bellows are shown in Fig. 9. The results for both sets of measurements agreed. The $\Delta\rho/\rho_L$ values obtained with the large bellows were then compared with an enlarged curve similar to Fig. 9. A gm-wt value per mm of Hg was determined for the large bellows in the region where the two sets of $\Delta\rho/\rho_L$ values overlapped. The results of this comparison are given in Table 4. The average value of gm-wt per mm of Hg was determined to be

Table 4. Large bellows calibration data

Manometer reading (cm of Hg)	Fractional change in resistivity (100 $\Delta\rho/\rho_L$)	Result of comparing $\Delta\rho/\rho_L$ with Fig. 9 (grams)	Resultant grams per mm of mercury
	Trial #1 increasing load		
15.60	4.821	2364	15.15
24.70	8.001	3793	15.35
34.90	11.345	5271	15.10
44.80	14.987	6854	15.30
54.75	18.295	8266	15.10
64.70	21.578	9727	15.04
	Trial #1 decreasing load		
59.70	20.233	9110	15.26
50.00	16.560	7526	15.05
40.40	13.432	6180	15.30
29.60	9.713	4556	15.39
20.00	6.326	3050	15.25
	Trial #2		
20.20	6.516	3116	15.43
24.90	8.015	3896	15.65
30.10	9.901	4609	15.31
35.50	11.714	5451	15.36
40.30	13.456	6169	15.31
45.00	15.102	6876	15.28
50.50	17.000	7711	15.27
55.00	18.580	8411	15.29
59.95	20.210	9139	15.24
65.00	22.030	9883	15.20
70.00	24.240	10691	15.27

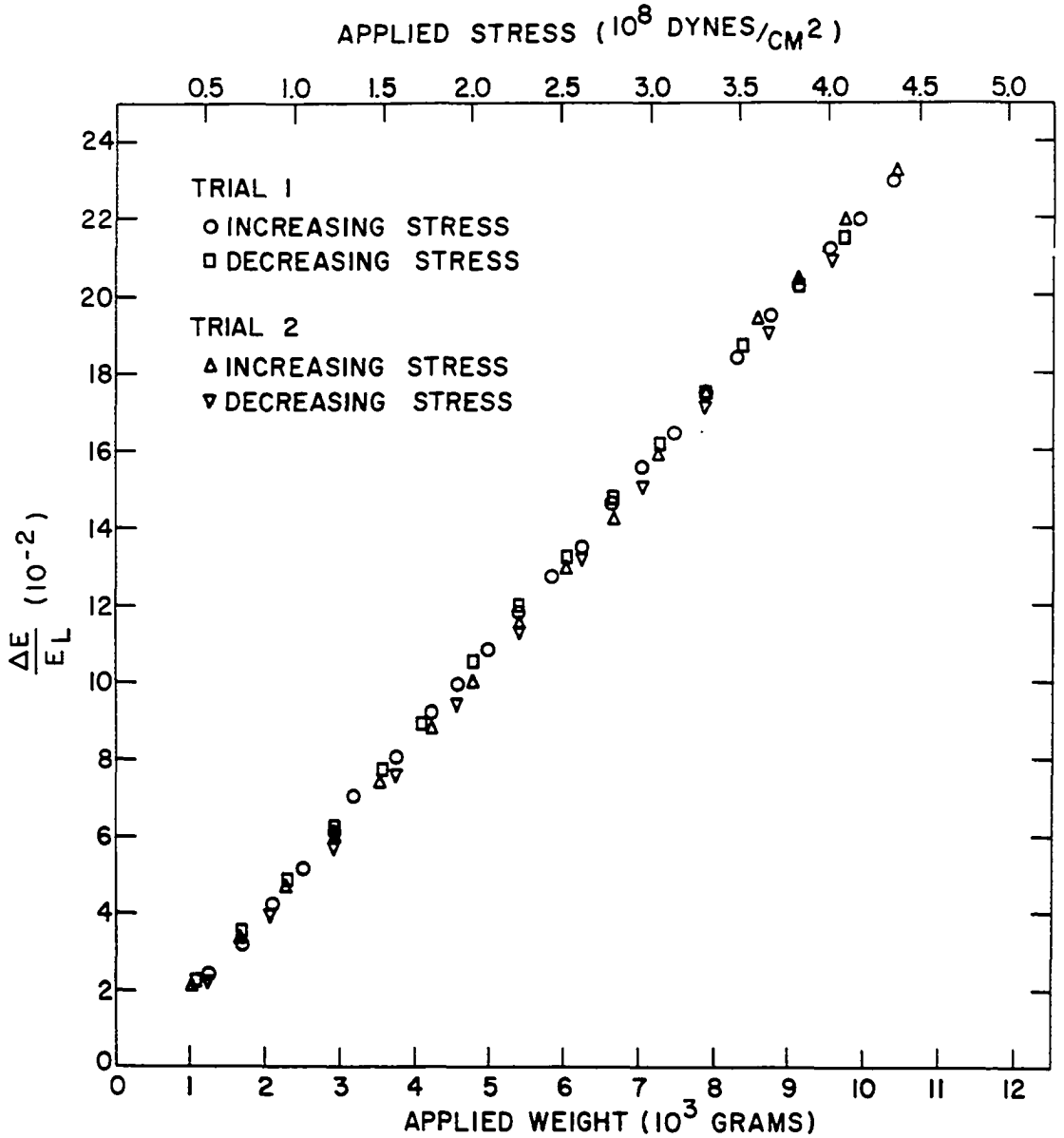

Figure 9. Result of $\Delta E/E_L$ as a function of stress for small bellows. Trial 1 was before and Trial 2 after large bellows was placed in loading apparatus. The agreement shows that the sample had not changed. The agreement between increasing and decreasing stress shows that the hysteresis effect was negligible.

15.25 ± 0.19 gm-wt/mm of Hg. The standard deviation gave an error of 1.3%.

B. Sample Holder

The sample holder is illustrated in Fig. 10. The copper spring was used to counter balance the weight of the push rod so that a minimum of stress was applied to the sample in the unloaded position. Since $\Delta\rho/\rho$ versus χ is linear; a small initial load (approximately 50 gms) does not change the result of the experiment. The Teflon sample support supported the sample in an upright position. The copper tube surrounding the sample holder helped minimize temperature gradients along the sample.

To make the piezoresistance measurements, a modification of the push rod and pedestal as described by Temple (67) was necessary. Instead of attaching current leads to the ends of the sample, the current leads were mounted on the push rod and pedestal. The current leads consisted of a copper sheet to which was soldered a 1/32 inch indium pad. The indium pads deformed to fit the ends of the sample. The current leads were attached to the copper sheets. The change in current through the sample upon stressing the sample was less than one part in 10^5. With this arrangement the current density through the sample remained constant.

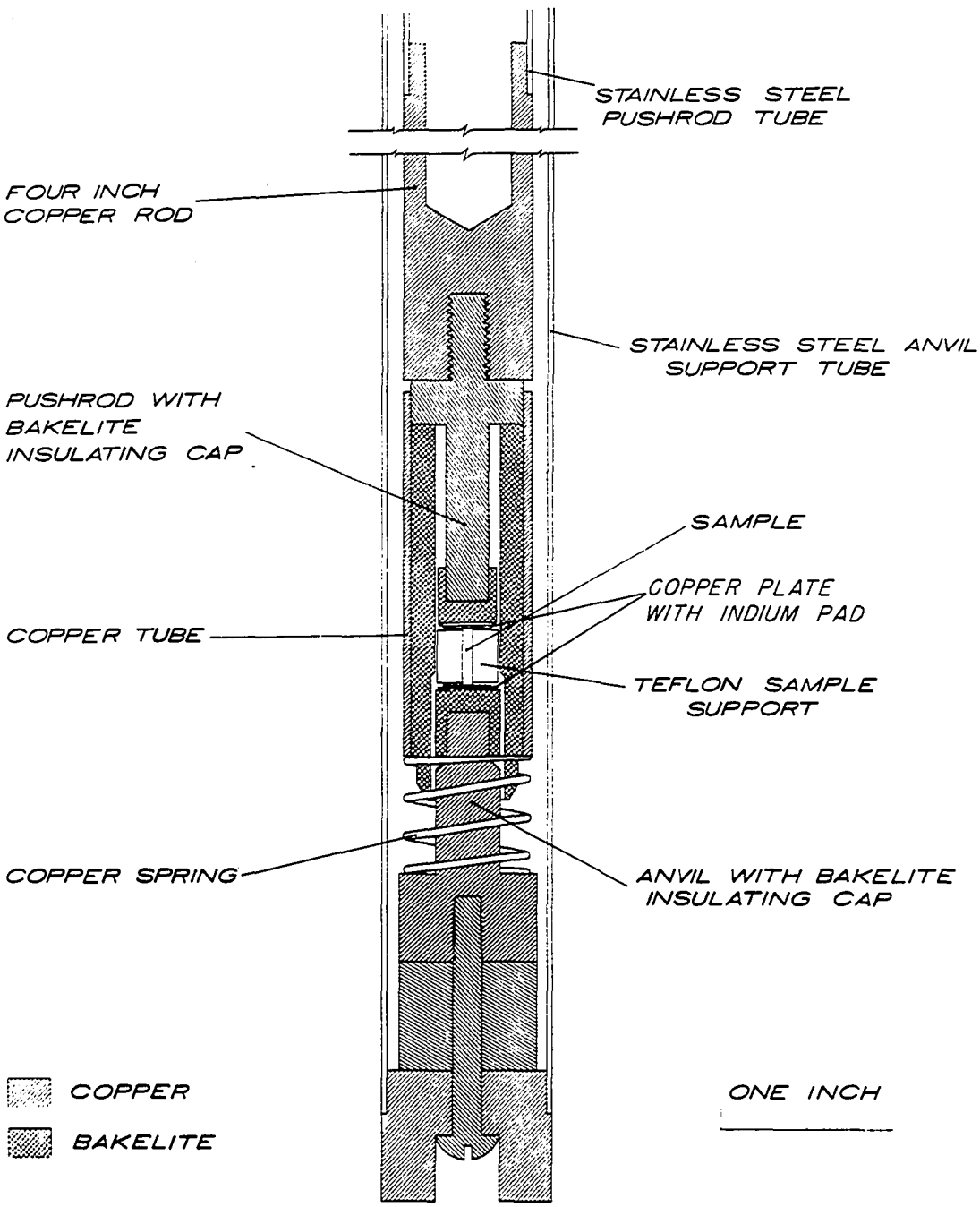

Figure 10. Cross-sectional diagram of the sample holder.

C. Resistivity Measurement

The instrumentation for measuring resistivity is shown in Fig. 11. To obtain a constant current through the sample fourteen 1.35 volt mercury batteries were connected in series with the sample and a high resistance decade box. A constant current of 0.2-1.0 ma was used. Switch 2 was used to reverse the current to the sample. Switch 1 was used in connection with switch 2. When the current was reversed, the voltage into the potentiometer could also be reversed. This reversal procedure was used so that thermal gradient effects could be averaged out. The Biddle-Gray potentiometer was used to measure and to null the voltage across the sample in the unloaded position. The change in voltage with applied stress was recorded on a strip chart recorder. The strip chart recorder was calibrated by first nulling the Keithley amplifier with the Biddle potentiometer. The Wilk potentiometer was set at the full scale value shown on the Keithly milli-microvoltmeter. The known voltage from the Wilk potentiometer was introduced at the Keithly milli-microvoltmeter output. The voltage divider was then adjusted to give a full scale deflection on the strip chart recorder.

D. Temperature Control

Figure 12 shows the temperature control apparatus which was employed. A copper-constantan thermocouple was used for temperature control. A second copper-constantan thermocouple

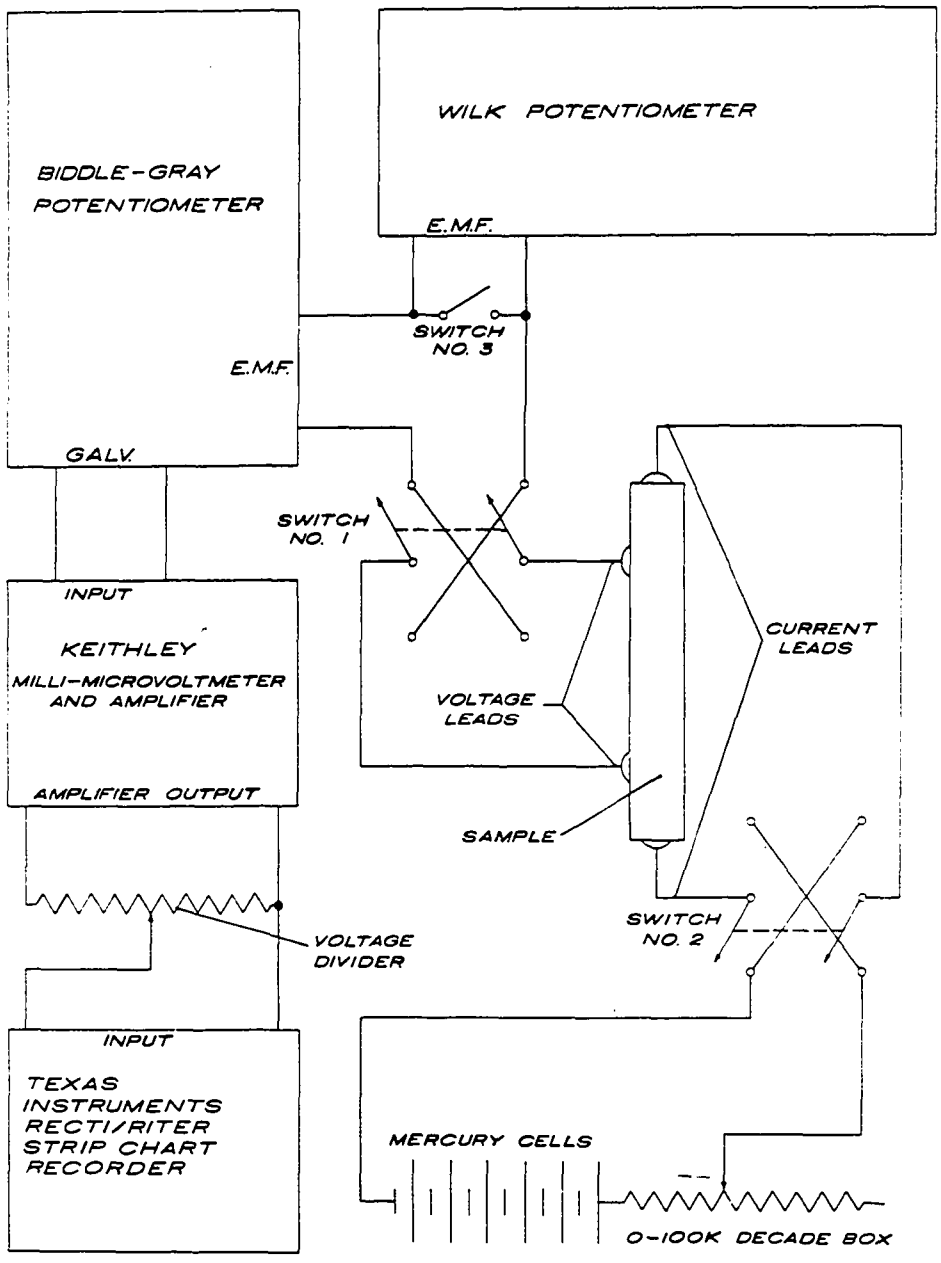

Figure 11. Block diagram of the instrumentation for measuring resistivity.

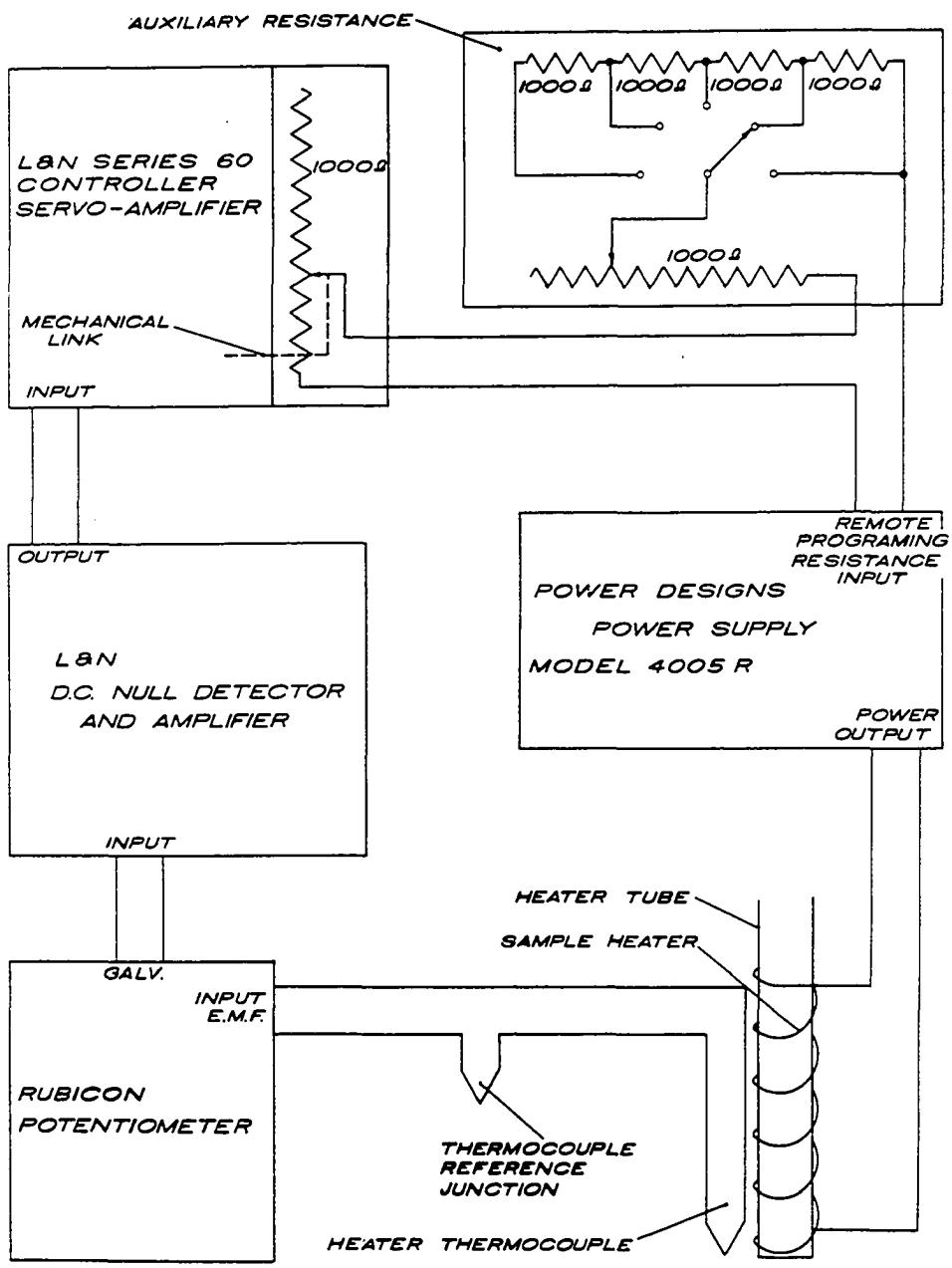

Figure 12. Block diagram of the instrumentation for controlling heater temperature. A second thermocouple and portable potentiometer (not shown) were used to determine the sample temperature.

was used to measure the sample temperature. The sample thermocouple was calibrated by comparing the temperatures obtained in a liquid nitrogen bath, ice bath and room temperature with a published (55) copper-constantan calibration curve. A copper block at room temperature was used as the reference junction. Heater current was supplied by a Power Designs constant-voltage power supply. The series resistances were used to optimize the temperature control at different temperatures. An L&N series 60 controller controlled the output of the power supply. The sample thermocouple voltage was measured on an L&N portable potentiometer (not shown in Fig. 12).

E. Cryostat

Figure 13 shows schematically the cryostat designed by P. H. Sidles to operate down to liquid helium temperatures. For the present experiment, 50°K was the lowest temperature used. This temperature was obtained by pumping on liquid nitrogen. The copper sheet on the jacket surrounding the heater was used to minimize temperature gradients in the sample chamber. The 10 inch spacer at the top of the cryostat could be removed and a tail placed at the bottom so the cryostat could be used in a magnet with no change in the sample holder.

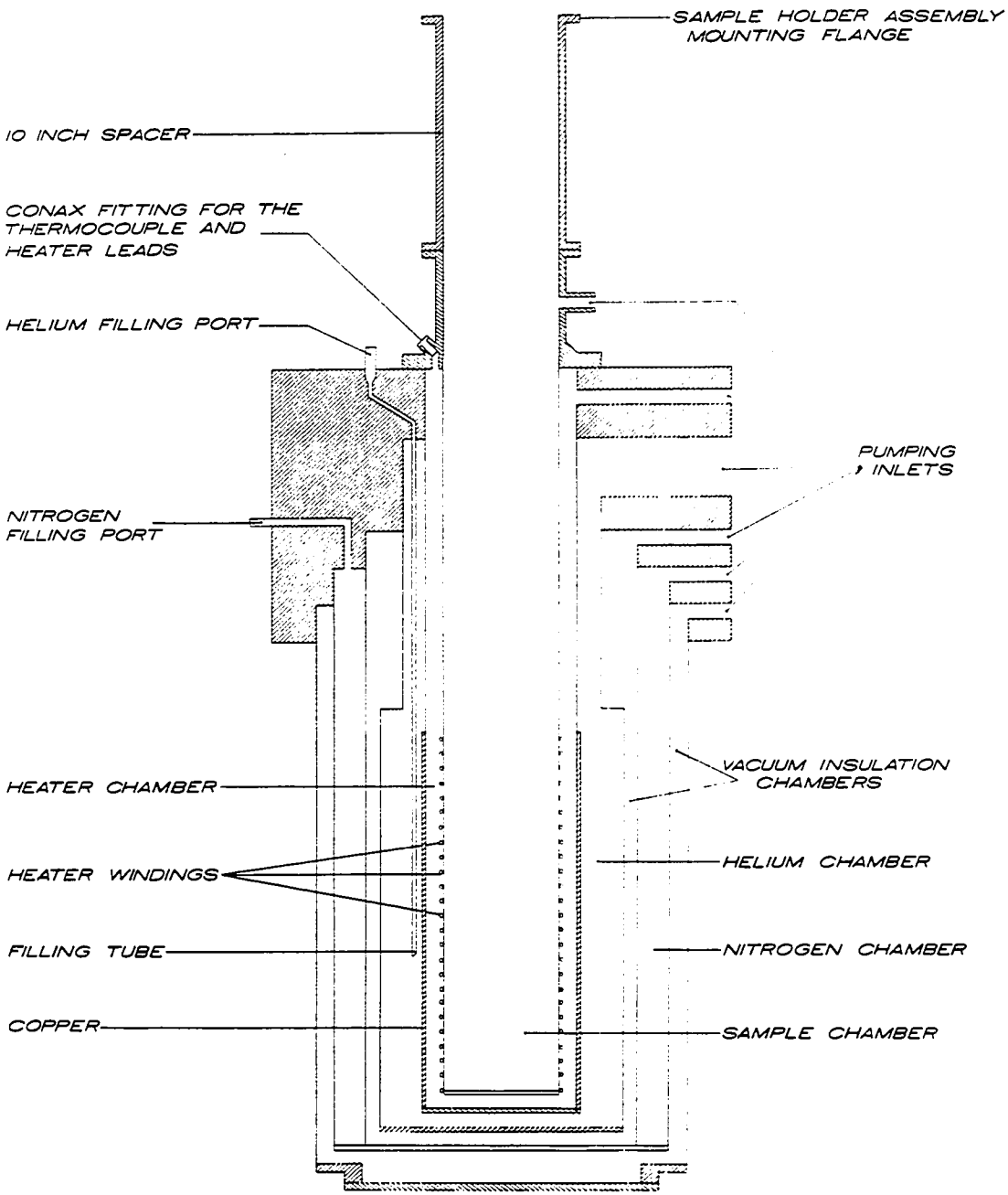

Figure 13. Schematic diagram of the cryostat.

F. Piezoresistance of Germanium

The longitudinal piezoresistance component $\Delta\rho/\rho X = \frac{1}{2}(\pi_{11} + \pi_{12} + \pi_{44})$ was measured on a [110] sample of n-type germanium. The results of this measurement are shown in Fig. 14 along with the results obtained by Morin et al. (48) on a similar sample. The solid line represents the average slope obtained by Morin et al. from data taken in the temperature range 40-120°K. A stressing weight of 1000 grams was used by Morin et al., while for the present data a stressing weight of 1045 grams was used. Because of the agreement with Morin et al., it was felt that our apparatus gave valid results.

Figure 14. A comparison of the data obtained by Morin *et al.* (48) and the data obtained with the apparatus described here and by Temple (67) on similar samples of n-type germanium. The experimental points show the result of measuring the piezoresistance component $\frac{1}{2}(\pi_{11} + \pi_{12} + \pi_{44})$ on a [110] sample. The straight line is the average slope obtained by Morin *et al.* from 40 to 120°K.

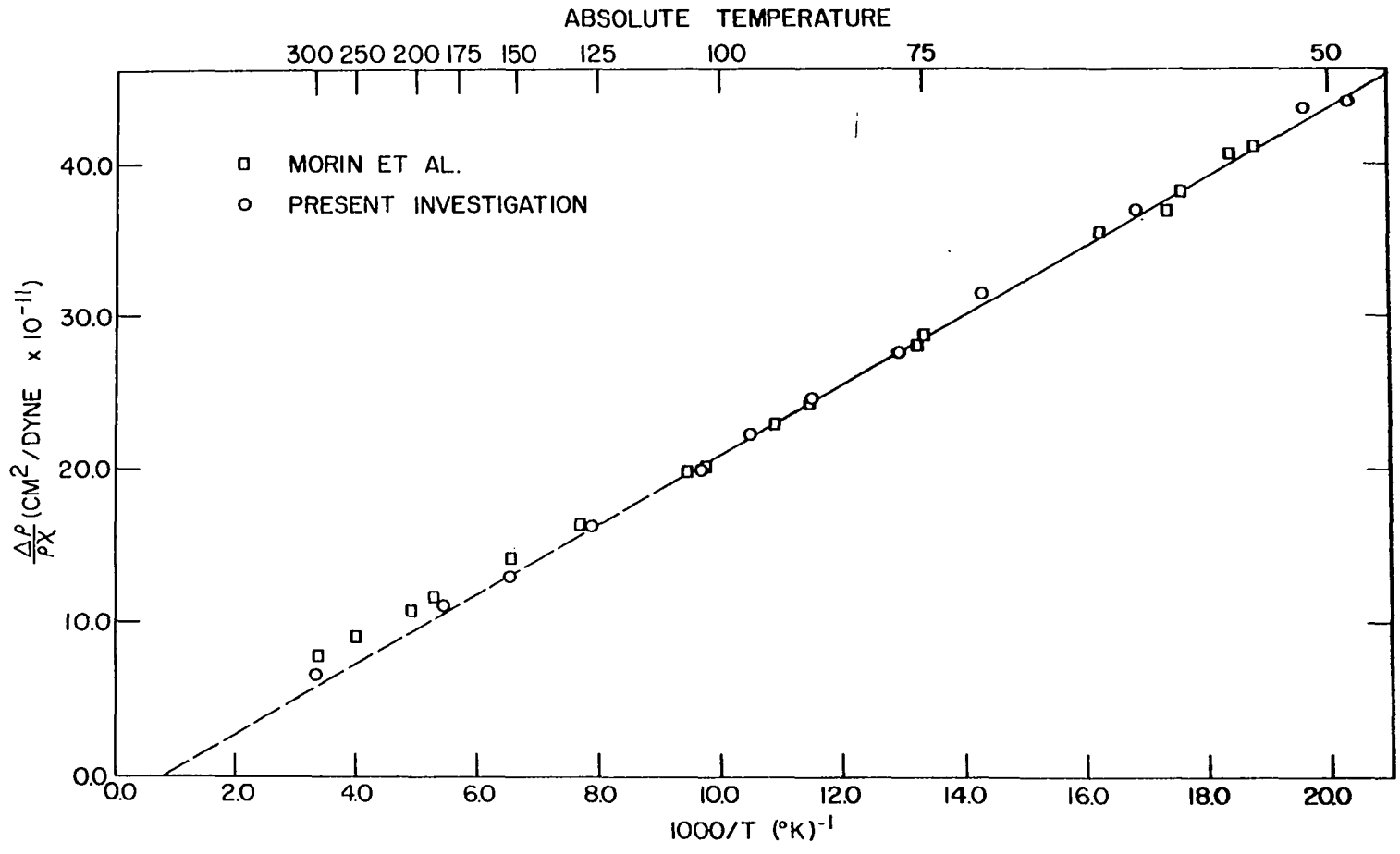
ABSOLUTE TEMPERATURE
300 250 200 175 150 125 100 75 50
MORIN ET AL.
PRESENT INVESTIGATION
$\frac{\Delta\rho}{\rho X}$ (CM^2/DYNE x 10^{-11})
0.0
10.0
20.0
30.0
40.0
0.0 2.0 4.0 6.0 8.0 10.0 12.0 14.0 16.0 18.0 20.0
1000/T (°K)$^{-1}$

V. SAMPLE PREPARATION

Mg_2Sn ingots are not commercially available. The ingots used in this experiment were grown by a Bridgman technique.

A. Growth of Mg_2Sn Ingots

The technique for growing Mg_2Sn crystals was a variation of the techniques used by Morris et al. (49). A stoichiometric ratio of Mg and Sn (two atomic weights of Mg for every atomic weight of Sn) was placed in a graphite crucible. The crucible was placed on a water cooled heat sink inside a resistance wound heater. The heat sink created a temperature gradient across the ingot. The tip of the ingot, which froze first in single crystal form, determined the orientation of the remainder of the ingot. A procedure was developed which produced ingots that were homogeneous, had no eutectic regions and were free of holes. The tips of these ingots were always single crystal. However, the region above the tip usually consisted of a mosaic appearing polycrystalline region (95% of the time). The polycrystalline grains in this mosaic region were misoriented from one another by three degrees or less. Piezoresistance data was taken only with single crystalline samples. Some mosaic crystals were used for the high stress piezoresistance measurements.

Figure 15 shows the graphite crucibles in which the crystals were grown. The results obtained from both

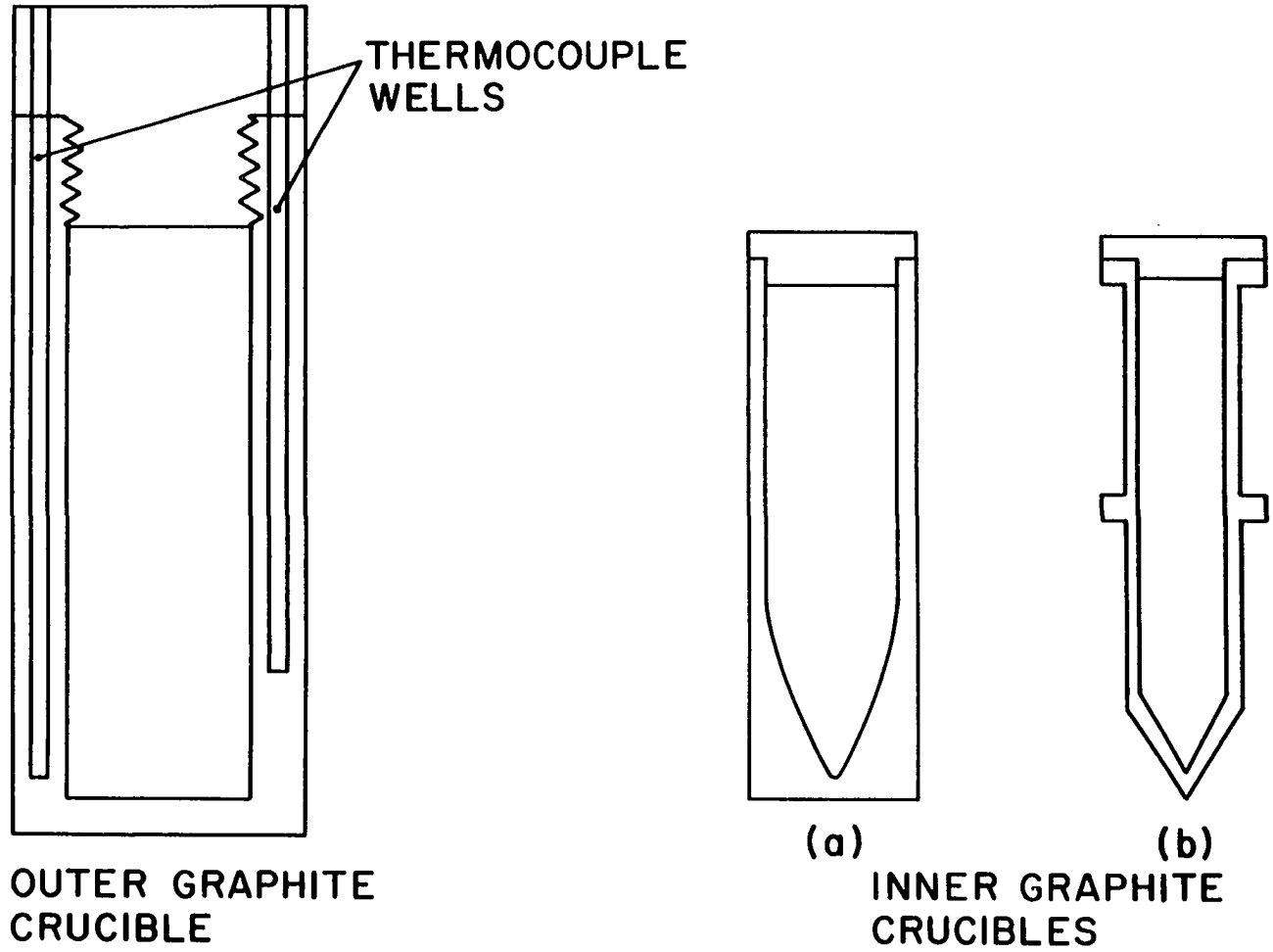

Figure 15. Graphite crucibles used in preparation of Mg_2Sn ingots. The results obtained from both kinds of crucibles (a) and (b) were identical.

crucibles were identical. The crucibles were outgassed in a vacuum of 0.5 microns for one-half hour at a temperature of 1000°C.

Vulcan tin with 99.999% purity was used just as it came from the manufacturer. The Mg used was sublimed from Dow Chemical Mg (99.99% pure) by Donald Grotzky at the Ames Laboratory. After the Mg was sublimed it was kept under a vacuum to minimize the absorption of gases.

Eight to ten per cent more Mg than was necessary for a stoichiometric ratio was added to the melt. At the melting point of Mg_2Sn (780°C), Mg has a vapor pressure of two atmospheres. The excess Mg was used to replace Mg that was lost due to evaporation in the heating process.

In the crucible, tin (melting point 250°C) was placed on top of the Mg (melting point 650°C). As the tin melted it flowed down over the Mg. With this arrangement, the mixing process would commence early in the growth period.

The charged crucible was placed in the Bridgman furnace and a five micron vacuum was maintained on the crucible for at least eight hours. During this time the air surrounding the charge was removed.

The charge was then heated slowly (2 hours) to 350°C while the crucible was still under a vacuum. During this period gases that were absorbed by the charge and crucible were removed. At the same time, the tin slowly flowed over

the Mg. This slow process also helped mix the two elements.

A helium pressure of 40 psi, which was the maximum safe pressure, was then applied to the crucible. This pressure was enough to appreciably reduce the loss of Mg due to evaporation.

The crucible was then heated to 840°C as indicated by the bottom thermocouple in the crucible. At this temperature the compound was formed. The ingot was allowed to soak for 30 minutes. The temperature gradient across the ingot was 50°C. The ingot was then cooled at 15°C per hour down to 650°C as indicated by the bottom thermocouple. If the crucible was then cooled to room temperature; the ingot always had either holes, tin rich eutectic regions or both. Hence the crucible was heated from 650°C back to 840°C and cooled at 5°C per hour to 670°C. It was found that there was no difference in the result if the ingot was annealed at 670°C for 72 hours or immediately cooled to room temperature. In either case, the ingot was cooled from 670°C to room temperature at a rate of 35°C per hour.

B. Shaping of Samples

Two steps were required to get samples of the required orientation (see Fig. 16): first, slabs with [100] oriented faces were cut out of the ingot; and second, from this slab samples with their long axis in either the [100] or [110] directions were obtained. The samples were oriented to within

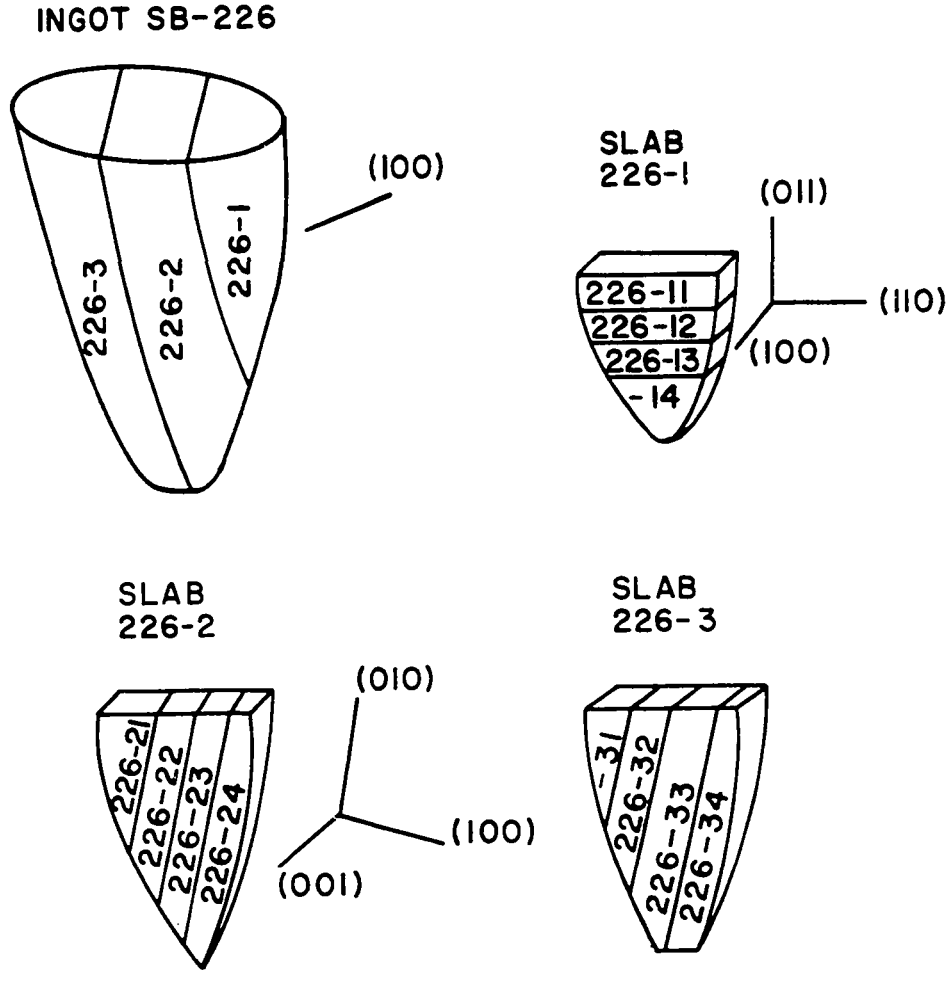

Figure 16. Schematic diagram showing the steps necessary to obtain oriented crystals.

2^{o} of the required orientation by the Laue back-reflection X-ray technique. The ingot was cut with a wire saw. A suspension of 23 micron silicon carbide in kerosene was placed on the stainless steel wire with an eye dropper.

At first a diamond saw was used to cut samples out of the ingot. However, it was found that the diamond saw produced cracks in the ingot. A spark cutter was also tried, but it also produced cracks. The wire saw was definitely most satisfactory.

The two faces of the slabs were lapped parallel to each other with the use of a lapping wheel charged with 23 micron silicon carbide in John Crane lapping vehicle. Samples cut from the slab were hand lapped to their final dimensions. It was very important that the final shaping be done by hand. Samples lapped to their final dimensions with the lapping wheel were found to break easier than samples which were hand lapped.

The final dimensions of the piezoresistance samples were 1.5 x 1.5 x 10 mm.

C. Soldering Techniques

Figure 5 shows the positions of voltage and current contacts on samples used for both transverse and longitudinal measurements.

For the <110> and <111> longitudinal measurements, indium contacts were applied to the samples with an ultrasonic

soldering iron. Gallium voltage contacts and pressure current contacts were used for the <100> longitudinal measurements. Large area, low resistance indium contacts were applied to the transverse samples with the ultrasonic soldering iron.

It was impossible to attach contacts to some samples with the ultrasonic soldering iron. The measured resistivity of these "unstable" samples was a factor of 5 to 20 times greater than the resistivity before soldering to the sample. To eliminate the change in sample resistivity upon soldering, we used gallium solder to apply voltage contacts to the samples. It was discovered that samples with gallium current contacts were electrically noisy when pressure was applied to the sample. We therefore used pressure current contacts for those samples which had gallium voltage contacts. Gallium has a low melting point (29°C) so the samples did not have to be heated to high temperatures ($T > 50^{\circ}C$) to apply the gallium solder. For the "unstable" samples it was necessary to use the low melting point gallium solder to keep from ruining the samples.

Many techniques were tried to attach transverse contacts to the "unstable" samples. The ultrasonic soldering iron was tried with several different solders (indium, 50% lead-50% tin, Woods metal, 90% tin-10% zinc and 70% tin-18% lead-12% indium). In each case the measured resistivity was 5 to 20 times greater than the true resistivity.

We also tried a thin film technique, but the resistance

of the indium and tin thin films was as great as the resistance of the sample. Therefore, these thin films did not satisfy the requirement that the transverse contact have a low resistance.

Evaporating thin films of silver, copper and gold were also tried. However, the noble metals are known acceptors in Mg_2Sn. It was determined that the noble metals were doping the samples.

An electrolytic technique was also tried. However, the solvents for all electrolysis solutions are either an acid or water. Since Mg_2Sn oxidizes very readily, the solvents would react with the surface of the sample.

We also tried making the transverse measurements by applying pressure to the sides of the samples. When pressure was applied, the sides of the sample tended to bow out. Frictional forces at the faces tended to prevent the faces from expanding, while the volume between push rod and pedestal was free to expand. It was found that the piezoresistance effect was non-linear with respect to stress. This non-linearity was attributed to the unknown stresses which were created as the sample bowed out. A very good discussion of the problems involved when the sample bows out is given in a paper by Fritzsche (17).

At this point in our measurements we had no way of attaching transverse leads to the "unstable" samples without

ruining them. It was noticed that samples taken from ingots SB-244, SB-245 and SB-246 (245 group) were very stable. That is, samples from these ingots could be soldered without the samples being ruined. However, samples from ingots SB-246 and SB-244 were all oriented in the <111> direction and could not be used for transverse measurements. There were only four samples from ingot SB-245 and three of these had been used for the longitudinal measurements, but the fourth sample was available for a transverse measurement. This particular sample (SB-245-3) could be soldered successfully with the ultrasonic soldering iron. Figure 17 shows a resistivity curve for the stable samples taken from the 245 group along with the resistivity curves for the "unstable" samples. The "unstable" sample resistivity was larger than the stable sample resistivity. This difference was characteristic of samples taken from ingots SB-199, 226, 228, 234, 251, 260 and 262 (199 group). It was determined that the only difference between the two groups of samples was the method employed to shape the samples. In every case, slabs cut from the ingots were lapped with a mechanical lapping wheel. However, the small samples cut out of the 245 group were hand lapped to their final shape, while the small samples taken from the 199 group were mechanically lapped to 2 x 2 mm pieces and then hand lapped to their final dimension. Samples from ingot SB-276 were mechanically lapped to their final dimension and

Figure 17. Resistivity profiles of stable, "unstable", machine lapped and soldered "unstable" samples. The stable samples were obtained by hand lapping the oriented crystals to their final dimensions. The "unstable" samples were machine lapped to 2 x 2 mm pieces and hand lapped to their final dimension. The machine lapped samples were mechanically lapped to their final dimension. Only the stable samples could be soldered with an ultrasonic soldering iron.

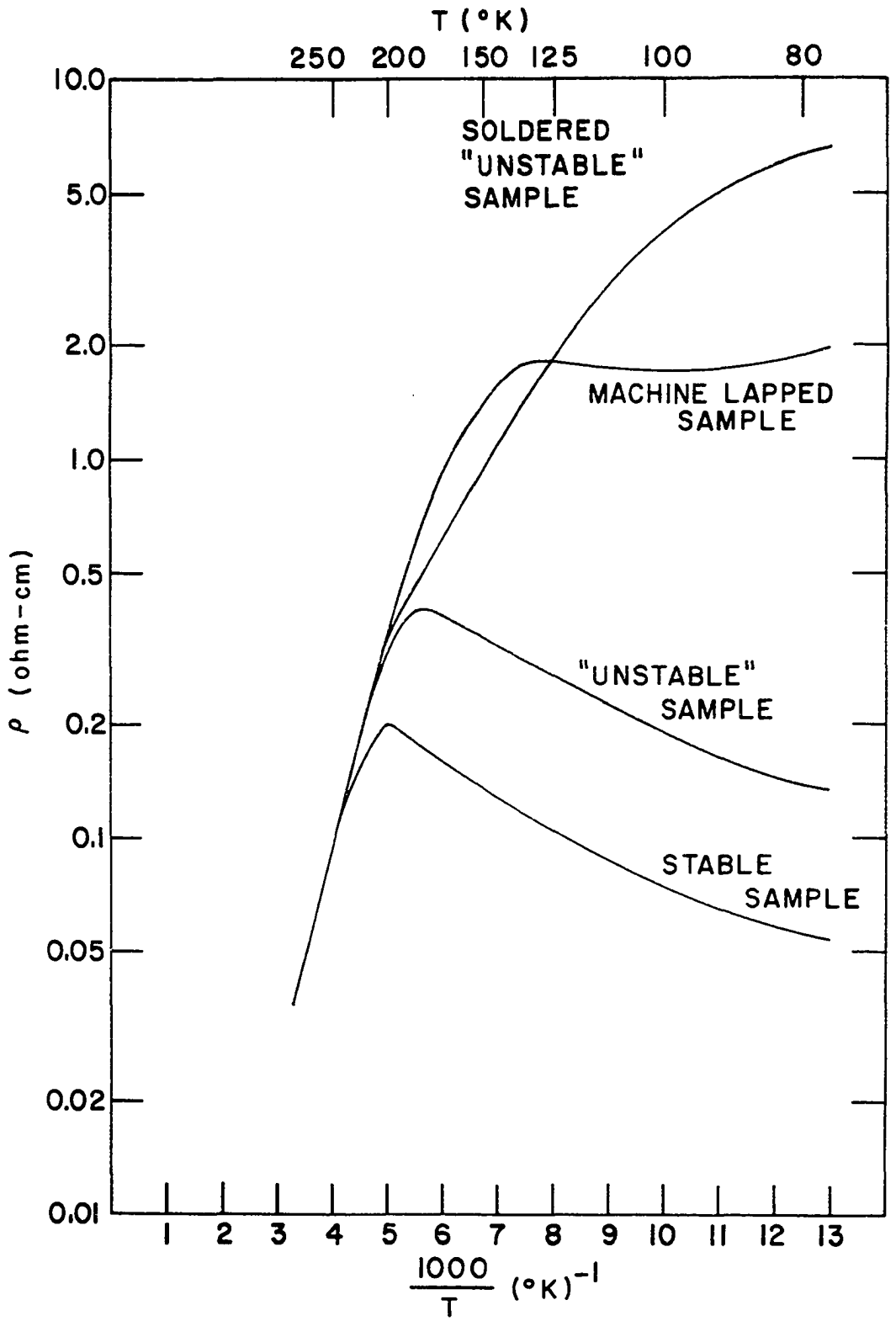
T (°K)
250 200 150 125 100 80
10.0
5.0
2.0
1.0
0.5
0.2
0.1
0.05
0.02
0.01
ρ (ohm-cm)
SOLDERED "UNSTABLE" SAMPLE
MACHINE LAPPED SAMPLE
"UNSTABLE" SAMPLE
STABLE SAMPLE
1 2 3 4 5 6 7 8 9 10 11 12 13
1000/T (°K)⁻¹

found to have resistivities 5 to 6 times larger than the sample resistivities from group 245 (Fig. 17). Samples from LB-1 were hand lapped similar to samples from group 245 and found to have similar resistivity curves. A test was then made on adjacent samples from the same ingot (SB-278). Sample SB-278-1 was lapped in the same manner as were the "unstable" samples from group 199. The same type resistivity curve was found for SB-278-1 as was found for samples in group 199. However, SB-278-2 was hand lapped to its final dimension and its resistivity curve appeared the same as the resistivity curves for samples from group 245. The resistivity of sample SB-278-2 after soldering with the ultrasonic iron was unchanged. However, the resistivity of sample SB-278-1 was a factor of 10 greater after it was soldered.

We concluded that mechanically lapping to the final dimension introduced strains in the sample. Vibrations from the ultrasonic soldering iron completely relaxed these strains in such fashion that small cracks were introduced in the sample. These cracks both increased the resistivity of the sample and created a false change in resistivity when pressure was applied to the sample. Those "unstable" samples which were measured with gallium voltage contacts were free of cracks, although under the influence of internal strains. As a result, the longitudinal measurements made with the "unstable" samples still gave valid piezoresistance results.

We also concluded that the strains introduced by mechanically lapping were not just surface effects. Crystals from group 199 were all hand lapped from a 2 x 2 mm sample down to a 1.5 x 1.5 mm sample. The strains were present throughout the entire sample.

We cannot over emphasize the importance of hand lapping Mg_2Sn samples once they are cut out of the <100> oriented slabs.

VI. SAMPLE CHARACTERIZATION

The electrical resistivity and Hall coefficient of our piezoresistance samples were measured from 77 to 300°K by a standard 5 probe technique. Figures 18 and 19 show the results of these measurements. Because the resistivity curves obtained during the piezoresistance measurements agreed with those obtained during the Hall coefficient measurements, the resistivity curves shown in Fig. 18 are those obtained during the piezoresistance measurements. Figures 20 and 21 show the resistivity and Hall coefficient for the high stress samples.

Table 5 shows the free electron carrier concentration of the piezoresistance samples as determined from the Hall coefficient. The carrier concentration of those samples not shown in Fig. 19 was estimated from a comparison with the resistivity curves shown in Fig. 18.

Figure 18. Electrical resistivity, ρ, of piezoresistance samples.

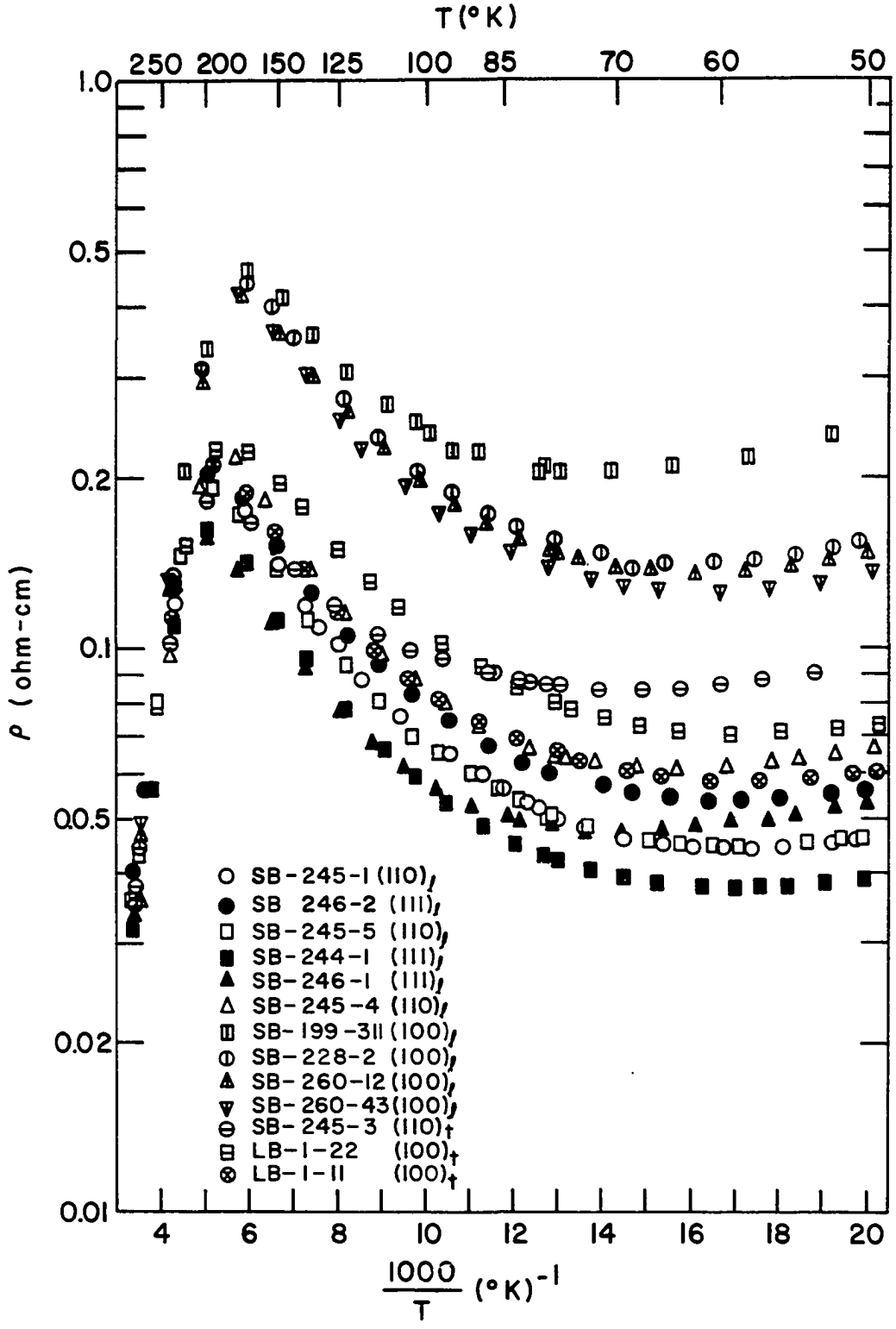
T(°K)
250 200 150 125 100 85 70 60 50
1.0
0.5
0.2
0.1
0.05
0.02
0.01
ρ (ohm-cm)
4 6 8 10 12 14 16 18 20
1000/T (°K)⁻¹
SB-245-1 (110),
SB 246-2 (111),
SB-245-5 (110),
SB-244-1 (111),
SB-246-1 (111),
SB-245-4 (110),
SB-199-311 (100),
SB-228-2 (100),
SB-260-12 (100),
SB-260-43 (100),
SB-245-3 (110)†
LB-1-22 (100)†
LB-1-11 (100)†

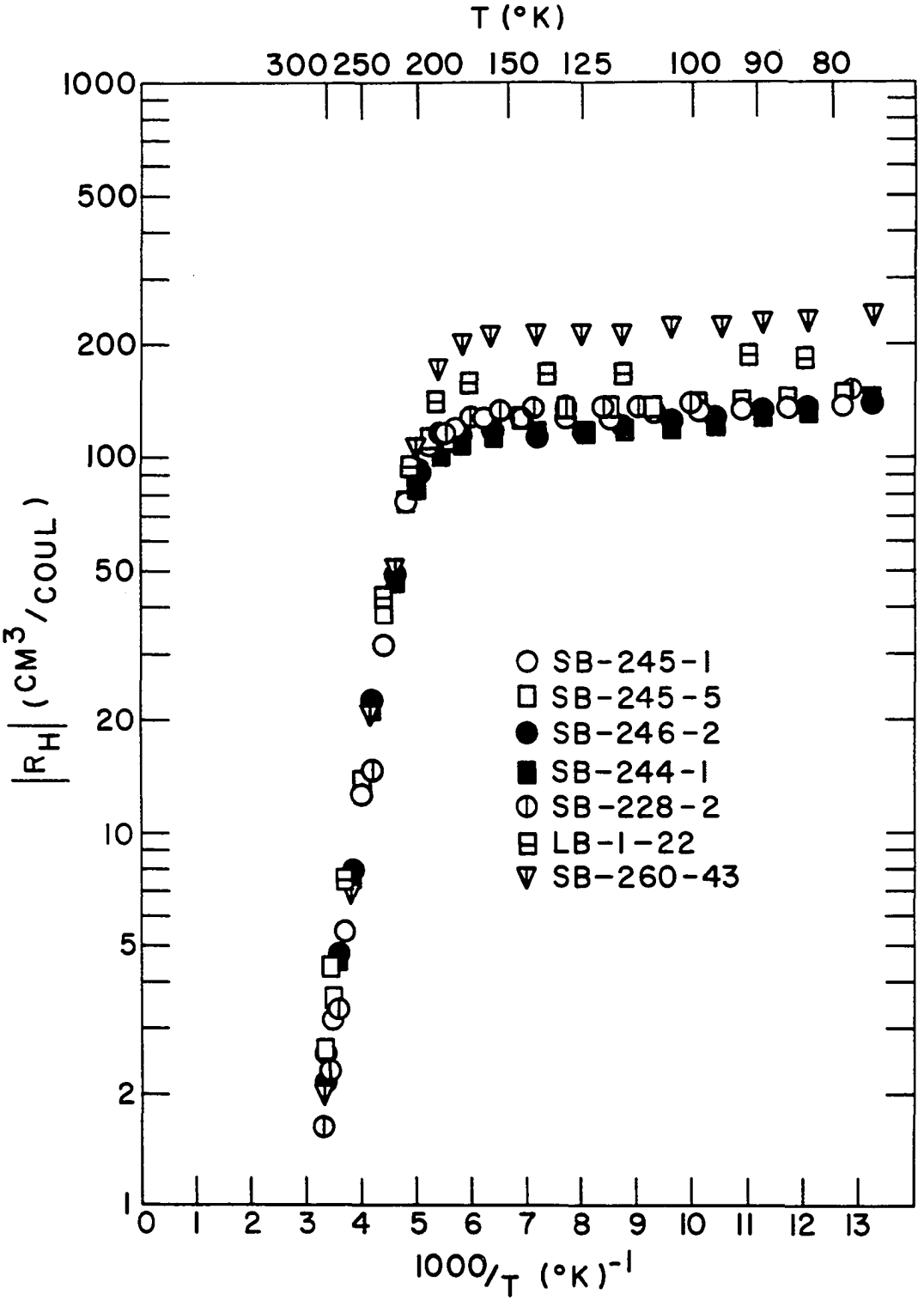

Figure 19. Hall coefficient, R_H, of piezoresistance samples.

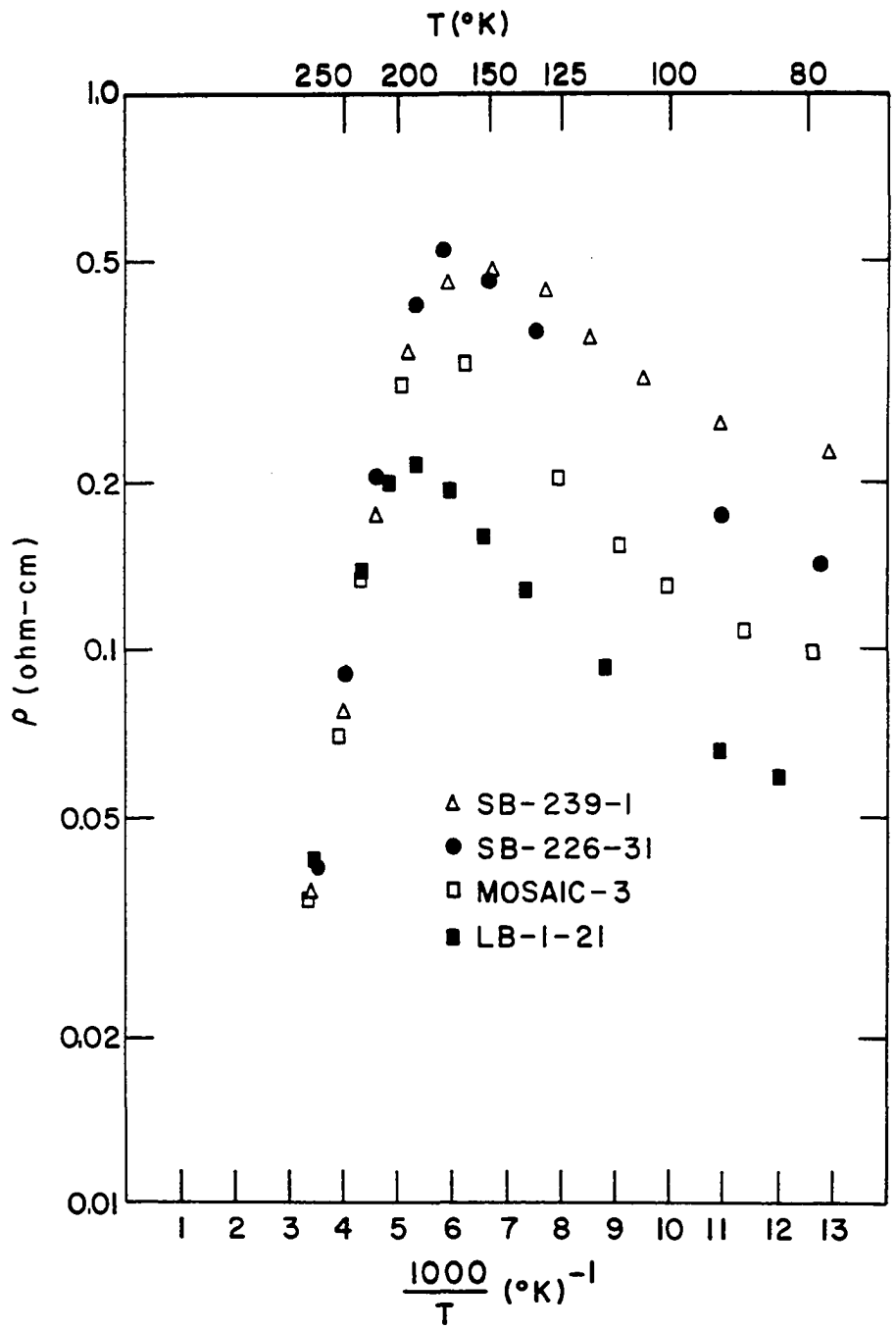

Figure 20. Electrical resistivity, ρ, of high stress samples.

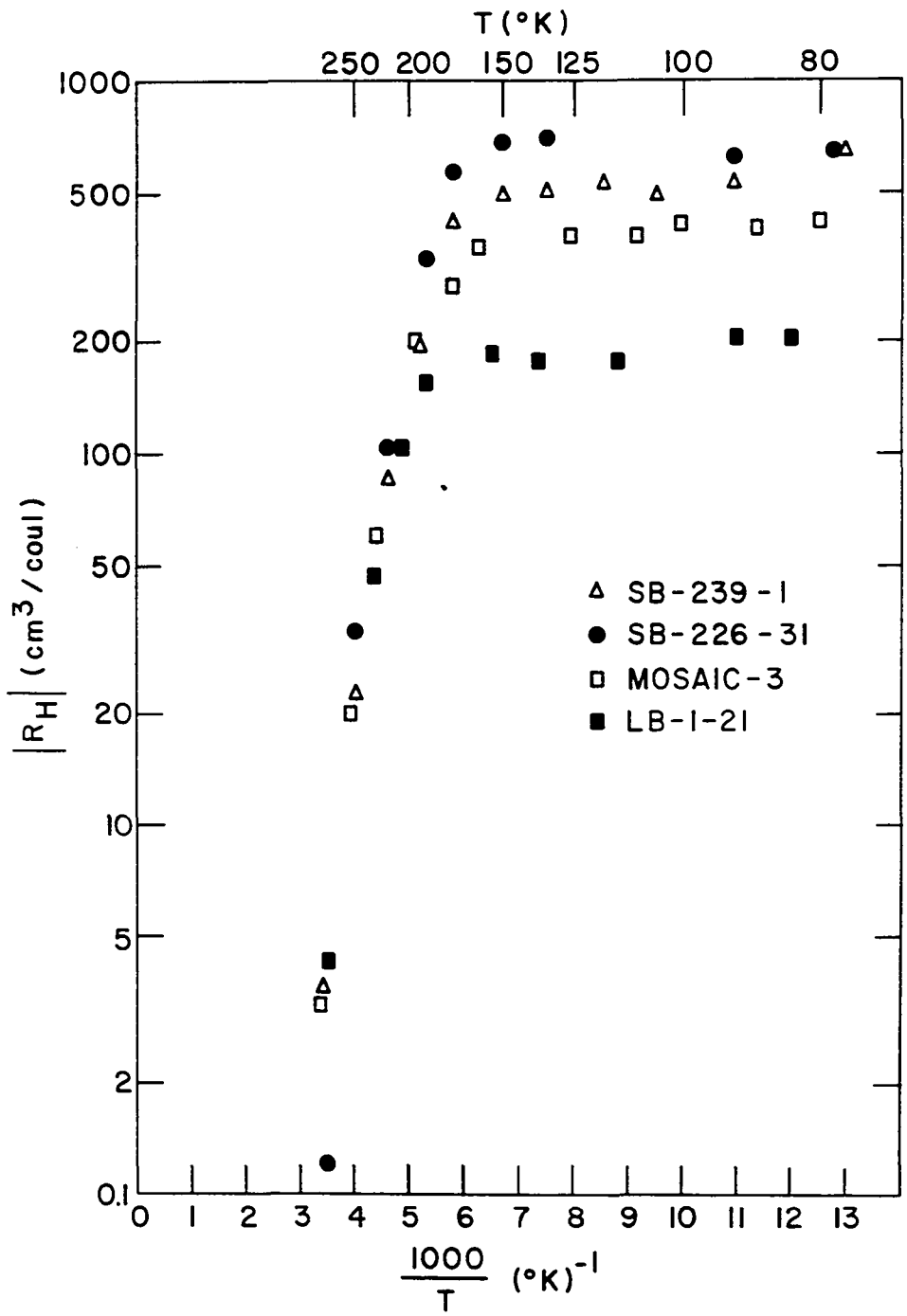

Figure 21. Hall coefficient, R_H, of the high stress samples.

Table 5. Electron carrier concentrations in piezoresistance samples

Sample number	Carrier concentration $\left(10^{16} \frac{\text{carriers}}{\text{cm}^3}\right)$	Sample number	Carrier concentration[a] $\left(10^{16} \frac{\text{carriers}}{\text{cm}^3}\right)$
SB-245-1	6.0	SB-260-12	4
SB-245-5	5.7	SB-245-3	6
SB-246-2	6.3	LB-1-11	5
SB-244-1	6.6	SB-199-311	7
SB-228-2	5.6	SB-246-1	6
SB-260-43	3.5	SB-245-4	6
LB-1-22	4.6		

[a]Carrier concentrations in second column were estimated by comparing resistivity curves.

VII. MEASUREMENTS

A. Measurement Procedure

The measurement procedures for the longitudinal and transverse measurements were identical.

The measurement procedure can best be illustrated by a specific example. Consider sample SB-260-43 which was a <100> oriented crystal on which a longitudinal measurement was made to determine the piezoresistance tensor component π_{11}. The cross sectional dimensions were determined to be 1.482 x 1.523 mm with a traveling microscope. The distance between voltage probes was 4.608 mm.

With the apparatus described in section IV it was possible to directly measure the ratio $\Delta E/E$, where ΔE is the change in sample potential when a stress is applied and E is the unstrained sample potential. The ratio $\Delta\rho/\rho$ is needed to determine the piezoresistance tensor component. However, the $\Delta\rho/\rho$ equals $\Delta E/E$, since the constants needed to convert a resistivity to a potential are present in both the numerator and denominator and cancel.

For this sample the piezoresistance tensor component π_{11} was given by,

$$\pi_{11} = \frac{\Delta\rho}{\rho\chi} = \frac{\Delta E}{E\chi} = \frac{\Delta E}{E} \times 1.586\times10^{-8}\ \text{cm}^2/\text{dyne}, \qquad (84)$$

while the resistivity was given by

$$\rho = \frac{RA}{\ell} = \frac{E}{I}\frac{A}{\ell} = \frac{E}{I} \times 9.900\times10^{-2}\text{cm}^{-1}. \qquad (85)$$

The applied load was 1453 grams (350 mm of Hg).

To start the measurements the strip chart recorder was calibrated as described in section IV. C. For this particular sample the convenient full scale deflection was 60 microvolts. Figure 22 shows a reproduction of the strip chart for measurements at 78.0°K (Fig. 22a) and 100.5°K (Fig. 22b). Tables 6 and 7 show the corresponding data sheets. The page numbers on the strip chart give the location of the original data.

The thermocouple voltage and reference junction temperature were measured both before and after the measurement of ΔE. For these two examples the sample thermocouple voltage remained the same during the measurement procedure and only one value was recorded. The reference junction temperature was given in degrees Fahrenheit.

The symbol ⊗0⊗0 indicates the voltage and current directions in the sample. The current and voltage was reversed by changing the control switch from ⊗0⊗0 to 0⊗0⊗ or vice-versa. Current through the sample was reversed so that temperature-gradient induced voltages present in the sample could be averaged out of the result. The voltage across a strained sample is given by,

$$E_L = IR + I\Delta R + E_t + \Delta E_t, \qquad (86)$$

where R is the unloaded resistance, E_t the thermal voltage and ΔE_t the change in thermal voltage due to an applied stress.

Figure 22. Reproduction of the strip chart for measurements on sample SB-260-43 at (a) 78.0°K and (b) 100.5°K. The page numbers on the strip chart give the location of the original data. Part (a) shows an example where the reference line (0.2 left of center) remained the same during the measurement, while part (b) shows an example where the reference line was drifting during the measurement.

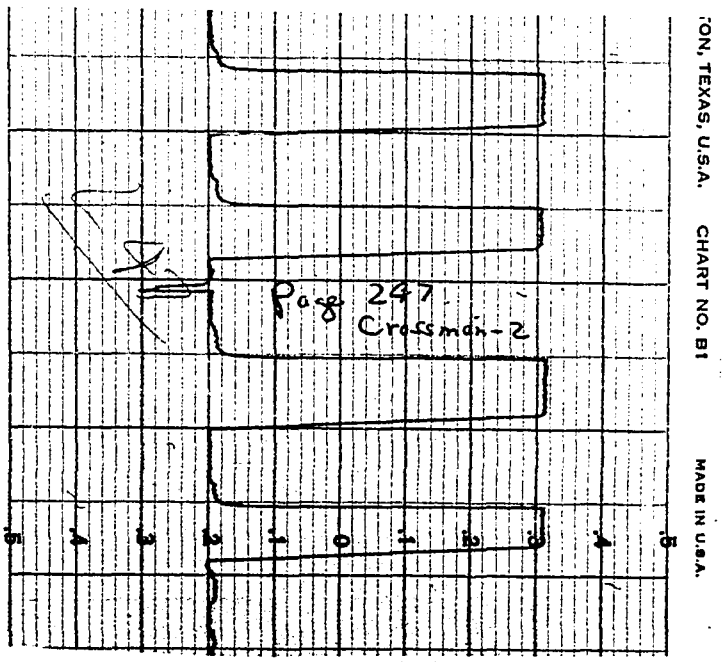
Pad 247
Crossman-2
HOUSTON, TEXAS, U.S.A. CHART NO. B1 MADE IN U.S.A.

(a)

(b)

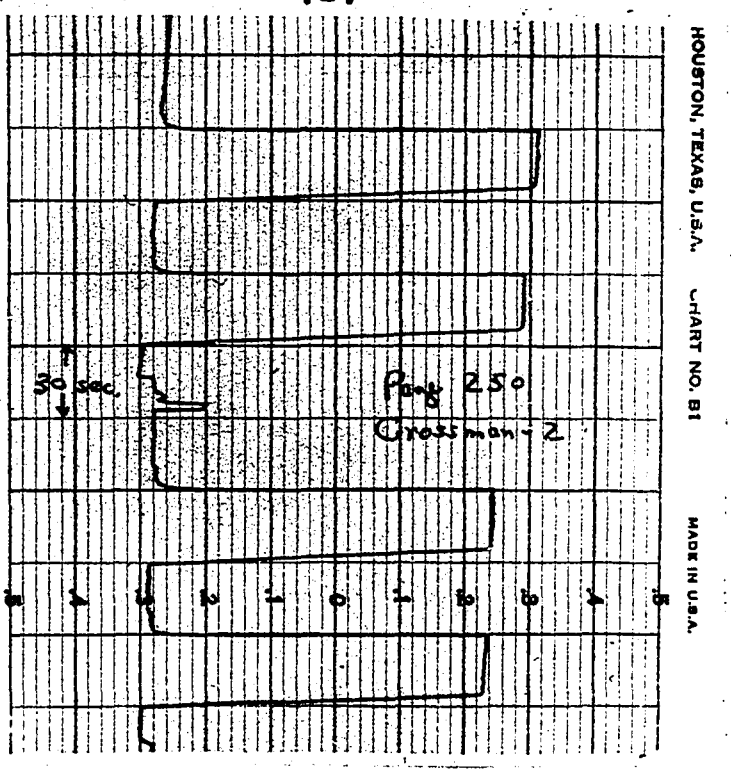
30 sec.
Pad 250
Crossman-2
HOUSTON, TEXAS, U.S.A. CHART NO. B1 MADE IN U.S.A.

Table 6. Actual experimental data taken on sample SB-260-43 at 78°K

0 2 0	Thermocouple voltage	6549 μv
$E = 9.380 \times 10^{-4}$ volts	"Reference junction" Temperature	80.0°F(26.7°C)
-20.0	Sample temperature	78.00°K
31.5		
-20.0 51.5	1000/T	$12.82°K^{-1}$
31.5		
-20.0	Sample current	0.328 ma
	Full scale	60 μv
0 2 0		
$E = 9.336 \times 10^{-4}$ volts		
-20.0		
30.5	Average deflection	51.0
-20.0 50.5		
30.5		
-20.0		

$E_{ave} = 9.358 \times 10^{-4}$ volts

$\Delta E = 30.60$ μv

$\Delta E/E = 32.70 \times 10^{-3}$

$\frac{\Delta \rho}{\rho \chi} = 51.86 \times 10^{-11}$ cm²/dyne

$E/I = 2.851 \frac{\text{volts}}{\text{amps}}$

$\rho = 0.140$ ohm-cm

Table 7. Actual experimental data taken on sample SB-260-43 at 100.5°K

0 2 0 2			Thermocouple voltage	6233
$E = 12.210 \times 10^{-4}$ volts			Reference junction temperature	81.9°F(27.7°C)
-30.0				
	23.5		Sample temperature	100.5°K
-28.5		52.75		
	24.5		1000/T	$9.95°K^{-1}$
-28.0				
			Sample current	0.340 ma
2 0 2 0			Full scale	60 μv
$E = 12.384 \times 10^{-4}$ volts				
-29.5				
	29.0			
-28.5		57.88		
	31.0			
-26.0				
			Average deflection	55.31

$E_{ave} = 12.297 \times 10^{-4}$ volts

$\Delta E = 33.19$ μv

$\Delta E/E = 26.99 \times 10^{-4}$

$\frac{\Delta \rho}{\rho X} = 42.81 \times 10^{-11}$ cm²/dyne

$E/I = 3.617$ volt/amp

$\rho = 0.177$ ohm-cm

E_t and ΔE_t are always in the same direction independent of the current direction. If the current is reversed,

$$E_L = -IR - I\Delta R + E_t + \Delta E_t, \tag{87}$$

and if the voltage is also reversed, the measured voltage is,

$$-E_L = -IR - I\Delta R + E_t + \Delta E_t,$$

or

$$E_L = IR + I\Delta R - \Delta E_t - E_t. \tag{88}$$

When Equations 86 and 88 are added and the result divided by two the final result is

$$E_L - E = \Delta E . \tag{89}$$

The unloaded voltage was recorded for each current direction. In Tables 6 and 7 the unloaded voltage was different for the two current directions. This difference indicated a temperature gradient across the sample.

The strip chart was divided into 100 equal intervals with 50 intervals each side of zero. The strip chart pen could be off-set in either direction so that a deflection of more than one-half scale could be observed.

In Fig. 22a the line marked 0.2 to the left of center was taken to be the reference line for the unloaded position. This reference line corresponded to a -20 in our notation. As the sample was loaded the voltage increased to a value of 0.315 on the strip chart recorder (+31.5 in our notation). The sample was unloaded and the voltage returned to the original reference line. The total deflection was 51.5 units.

The same procedure was repeated a second time. The current and voltage were reversed and the results of two more loadings were recorded. For Fig. 22a and Table 6 the average deflection was 51.0 units. Since full scale was 60 micro-volts, a deflection of 51.0 units corresponded to a ΔE of 30.60 micro-volts. At 78.0°K the ratio $\Delta E/E = 32.70 \times 10^{-3}$ and the piezoresistance effect $\Delta\rho/\rho X = 51.86 \times 10^{-11}$ cm^2/dyne.

For each current direction the current was determined from the measured voltage drop across a 10 ohm standard resistor. For this example, the average current of 0.328 ma gave a resistivity of 0.140 ohm-cm at 78.0°K.

Figure 22b shows an example of a measurement when the sample temperature was changing. The temperature change was not detectable on the thermocouple, but the unloaded reference line was drifting. When the reference line was drifting the loading and unloading sequence was done with equal time intervals. For this particular example (Fig. 22b) the time intervals were 30 seconds. The measured values were recorded at the end of each 30 second interval. For the first loading sequence in Fig. 22b the reference line started at -30. When pressure was applied the voltage increased to +23.0. However at the end of the 30 second interval the voltage read +23.5. The sample was unloaded and the reference line at the end of the 30 second interval was -28.5. The average reference line was -29.25. A deflection of 52.75 units was obtained. When

the sample current was reversed a deflection of 57.88 units was obtained. The difference between the two deflection values indicated a temperature gradient across the sample. The average deflection was 55.31 units. This average deflection gave a ΔE of 33.19 micro-volts. The corresponding piezoresistance effect was $\Delta\rho/\rho X = 42.81 \times 10^{-11}$ cm^2/dyne.

Deflections to the right indicated a positive ΔE, while deflections to the left indicated a negative ΔE. However, it must be remembered that a compressive (or negative) stress was applied to the samples. The two examples considered here show positive deflections, which in reality indicated negative piezoresistance tensor components. The results were $\pi_{11} = -51.56 \times 10^{-11}$ cm^2/dyne at 78°K and $\pi_{11} = -42.81 \times 10^{-11}$ cm^2/dyne at 100.5°K.

For all samples the voltage change caused by the application of a stress was measured as a function of stress at 77°K. The loading weight was varied from 400 to 2000 grams. In all cases the ratio $\Delta E/E$ was linear with respect to stress. Figure 23 shows such a linearity check for sample SB-260-43. Linearity implied that the piezoresistance effect was independent of stress. For all determinations of piezoresistance tensor components, the applied stress was within the linear region.

Samples were also measured as a function of current which showed that the piezoresistance effect was independent of

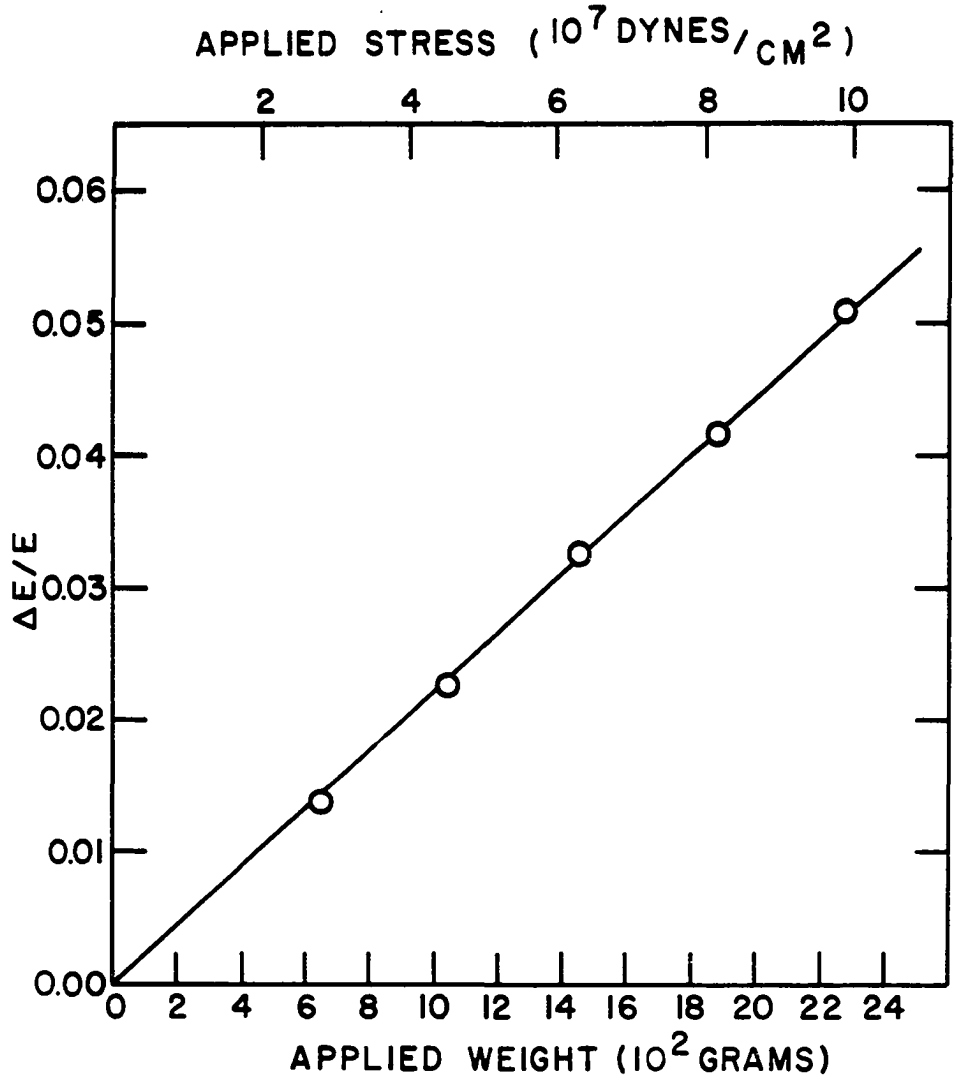

Figure 23. Linearity check for sample SB-260-43 at 77°K. The fact that the experimental points lie on a straight line which passes through zero implied that the piezoresistance effect was independent of stress.

current throughout the range from 0.2 to 1.2 ma.

After each change in load sufficient time was allowed for the sample to regain thermal equilibrium. For most measurements 30 seconds was time enough to establish thermal equilibrium. For longitudinal measurements at temperatures greater than 200°K, 60 to 90 seconds was required to establish thermal equilibrium. Thus, isothermal values of the piezoresistance were obtained.

B. Errors

The uncertainties in this experiment entered through the measurement of the sample cross section, the sample temperature, the applied stress, the change in voltage read on the strip chart recorder, and the unloaded voltage. In addition, a misorientation of the sample introduced a small error.

The sample dimensions were measured with a traveling microscope, which could be read to the nearest 0.001 mm, on all four faces at both ends of the sample. The average measurements for the two sets of parallel sides was used as the sample dimension. A typical standard deviation of the four values used to determine one dimension was $\pm$ 0.005 mm. Thus, the dimensions of the sample were accurate to $\pm$ 0.3% and the cross sectional area accurate to $\pm$ 0.6%.

The sample thermocouple could be read to the nearest micro-volt. The reference junction temperature could be read to the nearest 0.1°F which introduced an error of two micro-

volts in the final thermocouple voltage. At the lower temperatures the thermocouple voltage between two temperatures was 12 micro-volts. An error of three micro-volts in the thermocouple voltage introduced an error of $\pm$ 0.5% in 1/T at 50°K. At higher temperatures the thermocouple voltage between two temperatures was 40 micro-volts. Thus, at 200°K, for example, the error in 1/T was less than 0.1%.

The strip chart recorder could be read to the nearest 0.5 division. For a deflection of one-half scale the uncertainty in reading ΔE was 1.0%. The error in the calibration of the strip chart recorder was limited to the uncertainty in the Wilk potentiometer. The Wilk potentiometer had a stated error of $\pm$ 0.10%.

The unloaded voltage was read directly from the Biddle-Gray potentiometer which had a stated error of $\pm$ 0.01%.

The error in the loading system was determined in section IV. A. to be $\pm$ 0.6%.

The samples were oriented to within 2° of the required orientation. The piezoresistance effect varies as the square of the error angle at the orientation used [see Eqns. 22 and 24 and Smith (64)]. The misalignment caused an error in the longitudinal measurements of $\pm$ 0.1%. For the transverse measurements, two direction cosines are introduced. The misalignment caused an error of $\pm$ 0.2% in the transverse measurements.

The measurements in the intrinsic temperature region were less accurate than the measurements in the extrinsic temperature region. In particular, the transverse measurements in the intrinsic temperature region required a measurement of $\Delta E/E = 5 \times 10^{-4}$, where E = 30 μv. Thus ΔE was on the order of 0.02 μv. So, an error in ΔE of one nano-volt caused an error of 5%. However, the useful information was obtained in the extrinsic region where ΔE/E was greater than 10^{-3} and E greater than 100 μv.

The error in measuring the distance between voltage contacts did not enter into this experiment. The measured result was $\Delta\rho/\rho$. Therefore, an error in ρ due to inaccuracy in the measurement of voltage probe separation is present in both numerator and denominator and cancels.

It is felt that the measurements were accurate to within ± 3% in the extrinsic temperature region.

The above discussion does not include any error which could be introduced by strain inhomogeneities in the sample and misalignment of the sample in the sample holder (probably less than 1°). The voltage probes were placed 1.5 mm away from the ends of the sample to reduce the error caused by strain inhomogeneities.

VIII. RESULTS AND DISCUSSION

A. Piezoresistance Results

Table 8 gives a list of the samples used for piezoresistance measurements. The results of measuring $\Delta\rho/\rho X$ as a function of temperature for these samples are shown in Fig. 24. Table 13 (Appendix) gives some sample data for a $[100]_\ell$, $[100]_t$, $[110]_\ell$, and $[111]_\ell$ sample. The average values of the tensor components π_{11}, π_{12} and π_{44} are shown in Fig. 25. These averages were obtained from a best fit curve through the measured $\Delta\rho/\rho X$ values. The tensor components are tabulated at integral values of 1000/T in Table 14 (Appendix). The tensor component π_{44} was determined from a combination of the quantities π_{11}, π_{12} and $\frac{1}{2}(\pi_{11} + \pi_{12} + \pi_{44})$.

The quantities π_{11} and $\frac{1}{2}(\pi_{11} + \pi_{12} + \pi_{44})$ were obtained from longitudinal measurements on [100] and [110] oriented samples respectively. The component π_{12} was obtained from transverse measurements on [100] oriented samples. These three measurements gave the largest $\Delta\rho/\rho X$ values, and thus gave the most accurate determination of π_{11}, π_{12} and π_{44}.

The average values given in Table 14 were corrected for changes in sample dimensions by a method described by Smith (64) and Potter and McKean (54). For each sample orientation the measured values of $\Delta\rho/\rho X$ were corrected by the addition of the following quantities:

Table 8. Sample orientation and applied stress

Sample number	Sample axis and stress axis	Current direction	Quantity measured	Applied stress (grams)
SB-199-311	100	100	π_{11}	1045
SB-228-2	100	100	π_{11}	1245
SB-260-43	100	100	π_{11}	1453
SB-260-12	100	100	π_{11}	1245
LB-1-11	100	010	π_{12}	1245
LB-1-22	100	010	π_{12}	1245
SB-245-1	110	110	$\frac{1}{2}(\pi_{11}+\pi_{12}+\pi_{44})$	1045
SB-245-4	110	110	$\frac{1}{2}(\pi_{11}+\pi_{12}+\pi_{44})$	1045
SB-245-5	110	110	$\frac{1}{2}(\pi_{11}+\pi_{12}+\pi_{44})$	1045
SB-246-1	111	111	$1/3(\pi_{11}+2\pi_{12}+2\pi_{44})$	1245
SB-246-2	111	111	$1/3(\pi_{11}+2\pi_{12}+2\pi_{44})$	1045
SB-244-1	111	111	$1/3(\pi_{11}+2\pi_{12}+2\pi_{44})$	1045
SB-245-3	110	$\bar{1}10$	$\frac{1}{2}(\pi_{11}+\pi_{12}-\pi_{44})$	1245

$[100]_{\ell}$, $-(S_{11} - 2S_{12})$; $\quad [110]_{\ell}$, $-(\frac{1}{2}S_{44} - S_{12})$;

$[100]_{t}$, $+S_{11}$; $\quad [110]_{t}$, $+(\frac{1}{2}S_{44} + S_{12})$.

The elastic compliances, S_{ij}, were determined from the elastic constants of Davis et al. (12). The transverse measurements are subject to a second correction which arises because the current lines are not straight at the ends of the transverse electrodes. The approximate correction given by Smith (64) is,

Figure 24. Results of measuring $\Delta\rho/\rho X$ as a function of temperature on oriented samples of Mg_2Sn. π_{11} is large and negative; π_{12} is half as large and positive; $1/3(\pi_{11}+2\pi_{12}+2\pi_{44})$, and hence π_{44}, is small in magnitude.

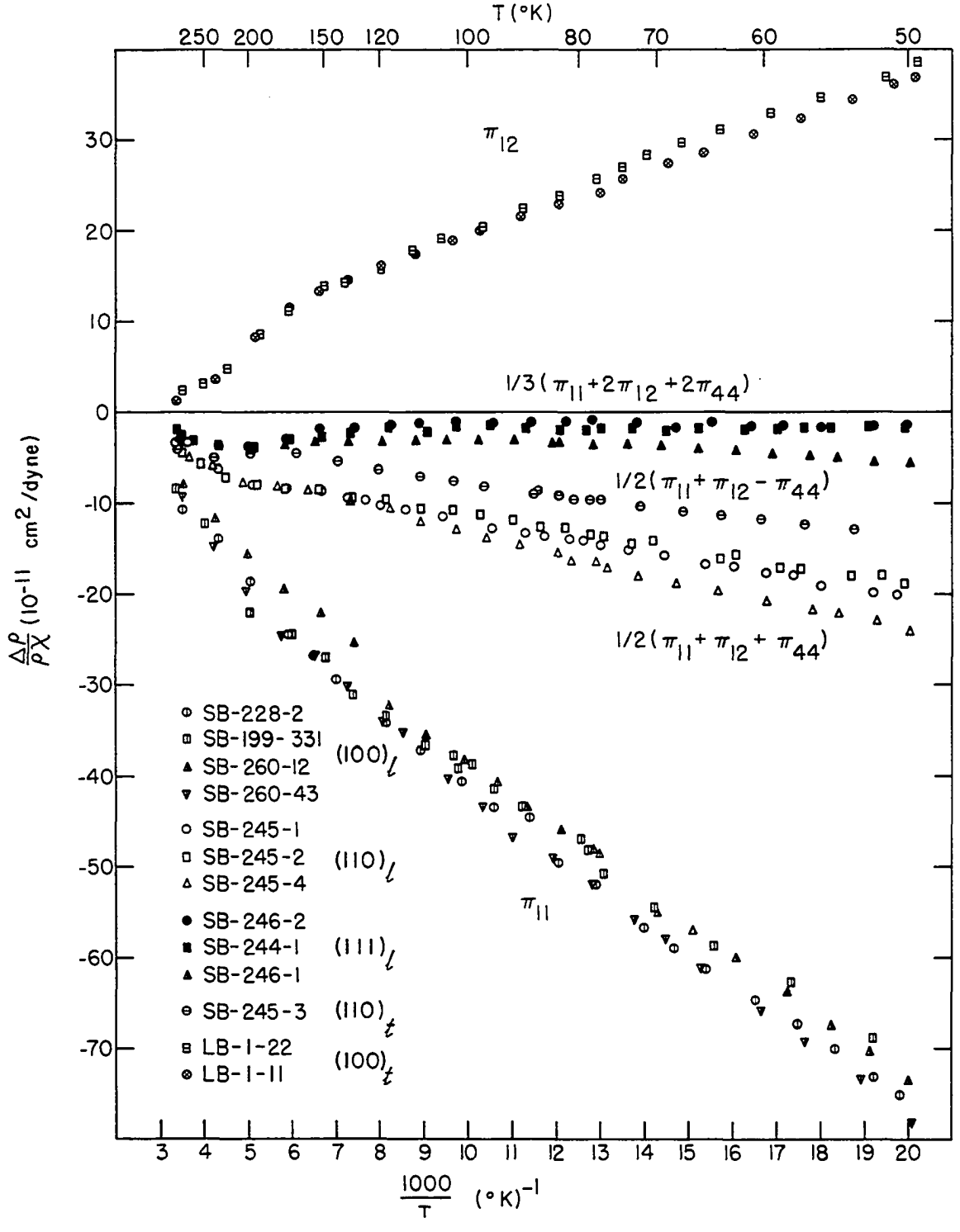
T (°K)
250 200 150 120 100 80 70 60 50
π_{12}
$1/3(\pi_{11}+2\pi_{12}+2\pi_{44})$
$1/2(\pi_{11}+\pi_{12}-\pi_{44})$
$1/2(\pi_{11}+\pi_{12}+\pi_{44})$
π_{11}
SB-228-2
SB-199-331
SB-260-12
SB-260-43
$(100)_l$
SB-245-1
SB-245-2
SB-245-4
$(110)_l$
SB-246-2
SB-244-1
SB-246-1
$(111)_l$
SB-245-3
$(110)_t$
LB-1-22
LB-1-11
$(100)_t$
$\frac{\Delta\rho}{\rho X}$ (10^{-11} cm^2/dyne)
30 20 10 0 -10 -20 -30 -40 -50 -60 -70
3 4 5 6 7 8 9 10 11 12 13 14 15 16 17 18 19 20
$\frac{1000}{T}$ (°K)$^{-1}$

Figure 25. Average values of the piezoresistance tensor components at integral values of 1000/T. These were obtained by drawing a best fit curve through the measured $\Delta\rho/\rho X$ values. The intersections of the best fit curves with integral values of 1000/T were averaged for each component. The component π_{44} was determined by combining the quantities π_{11}, π_{12} and $\frac{1}{2}(\pi_{11}+\pi_{12}+\pi_{44})$.

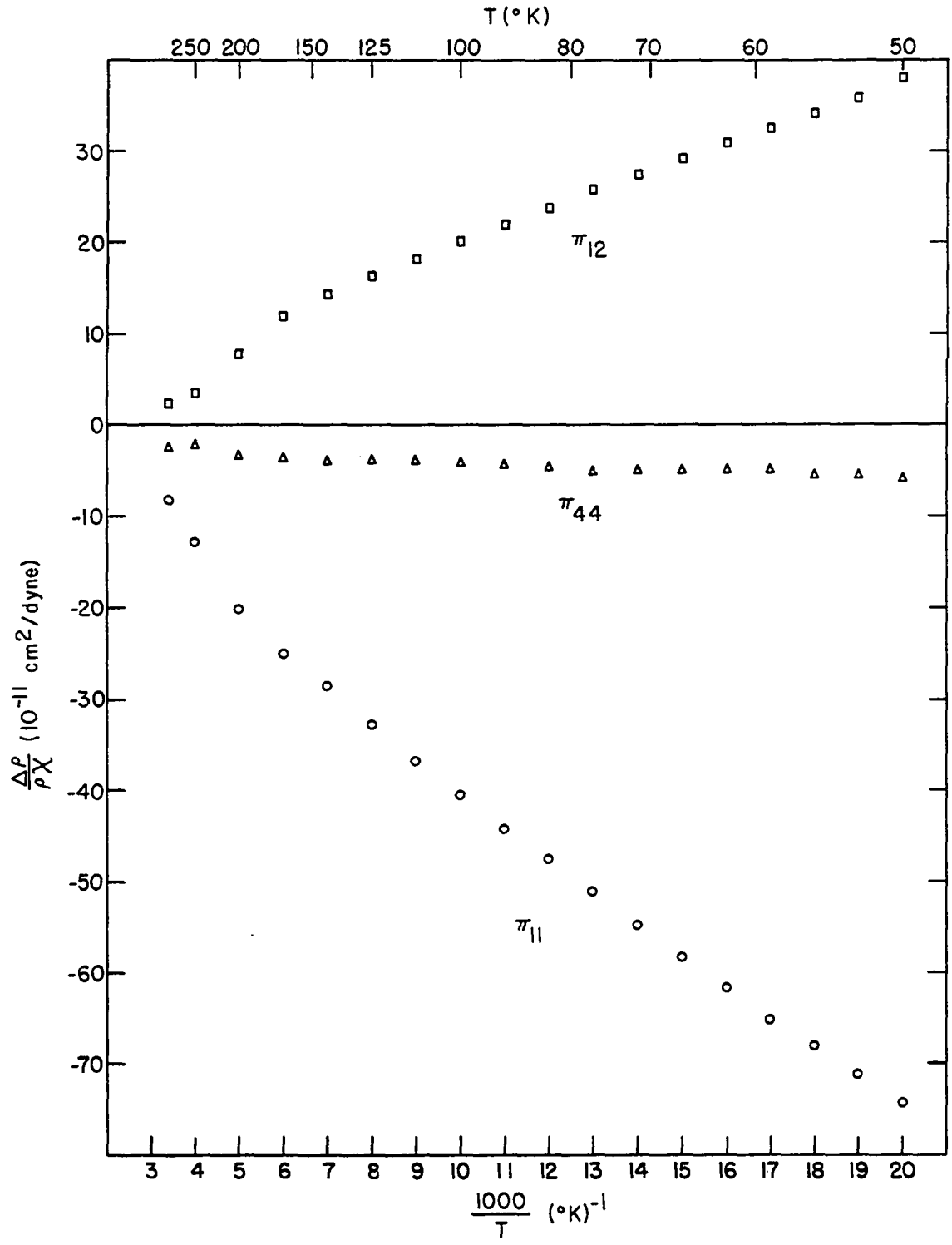
T(°K)
250 200 150 125 100 80 70 60 50
30
20
10
0
-10
-20
-30
-40
-50
-60
-70
π_{12}
π_{44}
π_{11}
$\frac{\Delta\rho}{\rho\chi}$ (10^{-11} cm^2/dyne)
3 4 5 6 7 8 9 10 11 12 13 14 15 16 17 18 19 20
$\frac{1000}{T}$ (°K)$^{-1}$

$$\pi_T = \pi_T(\text{obs}) + \frac{w}{2\pi_T \ell} \frac{(\pi_T - \pi_L)}{\pi_T} \qquad (90)$$

where π_T and π_L are the transverse and longitudinal piezoresistance tensor components, w and ℓ the width and length of the transverse electrode and $\pi_T(\text{obs})$ the observed piezoresistance tensor components. For the $[110]_t$ samples the transverse correction was less than 0.1% and was neglected. For the $[100]_t$ samples the correction was 1% and was included in the results shown in Fig. 25. The corrected average values of the piezoresistance tensor components at integral values of 1000/T are given in Table 9.

For a useful comparison with theory it was necessary to calculate the volume coefficient $(m_{11} + 2m_{12})/3$ and the two shear coefficients m_{44} and $(m_{11} - m_{12})/2$. Thus, the elastoresistance tensor components m_{11}, m_{12} and m_{44} were calculated from the piezoresistance results with Eqns. 33-35 and the elastic constants of Davis et al. (12). Figure 26 shows the elastoresistance tensor components of Mg_2Sn as a function of 1000/T. Figure 27 shows the volume coefficient and the two shear coefficients obtained from the values shown in Fig. 26. Table 10 gives the numerical results shown in Figs. 26 and 27.

Table 9. Corrected average values of piezoresistance components at integral values of 1000/T in units of $10^{-11}cm^2/dyne$

T (^oK)	1000/T (^oK)$^{-1}$	π_{11}	π_{12}	π_{44}	$\frac{1}{2}(\pi_{11}+\pi_{12}+\pi_{44})$	$\frac{1}{2}(\pi_{11}+\pi_{12}-\pi_{44})$	$1/3(\pi_{11}+2\pi_{12}+2\pi_{44})$
50.00	20	-74.38	38.02	-5.92	-21.14	-13.50	-2.93
52.63	19	-71.19	35.96	-5.53	-20.38	-13.02	-2.85
55.56	18	-68.06	34.28	-5.48	-19.63	-12.52	-2.73
58.82	17	-65.21	32.62	-4.97	-18.78	-12.02	-2.67
62.50	16	-61.70	30.89	-5.01	-17.91	-11.51	-2.55
66.67	15	-58.33	29.21	-4.94	-17.03	-11.02	-2.43
71.43	14	-54.80	27.53	-5.01	-16.14	-10.06	-2.33
76.92	13	-51.13	25.82	-5.15	-15.23	-10.00	-2.23
83.33	12	-47.59	23.74	-4.63	-14.24	-9.42	-2.18
90.91	11	-44.23	21.91	-4.30	-13.31	-8.58	-2.13
100.0	10	-40.56	20.03	-4.09	-12.31	-7.75	-2.07
111.1	9	-36.85	18.16	-3.89	-11.29	-6.90	-2.10
125.0	8	-32.85	16.23	-3.90	-10.26	-6.10	-2.30
142.9	7	-28.72	14.29	-4.05	-9.24	-5.25	-2.50
166.7	6	-25.12	11.84	-3.70	-8.49	-4.45	-3.12
200.0	5	-20.20	7.62	-3.40	-7.99	-4.10	-3.90
250.0	4	-12.82	3.38	-2.28	-5.86	-4.70	-3.43
294.1	3.4	-8.25	2.16	-2.76	-4.38	-3.40	-2.53

Figure 26. The elastoresistance tensor components for Mg_2Sn. These were determined from the piezoresistance components in Fig. 25 and the elastic constants of Davis *et al.* (12).

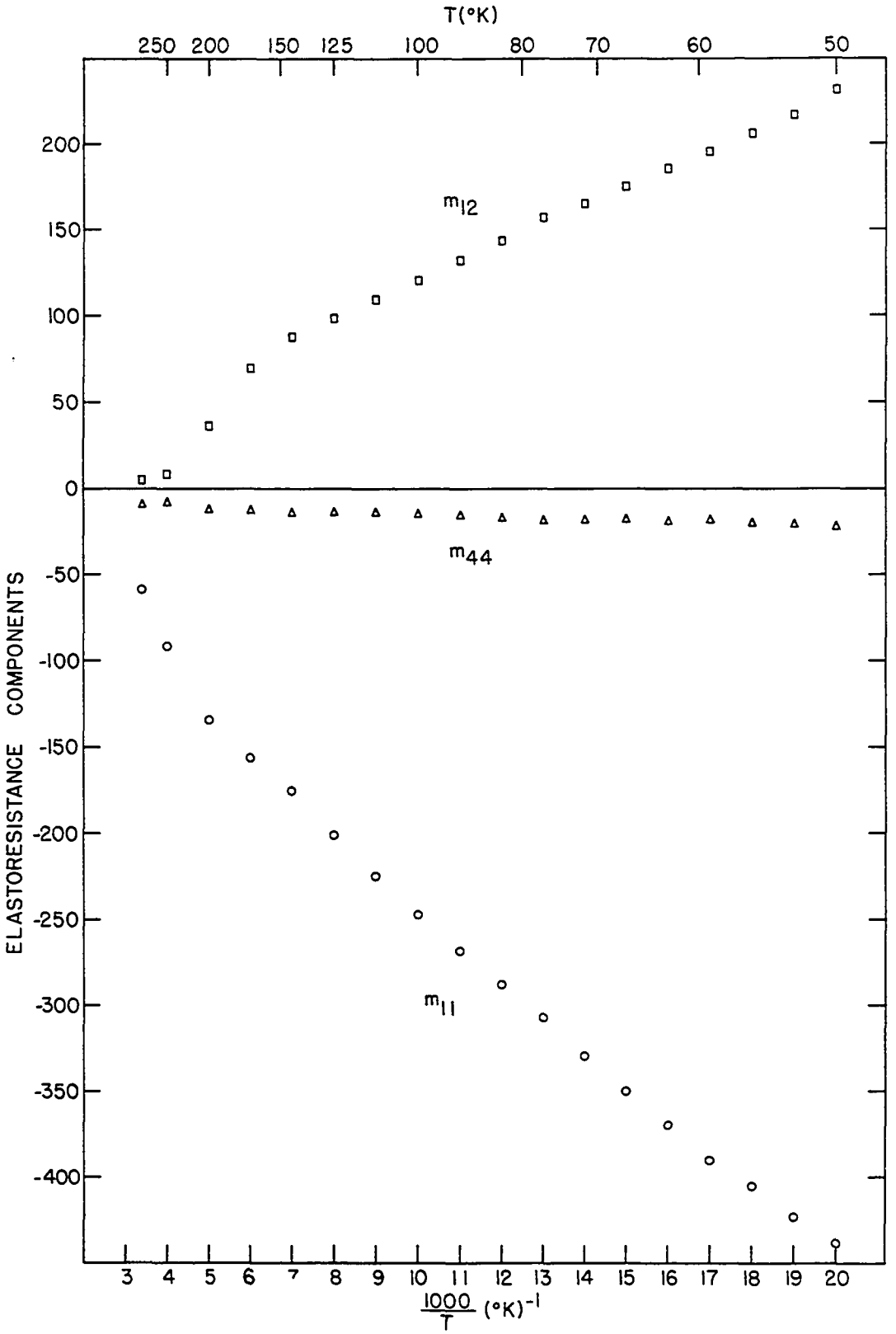
T(°K)
250 200 150 125 100 80 70 60 50
200
150
100
50
0
-50
-100
-150
-200
-250
-300
-350
-400
m12
m44
m11
ELASTORESISTANCE COMPONENTS
3 4 5 6 7 8 9 10 11 12 13 14 15 16 17 18 19 20
1000/T (°K)-1

Figure 27. The elastoresistance coefficients of Mg_2Sn. The volume coefficient, $1/3\ (m_{11} + 2m_{12})$, and one of the shear coefficients, m_{44}, are small and temperature independent in the extrinsic temperature region. The other shear coefficient $\frac{1}{2}(m_{11} - m_{12})$ is large and decreases with decreasing temperature. These results suggest energy ellipsoids in the <100> directions.

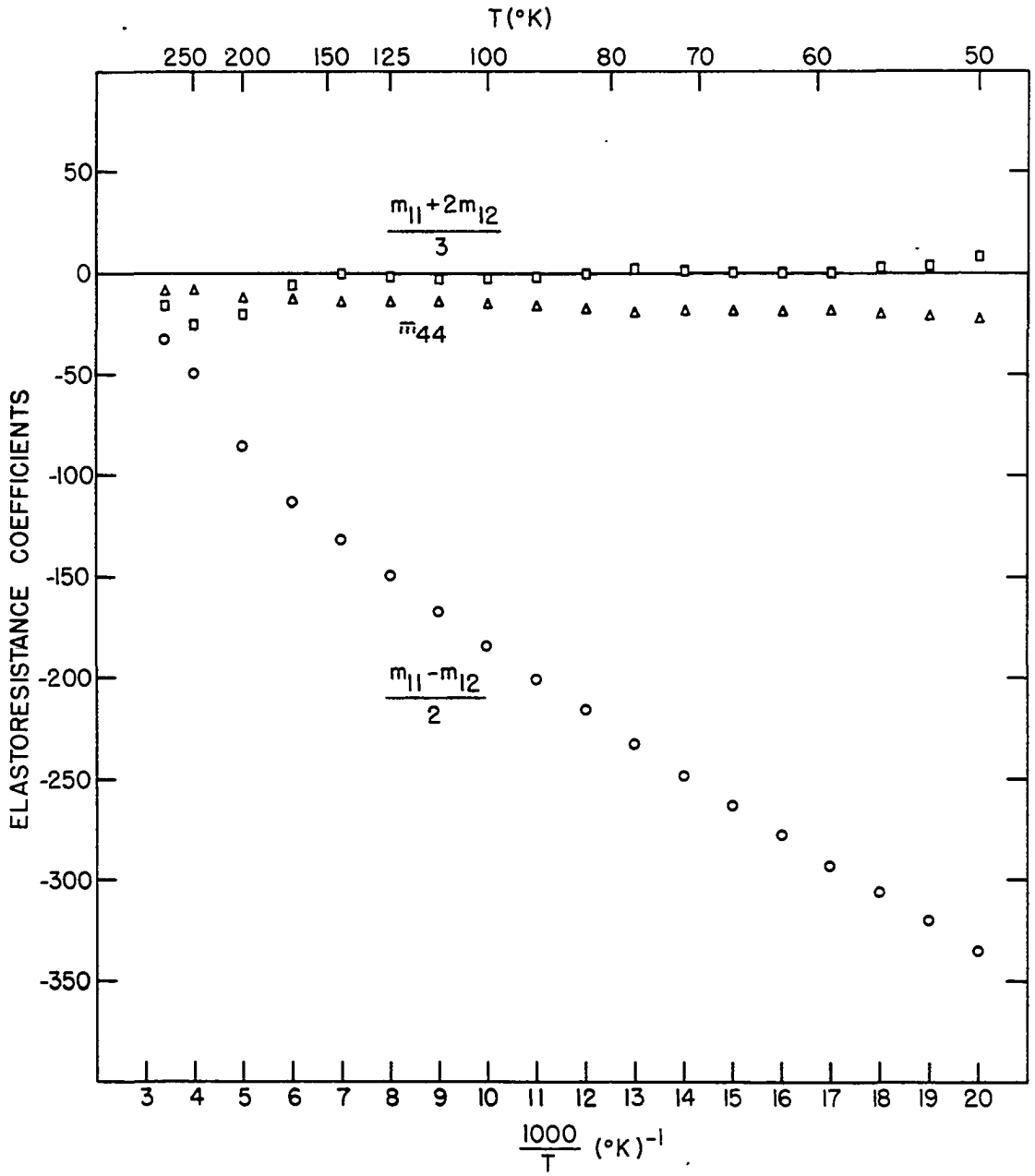
T(°K)
250 200 150 125 100 80 70 60 50
50
0
-50
-100
-150
-200
-250
-300
-350
ELASTORESISTANCE COEFFICIENTS
$\frac{m_{11}+2m_{12}}{3}$
m_{44}
$\frac{m_{11}-m_{12}}{2}$
3 4 5 6 7 8 9 10 11 12 13 14 15 16 17 18 19 20
$\frac{1000}{T}$ (°K)$^{-1}$

Table 10. Elastoresistance coefficients at integral values of 1000/T

T (°K)	1000/T (°K)$^{-1}$	m_{11}	m_{12}	m_{44}	$\frac{m_{11}-m_{12}}{2}$	$\frac{m_{11}+2m_{12}}{3}$
50.00	20	-438.6	231.3	-22.85	-335.0	8.01
52.63	19	-423.1	216.8	-21.29	-320.0	3.50
55.56	18	-405.6	206.4	-20.99	-306.0	2.38
58.82	17	-390.7	195.3	-18.79	-293.0	0.14
62.50	16	-370.3	185.2	-19.09	-277.8	0.33
66.67	15	-350.4	175.7	-18.77	-263.1	0.42
71.43	14	-329.8	166.7	-18.94	-248.2	1.19
76.92	13	-307.5	157.3	-19.42	-232.4	2.32
83.33	12	-288.3	143.4	-17.41	-215.8	-0.49
90.91	11	-268.6	132.2	-16.13	-200.4	-1.38
100.0	10	-247.8	120.6	-15.26	-184.2	-2.21
111.1	9	-225.3	109.2	-14.47	-167.2	-2.32
125.0	8	-201.3	98.1	-14.47	-149.7	-1.69
142.9	7	-175.5	87.3	-14.99	-131.9	-0.60
166.7	6	-156.9	69.3	-13.65	-113.1	-6.12
200.0	5	-134.6	35.9	-12.51	-85.3	-20.90
250.0	4	-91.6	7.8	-8.37	-49.7	-25.25
294.1	3.4	-59.0	5.0	-10.1	-32.9	-16.31

B. Piezoresistance Discussion

In Fig. 25 the three quantities π_{11}, π_{12} and $\frac{1}{2}(\pi_{11} + \pi_{12} + \pi_{44})$ were used to determine the three tensor components $\pi_{11} + \pi_{12}$, and π_{44}. The remaining two measured quantities $\frac{1}{2}(\pi_{11} + \pi_{12} - \pi_{44})$ and $1/3(\pi_{11} + 2\pi_{12} + 2\pi_{44})$ were used for an internal check on the piezoresistance measurements. Figure 28 shows a comparison of the measured quantities $1/3(\pi_{11} + 2\pi_{12} + 2\pi_{44})$ and $\frac{1}{2}(\pi_{11} + \pi_{12} - \pi_{44})$ with the values obtained from the π's shown in Fig. 25. The measured quantity $1/3\ (\pi_{11} + 2\pi_{12} + 2\pi_{44})$ shown in Fig. 28 is the average of longitudinal

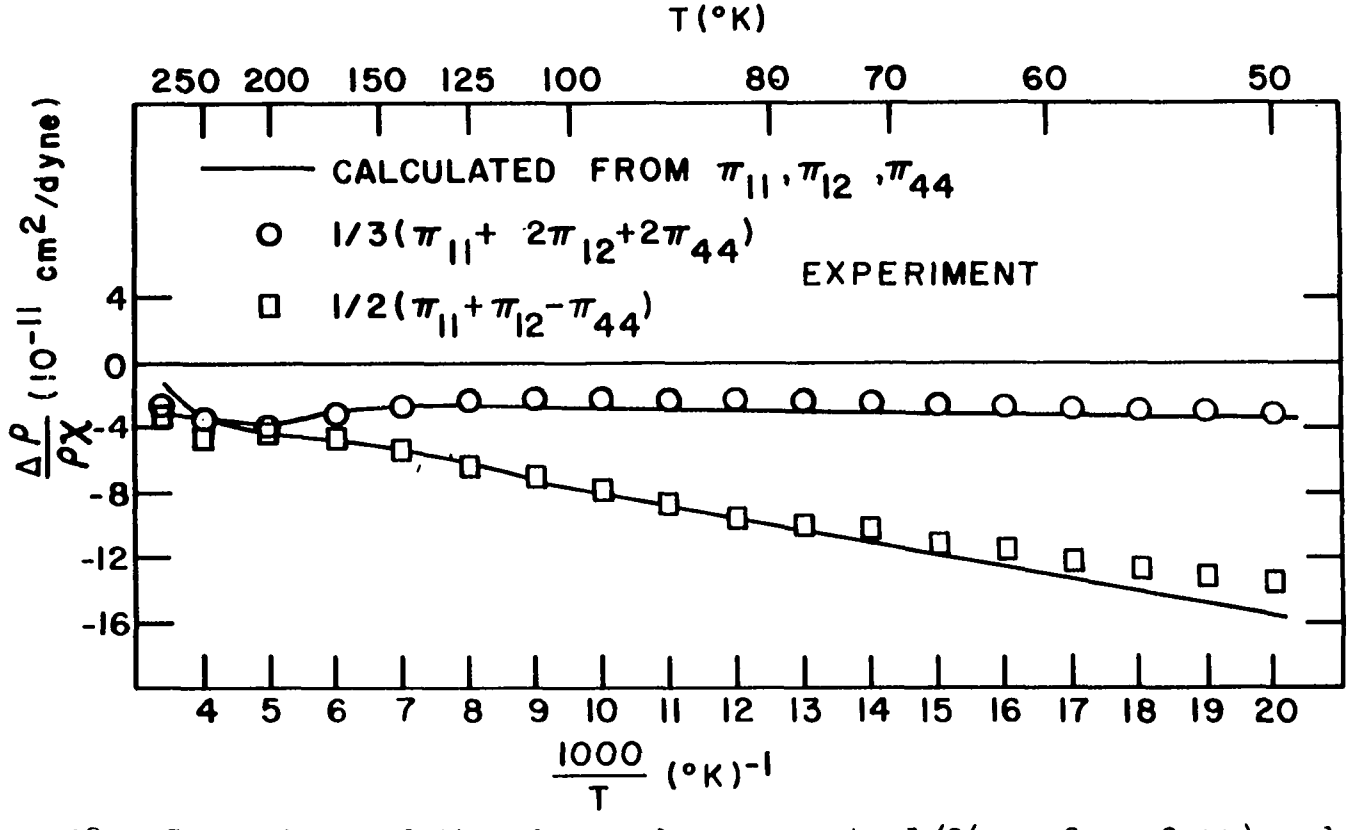

Figure 28. Comparison of the observed components $1/3(\pi_{11}+2\pi_{12}+2\pi_{44})$ and $\frac{1}{2}(\pi_{11}+\pi_{12}-\pi_{44})$ with the values calculated with π_{11}, π_{12} and π_{44} obtained from Fig. 25. The good agreement indicated that the piezoresistance results were internally consistent.

measurements on three [111] oriented samples. There is good agreement between the two $1/3(\pi_{11} + 2\pi_{12} + 2\pi_{44})$ values. The measured quantity $\frac{1}{2}(\pi_{11} + \pi_{12} - \pi_{44})$ is the result of a transverse measurement on one [110] oriented sample. The two $\frac{1}{2}(\pi_{11} + \pi_{12} - \pi_{44})$ values agree in the temperature region 80-200°K and below 80°K they diverge slightly from one another. Two factors which could cause this divergence are (1) transverse measurements are not as accurate as longitudinal measurements, and (2) only one sample was used to measure $\frac{1}{2}(\pi_{11} + \pi_{12} - \pi_{44})$. There is generally, however, good internal consistency within the piezoresistance results.

In section III. A it was shown that, for a many-valley semiconductor with valleys in the <100> directions, the elastoresistance tensor components should be related as follows:

$$\frac{m_{11} + 2m_{12}}{3} = 0,$$

$$m_{44} = 0, \qquad (40)$$

$$\frac{m_{11} - m_{12}}{2} \text{ large.}$$

The results given in Fig. 27 show that the elastoresistance tensor components of Mg_2Sn satisfy the criteria given in Eqn. 40. Thus, it is concluded that n-type Mg_2Sn is a many-valley semiconductor with conduction energy ellipsoids in the <100> direction.

A surprising feature of Fig. 25 is the large magnitude

of the π_{11} tensor component. Whitten and Danielson (75) earlier reported piezoresistance measurements on Mg_2Si. Their results indicate a relatively small magnitude for the piezoresistance tensor component π_{11} in Mg_2Si (see Fig. 29). It was expected that the π_{11} tensor component for Mg_2Sn would be of the same relative size as that of Mg_2Si. However, the π_{11} value of Mg_2Sn is a factor of 10 larger than the π_{11} value for Mg_2Si. Also the magnitude of π_{11} for Mg_2Sn is greater than the largest piezoresistance tensor component reported for other n-type semiconductors. Figure 29 shows the temperature dependence of piezoresistance components for the many-valley semiconductors given in Table 1. In each case the largest tensor component is shown.

Figure 26 shows that both m_{11} and m_{12} are linear with respect to 1/T in the extrinsic temperature region (50-175°K). This linear dependence was predicted in Eqns. 56 and 57,

$$m_{11} = \frac{2}{3} \frac{\Xi_u}{kT} \frac{(1-K)}{(1+2K)} , \tag{56}$$

$$m_{12} = -\frac{1}{3} \frac{\Xi_u}{kT} \frac{(1-K)}{(1+2K)} . \tag{57}$$

Thus, if the mobility anisotropy, K, and the deformation potential, Ξ_u, are independent of temperature, mT should be temperature independent. The mobility anisotropy has been determined by Umeda (74) from magnetoresistance measurements on Mg_2Sn. Figure 30 shows $|m_{11}|$ T, $2m_{12}T$ and $(K - 1)/(1 + 2K)$ as a function of 1000/T. The fact that mT is not exactly

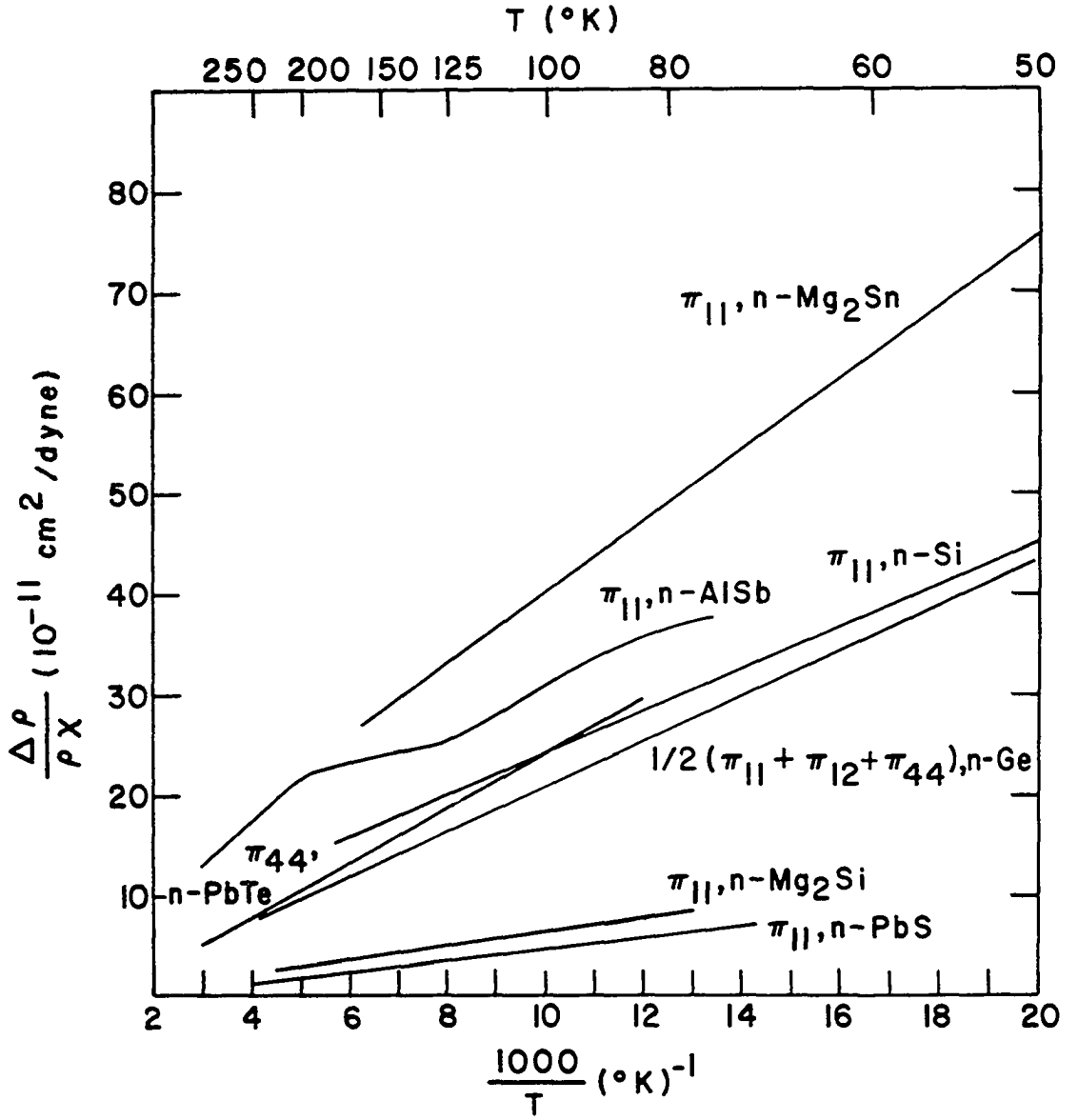

Figure 29. Temperature dependence of the largest observed piezoresistance components for the n-type many-valley semiconductors given in Table 1. The tensor component π_{11} for Mg_2Sn is greater than the largest piezoresistance tensor component reported for other materials.

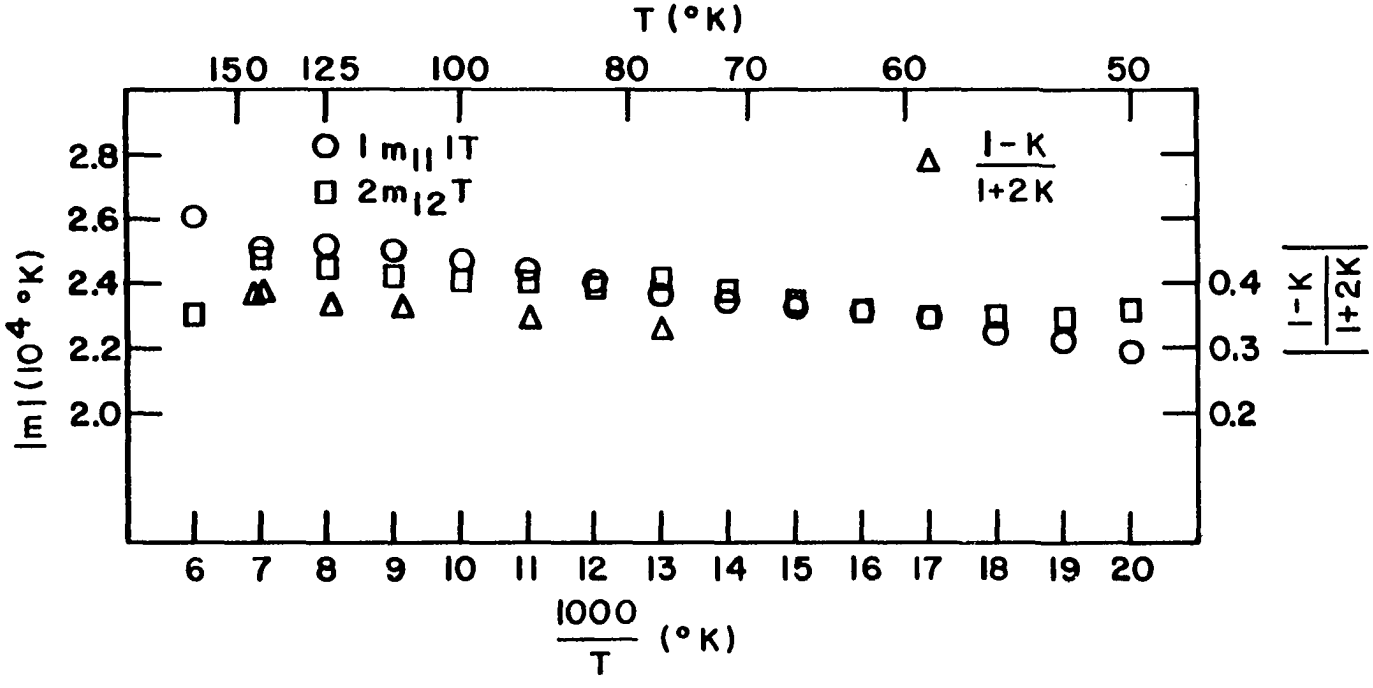

Figure 30. Dependence of mT as a function of 1000/T. The temperature dependence of mT can, in part, be attributed to the temperature dependence of (1-K)/(1+2K).

temperature independent is attributed to the temperature dependence of the mobility anisotropy. Thus, we conclude that not only do the magnitudes of the elastoresistance components satisfy the necessary criterion for a <100> many valley semiconductor, but the elastoresistance components also satisfy the correct temperature dependence.

The linearity of the m's can be used to obtain some information about the importance of inter-valley scattering in Mg_2Sn. In the development of Eqns. 56 and 57 we neglected an inter-valley scattering term (Eqn. 53). We assumed only acoustic mode scattering. Acoustic phonons at low T do not have enough energy to produce inter-valley scattering. However, it may be possible that, at the higher temperature region in the extrinsic temperature region, the phonons acquire enough energy to produce inter-valley scattering. If inter-valley scattering does become important, then the elastoresistance tensor components should decrease more rapidly than 1/T [see Herring (21), Morin et al. (48) and Keyes (33)]. But at higher temperatures the tensor components should again become linear with respect to 1/T. Hall mobility measurements in Mg_2Sn indicate acoustic mode scattering is dominant in the extrinsic temperature region [see Geick et al. (19) and Lichter (43)]. Figure 31 shows the Hall mobility of some samples used in this experiment. It will be noted that in the temperature range 77-175°K the slope of $\ln\mu_H$ versus ln T is

Figure 31. Hall mobility of some piezoresistance samples. The -3/2 slope indicates that acoustic mode scattering dominates in the extrinsic temperature region.

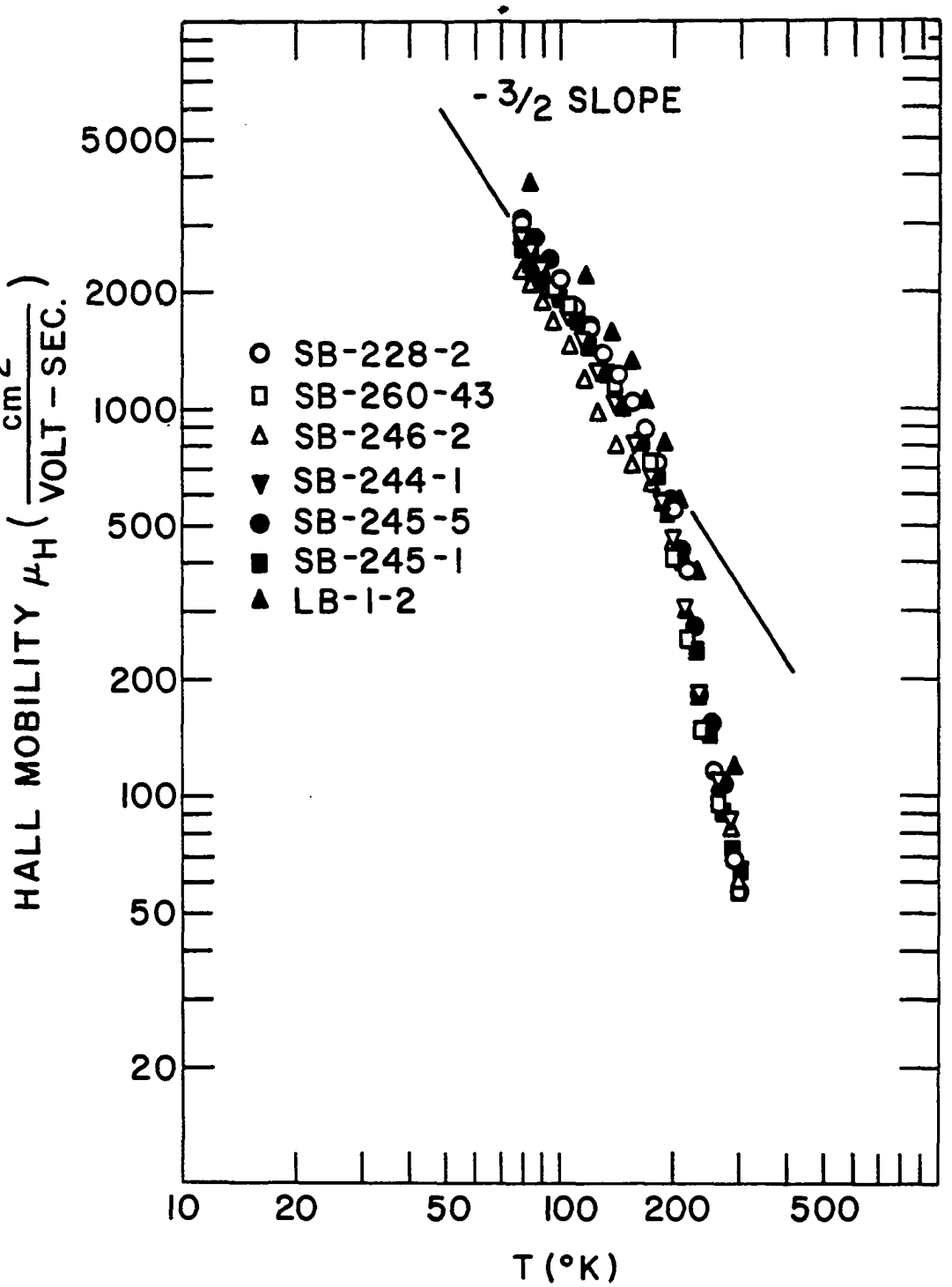
-3/2 SLOPE
SB-228-2
SB-260-43
SB-246-2
SB-244-1
SB-245-5
SB-245-1
LB-1-2
HALL MOBILITY μ_H ($\frac{cm^2}{VOLT-SEC.}$)
5000
2000
1000
500
200
100
50
20
10
20
50
100
200
500
T (°K)

nearly -3/2. The -3/2 slope indicates acoustic mode scattering. In Fig. 26, m_{12} shows no deviation from linearity in the temperature range 60-175°K. However, the m_{11} shows a small deviation at T = 125°K. From 145-180°K the m_{11} is again linear. This small deviation from linearity could be explained in terms of inter-valley scattering. However the deviation is small and we conclude that inter-valley scattering in Mg_2Sn is indeed unimportant in the extrinsic temperature range.

At temperatures above 175°K there is a very rapid decrease in m_{11} and m_{12} as functions of 1/T. However, this rapid decrease cannot be attributed to inter-valley scattering. Above 175°K Mg_2Sn enters into the intrinsic temperature region (see Fig. 18). At this point electrons are being thermally excited from the valence band into the conduction band. As a result, part of the conduction process is due to holes in the valence band. In the intrinsic temperature region the total conductivity is given by,

$$\sigma = \sigma_h + \sigma_e$$

where σ_h and σ_e are the conductivities of holes and electrons respectively. The fractional change in conductivity is given by

$$\frac{\delta\sigma}{\sigma} = \frac{\delta\sigma_h + \delta\sigma_e}{\sigma_h + \sigma_e} \quad .$$

A comparison of our piezoresistance measurements on n-type

Mg_2Sn with the piezoresistance measurements on p-type Mg_2Sn by Kaiser and Kearney (29) reveals that $\delta\sigma_h \ll \delta\sigma_e$. Thus, we have

$$\frac{\delta\sigma}{\sigma} \approx \frac{\delta\sigma_e}{\sigma_n + \sigma_e} < \frac{\delta\sigma_e}{\sigma_e} .$$

So, as the number of holes increased the magnitude of $\delta\sigma/\sigma$ (or m_{11}) should decrease more rapidly than expected if $n_h \ll n_e$. Martin's[1] calculations on the number of carriers in n-type Mg_2Sn show that at 200°K, 15% of the carriers are holes, while at 300°K, 49% of the carriers are holes. We extended the extrinsic linear region of m_{11} to $1000/T = 3$ and found that the experimental points in the intrinsic region deviated from this straight line by 6% at 200°K and 45% at 300°K. We concluded that the rapid decrease of m_{11} and m_{12} in the intrinsic temperature region was due to the fact that the hole conductivity was insensitive to pressure and only a fraction of the charge carriers were affected by the application of pressure.

The small value of $(m_{11} + 2m_{12})/3$ is understood when it is remembered that the volume coefficient represents the change in resistivity under an applied hydrostatic stress.

---

[1]Martin, J. J., Iowa State University, Ames, Iowa. Private communication. 1967.

Under hydrostatic stress all valleys are affected in the same manner and there is no transfer of electrons from one valley to another. It is true that hydrostatic stress will change the energy gap of a semiconductor [Ziman p. 44 (77)] and one might expect a change in resistance in the intrinsic temperature range. In the extrinsic temperature range, however, the temperature is low enough to freeze out thermally induced carriers from the valence band. Thus, in the extrinsic temperature range the application of a small hydrostatic stress (less than 10^8 dynes/cm^2) will not cause a change in the density of free electrons in any valley. Any change in resistivity with hydrostatic pressure must be caused by a change in mobility and not in the number of free electrons. Because the volume coefficient is small, the change in mobility is small with respect to a change in volume. In the intrinsic temperature range above 175°K the deviation of the volume coefficient from zero can be attributed to a change in the energy gap with hydrostatic pressure.

Whitten and Danielson (75) indicate that it is probable that the intercepts with 1000/T = 0 of the two shear coefficients [-11 for m_{44} and -16 for (m_{11} - $m_{12}/2$]represent the change in mobility with respect to the two shear strains. Since the intercepts of the two shear coefficients are larger than the intercept of the volume coefficient it appears that a shear strain would introduce a greater change in the

mobility than would the application of a hydrostatic stress.

If electrons are scattered by ionized impurities, their mobility and, hence, the ratio (1 - K)/(1 + 2K) would be reduced. Thus, if ionized impurity scattering becomes important the magnitude of the elastoresistance components should decrease. The deviation from linearity of m_{11} at temperatures below 60°K can be explained, in part, by the onset of ionized impurity scattering [see Herring (21) and Morin et al. (48)].

C. Deformation Potential Results

The deformation potential can be determined from piezoresistance measurements if the mobility anisotropy is known. Umeda (74) has deduced the mobility anisotropy for Mg_2Sn from his magnetoresistance measurements (see Fig. 32b). With these values of K, Eqns. 56 and 57,

$$m_{11} = \frac{2}{3} \frac{\Xi_u}{kT} \frac{(1-K)}{(1+2K)}, \tag{56}$$

$$m_{12} = -\frac{1}{3} \frac{\Xi_u}{kT} \frac{(1-K)}{(1+2K)}, \tag{57}$$

were used to determine the deformation potential Ξ_u. Table 11 shows the deformation potential as calculated from both Eqns. 56 and 57 along with the average result. It was necessary to use both Eqns. 56 and 57 because both m_{11} and m_{12} depend on π_{11} and π_{12}. Hence it cannot be said that the value for m_{11} is more reliable than the value for m_{12} or vice-versa even

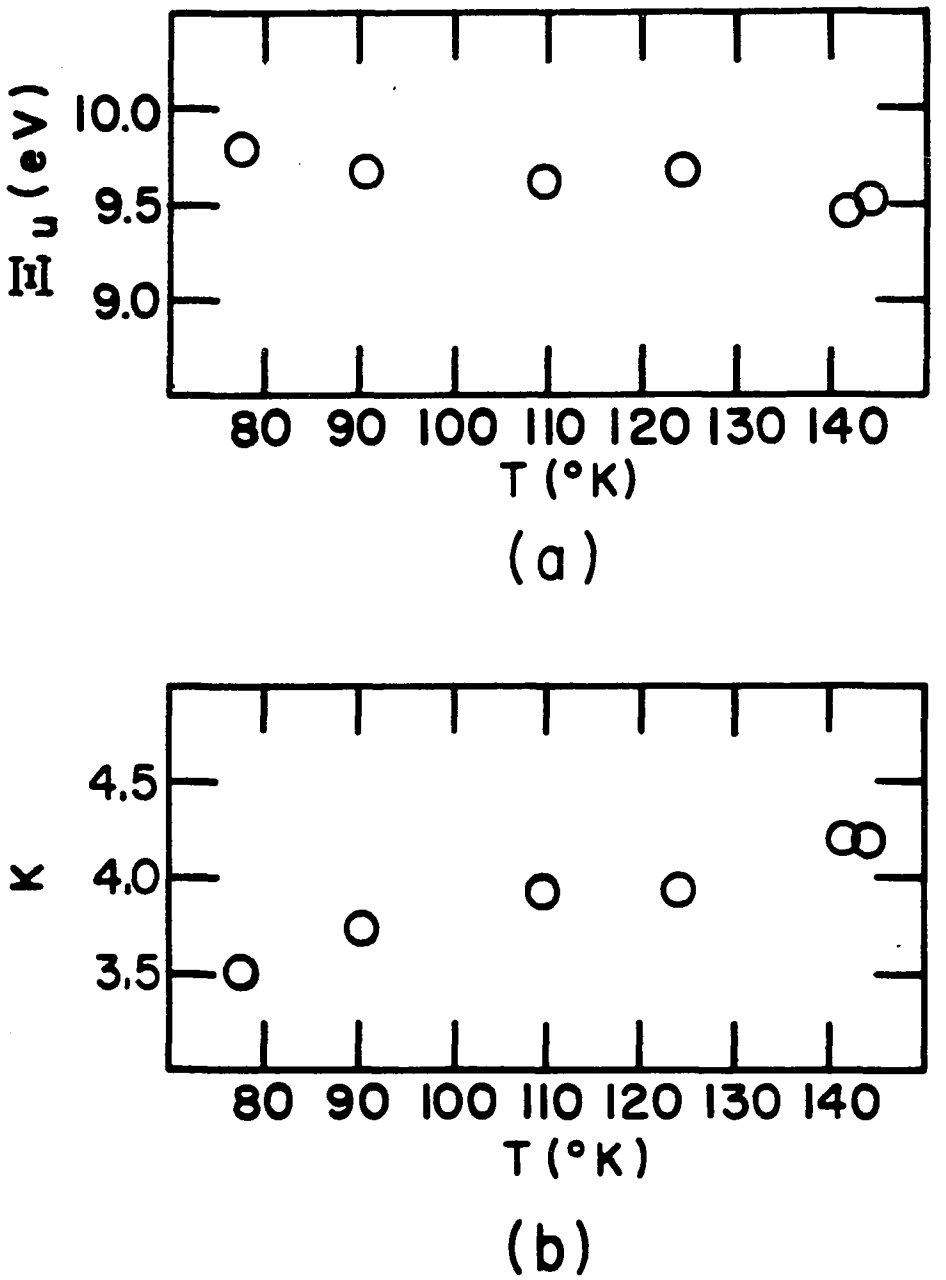

Figure 32. Temperature dependence of the deformation potential (a) as determined with the use of the mobility anisotropy (b) found by Umeda.

though it is true that the value of π_{11} is more reliable than the value of π_{12}. Figure 32a shows the temperature dependence of the deformation potential. The dependence of Ξ_u on T can be represented by the relation

$$\Xi_u = \Xi_u^o (1 + \alpha T) \text{ where } \Xi_u^o = 10.1 \text{ ev and } \alpha = (-4.3 \pm 0.6) \times 10^{-4} \, {}^oK^{-1} .$$

Table 11. The deformation potential calculated from a combination of the present piezoresistance data and the magnetoresistance data of Umeda (74).

T (^oK)	K^a ($\mu_\perp/\mu_\parallel$)	Ξ_u from m_{11} (ev)	Ξ_u from m_{12} (ev)	Ξ_u average (ev)
77.4	3.51	9.74	9.98	9.86
90.2	3.74	9.75	9.59	9.67
109.7	3.94	9.76	9.46	9.61
124.1	3.94	9.81	9.56	9.69
141.6	4.21	9.50	9.44	9.47
144.0	4.20	9.55	9.49	9.52

[a]From the magnetoresistance measurements of Umeda (74).

An attempt was also made to determine an independent value for the mobility anisotropy and the deformation potential by extending the piezoresistance measurements to high stress. The high stress results at T = 77.4°K and 50°K are given in Figs. 33 and 34 respectively. The solid curve in Fig. 33 shows the expected result based on Eqn. 83 with Ξ_u = 9.8 ev and K = 3.51. The dashed curve shows the best

Figure 33. Results of high stress piezoresistance measurements on Mg_2Sn at 77.4°K. The solid line indicates the expected result based on Eqn. 83 with Ξ_u = 9.8 ev and K = 3.51. The dashed curve shows the best fit to experimental data with Ξ_u = 18 ev and K = 2.65.

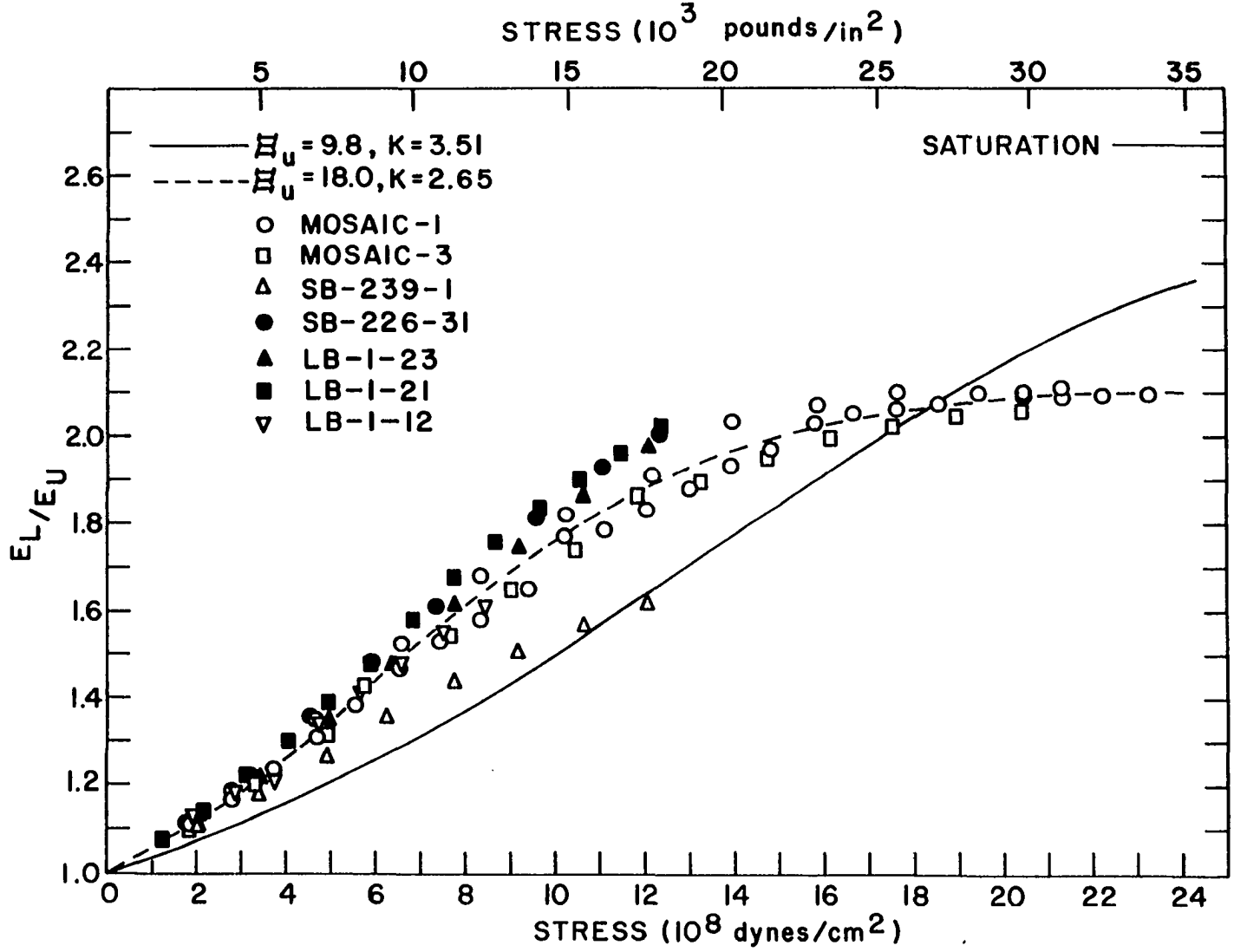
STRESS (10^3 pounds/in^2)
5
10
15
20
25
30
35
Ξ_u = 9.8, K = 3.51
Ξ_u = 18.0, K = 2.65
SATURATION
MOSAIC-1
MOSAIC-3
SB-239-1
SB-226-31
LB-1-23
LB-1-21
LB-1-12
E_L/E_U
2.6
2.4
2.2
2.0
1.8
1.6
1.4
1.2
1.0
0
2
4
6
8
10
12
14
16
18
20
22
24
STRESS (10^8 dynes/cm^2)

Figure 34. Result of a high stress piezoresistance measurement on sample mosaic-1 at 50°K. The solid line indicates the expected result based on Eqn. 83 with Ξ_u = 9.92 ev and K = 3.21. The dashed curve shows the best fit to experimental data with Ξ_u = 18 ev and K = 2.50.

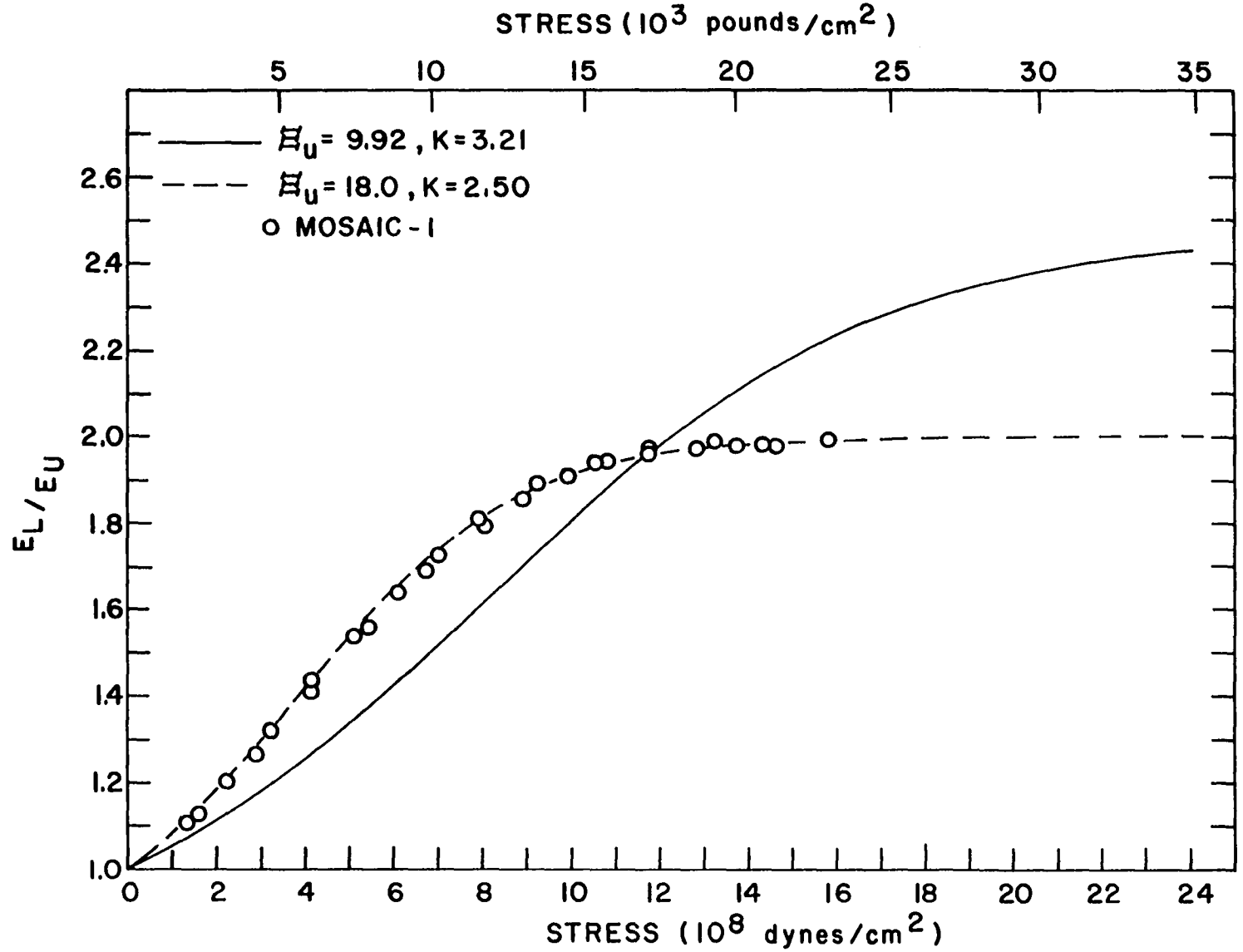
STRESS (10^3 pounds/cm^2)
5
10
15
20
25
30
35
Ξ_u = 9.92 , K = 3.21
Ξ_u = 18.0 , K = 2.50
o MOSAIC - I
E_L / E_U
2.6
2.4
2.2
2.0
1.8
1.6
1.4
1.2
1.0
0
2
4
6
8
10
12
14
16
18
20
22
24
STRESS (10^8 dynes/cm^2)

fit to experimental data with Ξ_u = 18 ev and K = 2.65. In Fig. 34 the solid curve was obtained with Ξ_u = 9.92 ev and K = 3.21, while the dashed curve shows the best fit to experimental data with Ξ_u = 18 ev and K = 2.50. Table 15 (Appendix) shows the high stress results for sample mosaic-1 at 77.4 and 50.0°K. The high stress results were obtained from longitudinal measurements on [100] oriented samples.

Single crystals of Mg_2Sn broke at $X = 12.5 \times 10^8$ dynes/cm^2. The breaking point was independent of sample cross section. The mosaic samples did not break until $X = 24 \times 10^8$ dynes/cm^2. As a result, there is no data for single crystal samples in the saturation region.

D. Deformation Potential Discussion

An indication that the deformation potential determined from the combination of piezoresistance and magnetoresistance measurements (Ξ_u = 9.86 ev at 77.4°K) is a more reliable value than that obtained from the high stress measurements (Ξ_u = 18 ev at 77.4°K) is given by the thermal conductivity measurements of Martin (46). Martin determined that an approximate value of Ξ_u = 10.3 ev helped give a best fit of his experimental values to theory.

Another indication that the deformation potential value of 9.86 ev is more reliable than Ξ_u = 18 ev is given by a comparison with the piezoresistance results obtained from silicon. Aubrey *et al.* (2) obtained Ξ_u = 8.3 ev for silicon

and Tufte and Stelzer (69) found K to be 5.0 for their silicon samples with a carrier concentration of 10^{16} carriers/cm^3. From the piezoresistance measurements of Morin et al. (48), an approximate value for the elastoresistance coefficients of silicon can be determined. Table 12 shows a comparison of the elastoresistance tensor component m_{11} of Mg_2Sn with m_{11} of Si at three different temperatures. Even though the piezoresistance tensor component π_{11} for Mg_2Sn is larger than π_{11} for Si, the elastoresistance tensor component m_{11} is approximately the same for both Mg_2Sn and Si. If m_{11} is the same for both materials, then the factor $\Xi_u(1 - K)/(1 + 2K)$ should also be the same for both materials. With the value $\Xi_u = 9.86$ ev and K = 3.51, $\Xi_u(1 - K)/(1 + 2K) = -3.09$ for Mg_2Sn, while $\Xi_u(1 - K)/(1 + 2K) = -3.02$ for Si. However, if we use $\Xi_u = 18$ ev and K 2.65, $\Xi_u(1 - K)/(1 + 2K) = -4.7$ for Mg_2Sn. Thus, we are lead to the conclusion that the deformation potential results presented in Fig. 32a and Table 11 are more reliable than the results obtained from the high stress measurements and that the value $\Xi_u = 9.86$ ev at 77.4°K is an accurate deformation potential for Mg_2Sn.

The temperature dependence of the deformation potential in Mg_2Sn ($\alpha = -4 \times 10^{-4}\ ^{o}K^{-1}$) is of the same order magnitude as was found in Si ($\alpha = 14 \times 10^{-4}\ ^{o}K^{-1}$) by Tufte and Stelzer (69), in Ge ($\alpha = -6 \times 10^{-4}\ ^{o}K^{-1}$) by Fritzsche (17) and AlSb ($\alpha = 10 \times 10^{-4}\ ^{o}K^{-1}$) by Ghaneker and Sladek (20). The

deformation potential for Mg_2Sn is greater than the deformation potential found in Si(Ξ_u = 8.3 ev)by Aubrey et al. (2) and less than the deformation potential found in Ge(Ξ_u = 19.2 ev) by Fritzsche (17).

Table 12. Comparison of the elastoresistance tensor component m_{11} of Mg_2Sn with m_{11} of Si at three different temperatures

T (^oK)	m_{11} from Si[a]	m_{11} from Mg_2Sn
66.7	350	350
80.0	303	297
100.0	247	247

[a]Determined from the piezoresistance data of Morin et al. (48).

At both 77.4 and 50^{o}K the high stress piezoresistance experimental results deviate from the expected result. There are several factors which could account for this deviation.

In the derivation of Eqn. 83 it was assumed that neither the relaxation time nor the effective mass changed under an applied stress. However, under large strains, the lattice constant of the crystal is changed, which would change the lattice vibrations, and thus change the relaxation time. In addition, energy ellipsoids could be warped, which would change the effective mass matrix. Also any strain inhomogeneities in the sample would create unknown strains which

could change the relaxation time.

Probably the most important factor which would account for the observed discrepancy is a shift of a valley band-edge point below a donor level. If this occurs it is possible to have a transfer of electrons not only between valleys, but also between valleys and donor levels.

The difference in energy of valley band-edge points under applied stress is given by Eqn. 73,

$$\delta \epsilon = \chi(S_{11} - S_{12}) \Xi_u \ . \qquad (73)$$

With $\Xi_u = 9.8$ ev and $\chi = 10^8$ dynes/cm^2 (smallest stress shown in Figs. 33 and 34), $\delta \epsilon = 1 \times 10^{-3}$ ev. Martin (46) measured the Hall coefficient on one of his Mg_2Sn samples down to 10°K and determined that the donor level in his samples was approximately 1.3×10^{-3} ev below the conduction band. Since our samples were prepared in the same manner and from the same lots of Mg and Sn, it is reasonable to assume that the donor level in our samples is the same. Thus at $\chi = 10^8$ dynes/cm^2 the lower valley band-edge point is at approximately the same energy as the donor level of the upper valley. Kohn and Luttinger (41) show that the donor level has the same symmetry as the conduction band. Kohn (40) shows that the donor level would be lowered under an applied stress, but the downward shift is quadratic and not linear. At $\chi = 10^8$ dynes/cm^2 the donor level is not shifted an appreciable amount. As the stress is increased both the donor level of the upper valley

and the lower valley band-edge point are shifted downward, with the valley band-edge point being shifted downward at a faster rate. Thus, in the stress region shown in Figs. 33 and 34 it is conceivable that the energy of the lower valley band-edge point is $\leq$ the donor energy level associated with the upper valley. There would then be an appreciable interchange of electrons between the lower valley and the donor level. Those electrons transferred into the donor level would be lost to the conduction process. Thus the resistivity would be increased more than expected when a stress was applied to the sample. So, the larger observed magnitude of E_L/E_u could be explained by a transfer of electrons between valleys and donor levels.

The above reasoning could also explain why the samples saturated at a smaller value of χ than expected. In the ideal case (no donor levels) the relative levels of the band-edges would have to be separated by an amount $>>kT$ to effectively empty the upper valley. However, if donor levels are present there is a large reservoir of empty sites which could accept electrons from the upper valley. Thus the upper valley would be emptied (saturation condition) at a smaller stress than expected.

In view of the above arguments two questions come to mind. The first question is; does this transfer of electrons from the upper valley to the donor level affect the validity

of the low stress piezoresistance results? This question can be answered by looking at the E_L/E_u values at low stress. Equation 83 predicts that for $\chi = 5 \times 10^7$ dynes/cm^2 (pressure employed for the low stress results) E_L/E_u should be 1.022. The ratio E_L/E_u for the samples used to determine π_{11} was 1.025. This discrepancy in E_L/E_u would give an error in $\Delta\rho/\rho\chi$ of less than 2%, which is within the measured error discussed in section VII. B. Thus the answer to the first question would have to be that a transfer of electrons from the upper valley to the donor level would not affect the low stress piezoresistance results.

The second question is; why can high stress piezoresistance measurements be used to obtain reliable values for the deformation potential in Si when it appears that it cannot be used to obtain reliable values of the deformation potential in Mg_2Sn? This question can be answered by looking at the location of the donor levels in Si. The donor levels in Si are at least 35×10^{-3} ev below the conduction band [see Kohn and Luttinger (41)]. A stress of 6×10^9 dynes/cm^2 [highest stress used in the high stress piezoresistance measurements in Si by Aubrey et al. (2)] produces a separation in energy between the upper and lower valleys of 25×10^{-3} ev. Thus the donor level of the upper valley would be 10×10^{-3} ev below the band-edge point of the lower valley, regardless of how much the donor level is shifted downward. The answer to

the second question is that the donor levels in Si are low enough so that there is a negligible transfer of electrons from the upper valley to the donor level.

Cuevas and Fritzsche (10) point out that the saturation value of E_L/E_u would yield the mobility anisotropy if the total carrier concentration remained unchanged by the application of stress. From the argument presented, this condition is probably violated in Mg_2Sn. Thus we should not expect the saturation value of E_L/E_u to give a valid mobility anisotropy.

As mentioned earlier, the effect of pressure on mobility has been neglected. However, a change in $\mu_{\parallel}$ or $\mu_{\perp}$ by 30% would be enough to reduce the mobility anisotropy from the expected 3.51 to the observed 2.65. So, a change in mobility with pressure could account for the smaller than expected saturation value observed in Figs. 33 and 34.

Another possible explanation of the difference in saturation value can be given if the samples were degenerate at high stress. However, for a semiconductor to be degenerate the Fermi temperature, T_F, should be approximately the same (say within a factor of two) as the temperature at which the measurements are made. The Fermi temperature is defined by $T_F = \epsilon_F(0)/k$, where $\epsilon_F(0)$ is the Fermi level at $0^{\circ}K$. An approximation of the Fermi level can be obtained if it is assumed that the donor levels are completely ionized. The free electron model [see Kittel p. 249 (38)] can then be used

to find $\epsilon_{F(0)}$,

$$\epsilon_F(0) = \frac{h^2}{2m}\left(\frac{3n}{8\pi}\right)^{2/3},$$

where h is Planck's constant, m the electron effective mass and n the density of charge carriers. For our samples, the unstrained Hall coefficient gave $n = 5 \times 10^{16}$ carriers/cm^3 which in turn gave $T_F = 6^oK$. Thus, it appears that at 77.4 and 50^{o}K the samples were non-degenerate. However, in the saturation region, the applied stress may have been great enough to cause additional electrons to be excited from deep donor levels into the conduction band. Also there could have been electrons trapped at impurity sites which, upon application of a high stress, entered the conduction band. An interesting comparison with the magnetoresistance work of Umeda (74) can be made. At 77.4^{o}K Umeda determined a K of 2.8 for his Mg_2Sn sample with 9×10^{17} carriers/cm^3. With a charge carrier density of 9×10^{17} carriers/cm^3 the Fermi temperature would be 45^{o}K. Thus, Umeda's sample was nearly degenerate. If our samples acquired an electron concentration of about 9×10^{17} carriers/cm^3 upon the application of a large stress (greater than 10^9 dynes/cm^2), Umeda's results would apply and we should have a mobility anisotropy of K = 2.8. For the saturation value shown in Fig. 33, a value of K = 2.65 (within six per cent of Umeda's value) was obtained. Thus, there would be agreement with Umeda if our samples did

in fact acquire a large number of additional charge carriers at high stress.

In conclusion, it is felt that the deformation potential obtained from a combination of piezoresistance and magnetoresistance measurements is a reliable value for Mg_2Sn. An interpretation of the high stress piezoresistance results is difficult because of the possibility of a transfer of electrons from donor levels and traps to the conduction band.

IX. CONCLUSIONS

The piezoresistance tensor components π_{11}, π_{12} and π_{44} have been measured for n-type Mg_2Sn in the temperature range 50-300°K. The component π_{11} is larger than that reported for other semiconducting materials.

A comparison of the experimentally observed quantities $\frac{1}{2}(\pi_{11} + \pi_{12} - \pi_{44})$ and $1/3\ (\pi_{11} + 2\pi_{12} + 2\pi_{44})$ with the values calculated from π_{11}, π_{12} and π_{44} showed that the piezoresistance measurements were internally consistent.

The elastoresistance tensor components have been determined and found to satisfy $m_{11} = -2m_{12}$, m_{44} small and m_{11} large, in the temperature range 50-200°K. These relationships between the elastoresistance tensor components confirm that n-type Mg_2Sn is a many-valley semiconductor with constant energy ellipsoids in the <100> direction.

The fact that m_{11} and m_{12} were both linear in the temperature range 60-175°K indicates that inter-valley scattering is unimportant in the extrinsic temperature region.

The small value of the volume coefficient, $(m_{11} + 2m_{12})/3$, indicates that carrier mobility in n-type Mg_2Sn is relatively insensitive to changes in sample volume.

The deformation potential was determined from a combination of these piezoresistance results and the magnetoresistance data of Umeda (74) and found to satisfy the relation $\Xi_u = \Xi_u^o(1+ \alpha T)$, where $\Xi_u^o = 10.1$ ev and $\alpha = (-4.3 \pm 0.6)$ x

10^{-4} $^{o}K^{-1}$. The temperature dependence, α, is of the same order magnitude as found in silicon, germanium and aluminum antimonide and of the same sign as that found in germanium, but of opposite sign to that observed in aluminum antimonide and silicon.

High stress piezoresistance measurements yielded a deformation potential of Ξ_u = 18 ev and a mobility anisotropy K = 2.65 at 77.4°K. Umeda (74) obtained K = 3.51. A qualitative explanation of the difference between the conflicting values for the deformation potential and mobility anisotropy is given. It appears, however, that effects which are unimportant at low stress become significant at high stress. At present, these effects are not well enough understood to permit a quantitative interpretation of the high stress piezoresistance data.

To better understand the high stress piezoresistance results, piezo-Hall-magnetoresistance measurements should be made on Mg_2Sn. If the Hall coefficient was measured as a function of stress it should be possible to determine the number of electrons in the conduction band as a function of stress. If magnetoresistance was measured as a function of stress, it should be possible to determine the mobility anisotropy, K, as a function of stress.

Cyclotron resonance measurements should be made on Mg_2Sn to determine $m_{\parallel}^{*}$ and $m_{\perp}^{*}$. If the effective masses were

known the relaxation time ratio, $\tau_{\parallel} / \tau_{\perp}$, could be determined and values for $\tau_{\parallel}$ and $\tau_{\perp}$ calculated. It would then be possible to calculate the transport properties and compare the results with experiment. Even though it is true that good cyclotron resonance measurements require higher purity crystals than are now available for Mg_2Sn, measurements on crystals with carrier concentrations of 10^{16} carriers/cm^3 would give an approximation to $m_{\parallel}^*$ and $m_{\perp}^*$.

X. LITERATURE CITED

1. Abeles, B. and Meiboom, S. Theory of the galvonomagnetic effects in germanium. Phys. Rev. 95:31. 1954.

2. Aubrey, J. E., Gubler, W., Henningsen, T. and Koenig, S. H. Piezoresistance and piezo-Hall-effect in n-type silicon. Phys. Rev. 130:1667. 1963.

3. Bardeen, J. and Shockley, W. Deformation potentials and mobilities in non-polar crystals. Phys. Rev. 80:72. 1950.

4. Bercha, D. M., Pankevich, Z. V., Savitskii, A. V. and Toustyuk, K. D. Piezoresistance of Sb_2Te_3 (translated title). Fiz. Tverd. Tela 7:2437. 1965. Original available but not translated; translated in Soviet Physics-Solid State 7:1968. 1966.

5. Bir, G. L., Bagomolov, V. N., Krivitskii, E. V. and Sulyatitskaya, T. E. Piezoresistivity in partially reduced rutile in temperature range 78-500°K. (translated title). Fiz. Tverd. Tela 7:2978. 1966. Original available but not translated; translated in Soviet Physics - Solid State 7:2414. 1966.

6. Blunt, R. F., Frederikse, H. P. R. and Hosler, W. R. Electrical and optical properties of intermetallic compounds. IV. Magnesium stannide. Phys. Rev. 100:663. 1955.

7. Boltaks, B. I. The electrical properties of the intermetallic compound Mg_2Sn (in Russian, translated title). Z. Tek. Fiz. 20:180. 1950.

8. Burns, F. P. and Fleischer, A. A. Piezoresistance in indium antimonide. Phys. Rev. 107:1281. 1957.

9. Busch, G and Schneider, M. Heat conduction in semiconductors. Physica 20:1084. 1954.

10. Cuevas, M. and Fritzsche, H. High stress piezoresistance and mobility in degenerate Sb-doped germanium. Phys. Rev. 137:A1847. 1965.

11. Cuevas, M. and Fritzsche, H. High stress piezoresistance in arsenic-doped germanium. Phys. Rev. 139:A1628. 1965.

12. Davis, L. C., Whitten, W. B. and Danielson, G. C. Elastic constants and calculated lattice vibration frequencies of Mg_2Sn. J. Phys. Chem. Solids 28:439. 1967.

13. Drabble, J. R. and Wolfe, R. Anisotropic galvanomagnetic effects in semiconductors. Proc. Phys. Soc. B69:1101. 1956.

14. Dumke, W. P. Deformation potential theory for n-type germanium. Phys. Rev. 101:531. 1956.

15. Finlayson, D. M. and Stewart, A. D. Piezoresistance measurements on n-type lead sulphide. Brit. J. Appl. Phys. 17:737. 1966.

16. Frederikse, H. P. R., Hosler, W. R. and Roberts, D. E. Electrical conduction in magnesium stannide at low temperatures. Phys. Rev. 103:67. 1955.

17. Fritzsche, H. Piezoresistance of n-type Ge. Phys. Rev. 115:336. 1959.

18. Fritzsche, H. The use of pressure in the study of impurity states in semiconductors. In Tomizuka, C. T. and Emrick, R. M., eds. Physics of solids at high pressures. pp. 184-195. New York, New York, Academic Press, Inc. 1965.

19. Geick, R., Habel, W. J. and Perry, C. H. Temperature dependence of the far-infrared reflectivity of magnesium stannide. Phys. Rev. 148:824. 1966.

20. Ghanekar, K. M. and Sladek, R. J. Piezoresistance in n and p-type aluminum antimonide. Phys. Rev. 146:505. 1966.

21. Herring, C. Transport properties of a many-valley semiconductor. Bell System Tech. J. 34:237. 1955.

22. Herring, C. and Vogt, E. Transport and deformation potential theory for many-valley semiconductors with anisotropic scattering. Phys. Rev. 101:944. 1956.

23. Hollander, L. E., Jr. and Diesel, T. J. Piezoresistance effect in p-type PbTe. J. Appl. Phys. 31:692. 1960.

24. Hallander, L. E., Jr., Diesel, T. J. and Vick, G. L. Piezoresistivity in the oxide semiconductor rutile (TiO_3). Phys. Rev. 117:1469. 1960.

25. Ilisavskii, Yu. V. Effect of uniaxial deformation on the electrical conductivity of bismuth telluride (Bi_2Te_3) and bismuth selenide (Bi_2Se_3) (translated title). Fiz. Tverd. Tela 4:818. 1962. Original available but not translated; translated in Soviet Physics-Solid State 4:601. 1962.

26. Ilisavskii, Yu. V. The piezoresistance effect in PbTe and PbSe (translated title). Fiz. Tverd. Tela. 4:918. 1962. Original available but not translated; translated in Soviet Physics-Solid State 4:674. 1962.

27. Ito, R. and Shagenji, K. Temperature dependence of piezoresistance in p-type PbTe. J. Phys. Soc. Japan 18:1343. 1963.

28. Jelinek, F. J., Shickell, W. D. and Gerstein, B. C. Thermal study of group II-IV semiconductors. II. Heat capacity of Mg_2Sn in the range 5-300°K. J. Phys. Chem. Solids 28:267. 1967.

29. Kaiser, K. B. and Kearney, R. J. Piezoresistance in p-type Mg_2Sn. Phys. Rev. (To be published) ca. 1967.

30. Katz, M. J. Piezoresistance in degenerate n-type germanium. Helv. Phys. Acta (Switzerland) 35:511. 1962.

31. Katz, M. J. Temperature and stress dependence in heavily doped n-type Ge. Phys. Rev. 140:A1323. 1965.

32. Kawasaki, T., Ishiguro, T. and Tanaka, T. Anisotropic piezoresistance of cadmium antitmonide. Japan J. Appl. Phys. 3:172. 1964.

33. Keyes, R. W. The effects of elastic deformation on the electrical conductivity of semiconductors. Solid State Physics 11:149. 1960.

34. Keyes, R. W. Elastoresistance in multivalley semiconductors with an axis of symmetry. J. Electronics 2: 279. 1956.

35. Keyes, R. W. Temperature dependence of the elastoresistance in n-type germanium. Phys. Rev. 100:1104. 1955.

36. Keyes, R. W. and Pollak, M. Hydrostatic pressure for piezoresistance. Phys. Rev. 118:1001. 1960.

37. Kittel, C. Experimental evidence on the band structure of germanium and silicon. Physica 20:829. 1954.

38. Kittel, C. Introduction to solid state physics. 2nd ed. New York, New York, John Wiley and Sons, Inc. 1956.

39. Koenig, S. H. Piezoresistance in n-type germanium. International School of Physics (Enrico Fermi) 22:515. 1963.

40. Kohn, W. Shallow impurity states in silicon and germanium. Solid State Physics 5:257. 1957.

41. Kohn, W. and Luttinger, J. M. Theory of donor states in silicon. Phys. Rev. 98:915. 1955.

42. Lawson, W. D., Nielsen, S., Putting, E. H. and Roberts, V. The preparation, electrical and optical properties of Mg_2Sn. J. Electronics 1:203. 1955.

43. Lichter, B. D. Electrical properties of Mg_2Sn crystals grown from nonstoichiometric melts. J. Electrochem. Soc. 109:819. 1962.

44. Lipson, H. G. and Kahan, A. Infrared absorption of magnesium stannide. Phys. Rev. 133:A800. 1964.

45. McWilliams, D. and Lynch, D. W. Infrared reflectivities of magnesium silicide, germanide and stannide. Phys. Rev. 130:2248. 1963.

46. Martin, J. J. Thermal conductivity of magnesium stannide. Unpublished Ph.D. thesis. Ames, Iowa, Library, Iowa State University of Science and Technology. 1967.

47. Mason, W. P. and Thurston, R. N. Use of piezoresistive materials in the measurement of displacement, force and torque. J. Acoustic. Soc. 29: 1096. 1959.

48. Morin, F. J., Geballe, T. H. and Herring, C. Temperature dependence of the piezoresistance of high-purity silicon and germanium. Phys. Rev. 105:525. 1957.

49. Morris, R. G., Redin, R. D. and Danielson, G. C. Semiconducting properties of Mg_2Si single crystals. Phys. Rev. 109:1909. 1958.

50. Nelson, J. T. Electrical and optical properties of Mg_2Sn and Mg_2Si. Bull. A. Phys. Soc. 23:390. 1955.

51. Pfann, W. G. and Thurston, R. N. Semiconducting stress transducers utilizing the transverse and shear piezoresistance effects. J. Appl. Phys. 32:2008. 1961.

52. Pollak, M. Piezoresistance of heavily doped n-type germanium. Phys. Rev. 111:798. 1958.

53. Potter, R. F. Piezoresistance of indium antimonide. Phys. Rev. 108:652. 1957.

54. Potter, R. F. and McKean, W. J. An apparatus for measuring the piezoresistivity of semiconductors. J. Res. Nat. Bur. Stand. 59:427. 1957.

55. Powell, R. L., Bunch, M. D. and Corruccini, R. J. Low temperature thermocouples-1, gold-cobalt or constantan versus copper or "normal" sliver. Cryogenics 1:1. 1961.

56. Sagar, A. Piezoresistance in GaSb. Phys. Rev. 117:93. 1960.

57. Sagar, A. Piezoresistance in InP. Phys. Rev. 117:101. 1960.

58. Sagar, A. Piezoresistance of n-type GaAs. Phys. Rev. 112:1533. 1958.

59. Sagar, A. and Lehnann, W. Piezoresistance in p-type ZnTe. Phys. Rev. 140:A923. 1965.

60. Sagar, A. and Rubenstein, M. Piezoresistance in n-type CdTe. Phys. Rev. 143:522. 1966.

61. Savitskii, A. V. and Pankevich, Z. V. Peizoresistance in p-ZnTe (translated title). Fiz. Tverd. Tela 7:315. 1965. Original available but not translated; translated in Soviet Physics-Solid State 7:252. 1965.

62. Sladek, R. J. Effect of stress on the electrical properties of n-type gallium arsenide. Phys. Rev. 140: A1345. 1965.

63. Smith, C. S. Macroscopic symmetry and properties of crystals. Solid State Physics 6:175. 1958.

64. Smith, C. S. Piezoresistance effect in germanium and silicon. Phys. Rev. 94:42. 1954.

65. Sugigama, K. and Kobayashi, A. Piezoresistance in n-type germanium at low temperature. J. Phys. Soc. Japan 17:574. 1962.

66. Swanson, H. E., Gilfrich, N. T. and Ugrinic, G. M. X-ray diffraction powder patterns. National Bureau of Standards Circular 539, Vol. 5:41. 1955.

67. Temple, P. A. Measurement of piezoresistance in semiconductors. Unpublished M.S. thesis. Ames, Iowa, Library, Iowa State University of Science and Technology. 1965.

68. Tovstyuk, K. D., Bercha, D. M., Pankevich, Z. V. and Rarenko, I. M. Piezoresistance in cadmium antimonide. Phys. Status Solidi (Germany) 13:207. 1966

69. Tufte, D. N. and Stelzer, E. L. Piezoresistance in heavily doped n-type silicon. Phys. Rev. 133:A1705. 1964.

70. Tufte, D. N. and Stelzer, E. L. Piezoresistance in p-type gallium antimonide. Phys. Rev. 133:A1450. 1964.

71. Tufte, D. N. and Stelzer, E. L. Piezoresistive properties of reduced strontium titanate. Phys. Rev. 141:678. 1966.

72. Tuzzolino, A. J. Piezoresistance constants of p-type InSb. Phys. Rev. 109:1980. 1958.

73. Tuzzolino, A. J. Piezoresistance of n-type InAs. Phys. Rev. 112:30. 1958.

74. Umeda, Jun-ichi. Galvanomagnetic effects in magnesium stannide Mg_2Sn. J. Phys. Soc. Japan 19:2052. 1964.

75. Whitten, W. B. and Danielson, G. C. Piezoresistance of n-type Mg_2Si. International Conference on the Physics of Semiconductors, Paris, Proceedings 7:537. 1964.

76. Winkler, U. Die elektrischen Engenschaften der intermetallischen Verbindungen Mg_2Si, Mg_2Ge, Mg_2Sn und Mg_2Pb. Helv. Phys. Acta 28:633. 1955.

77. Ziman, J. M. Electrons and phonons. London, England, Oxford Press. 1960.

XI. ACKNOWLEDGMENTS

The author would like to thank Dr. G. C. Danielson for his guidance during this research. Thanks are extended to Mr. P. H. Sidles for his assistance in the design and construction of the apparatus and also for his counsel regarding measurement procedures. A special word of appreciation is extended to Mr. P. A. Temple for his close cooperation during the early experimental work. Mr. O. M. Sevde helped set up the experiment. Mr. D. H. Grotzky and Mr. P. A. Millis gave help in the preparation of the Mg_2Sn crystals. Thanks are extended to Dr. J. J. Martin for his suggestions during the preparation of this thesis.

XII. APPENDIX

Table 13. Sample piezoresistance experimental data. The table shows the piezoresistance results for a $(100)_\ell$ sample (SB-260-43), $(100)_t$ sample (LB-1-11), $(110)_\ell$ sample (SB-245-1), and $(111)_\ell$ sample (SB-246-1)

T (°K)	1000/T (°K)$^{-1}$	E 10^{-4} volts	ΔE (μv)	I (ma)	$\frac{\Delta\rho/\rho\chi}{10^{-11}}$ $\left(\frac{}{cm^2/dyne}\right)$	ρ (ohm-cm)
			Sample SB-260-43			
49.76	20.10	9.144	45.00	0.328	78.05	0.137
52.77	18.95	9.222	42.64	0.345	73.34	0.131
56.65	17.65	9.186	40.09	0.352	69.21	0.128
60.00	16.67	9.244	38.36	0.360	65.82	0.126
65.34	15.30	9.773	37.65	0.378	61.09	0.127
68.90	14.51	9.940	36.45	0.378	57.81	0.129
72.57	13.78	9.795	34.43	0.361	55.75	0.133
78.0	12.82	9.358	30.60	0.328	51.86	0.140
83.69	11.95	10.100	31.20	0.334	48.99	0.148
90.35	11.07	11.308	33.30	0.345	46.71	0.161
96.61	10.35	12.225	33.38	0.342	43.30	0.175
100.5	9.95	12.297	33.19	0.340	42.81	0.177
104.6	9.56	13.261	33.60	0.334	40.19	0.195
116.9	8.55	13.699	30.38	0.294	35.18	0.228
123.7	8.08	17.272	36.86	0.330	33.85	0.257
137.5	7.27	19.660	37.28	0.315	30.07	0.306
153.4	6.52	23.682	39.79	0.315	26.64	0.369
173.6	5.76	27.643	42.79	0.319	24.55	0.425
201.6	4.96	20.340	25.13	0.319	19.59	0.312
237.1	4.22	8.215	7.10	0.305	13.71	0.132
283.7	3.52	3.081	1.77	0.305	9.13	0.495
			Sample LB-1-11			
49.60	20.16	1.033	2.025	1.527	39.93	0.0607
50.83	19.67	1.023	1.969	1.527	36.26	0.0601
53.48	18.70	1.006	1.838	1.527	34.42	0.0591
57.02	17.54	1.027	1.759	1.572	32.28	0.0585
60.74	16.46	1.030	1.673	1.572	30.60	0.0587
65.13	15.35	1.047	1.586	1.572	28.54	0.0597
68.70	14.56	1.070	1.556	1.572	27.40	0.0610
74.07	13.50	1.115	1.523	1.572	25.73	0.0636
77.00	12.99	1.045	1.343	1.420	24.21	0.0660
82.92	12.06	1.104	1.217	1.420	22.92	0.0697
89.29	11.20	1.182	1.354	1.420	21.58	0.0746
97.36	10.27	1.024	1.091	1.120	20.09	0.0819

Table 13. (Continued)

T (°K)	1000/T (°K)-1	E 10^{-4} volts	ΔE (μv)	I (ma)	$\left(\frac{\Delta\rho/\rho X}{10^{-11}\ cm^2/dyne}\right)$	ρ (ohm-cm)
			Sample LB-1-11			
104.0	9.62	1.109	1.114	1.120	18.92	0.0887
113.7	8.80	1.255	1.163	1.120	17.46	0.100
124.9	8.01	2.032	1.744	1.573	16.17	0.116
138.1	7.24	2.099	1.620	1.371	14.54	0.137
151.6	6.60	2.018	1.428	1.120	13.33	0.161
168.7	5.93	3.013	1.856	1.421	11.61	0.190
194.1	5.15	3.275	1.440	1.421	8.28	0.206
235.1	4.25	1.146	0.216	0.900	3.56	0.114
297.3	3.36	0.3275	0.0213	0.816	1.22	0.036
			Sample SB-245-1			
50.67	19.74	2.083	1.835	0.20	20.02	0.0461
52.13	19.18	2.054	1.788	0.20	19.79	0.0455
55.27	18.09	2.025	1.698	0.20	19.06	0.0448
57.55	17.38	2.010	1.585	0.20	17.92	0.0445
59.68	16.76	2.009	1.563	0.20	17.68	0.0445
62.34	16.04	2.022	1.508	0.20	16.95	0.0448
65.00	15.38	2.043	1.505	0.20	16.95	0.0452
69.10	14.47	2.089	1.450	0.20	15.78	0.0463
73.37	13.63	2.172	1.440	0.20	15.07	0.0481
77.00	12.99	2.252	1.448	0.20	14.62	0.0499
79.33	12.61	2.363	1.472	0.20	14.16	0.0523
81.32	12.30	2.421	1.488	0.20	13.97	0.0536
85.19	11.74	2.543	1.525	0.20	13.63	0.0563
88.50	11.30	2.704	1.580	0.20	13.28	0.0599
94.79	10.55	2.956	1.653	0.20	12.71	0.0654
106.2	9.42	3.444	1.742	0.20	11.50	0.0760
116.7	8.57	4.007	1.903	0.20	10.79	0.0887
124.9	8.01	4.570	2.060	0.20	10.25	0.101
130.2	7.68	4.940	2.097	0.20	9.65	0.109
137.6	7.27	5.396	2.245	0.20	9.46	0.120
150.1	6.66	6.336	2.423	0.20	8.69	0.140
170.2	5.88	7.909	2.918	0.20	8.39	0.175
196.0	5.10	8.846	3.561	0.20	8.09	0.196
232.0	4.31	5.478	1.495	0.20	6.20	0.121
296.5	3.37	1.662	0.245	0.20	3.35	0.0368

Table 13. (Continued)

T (°K)	1000/T $(°K)^{-1}$	E 10^{-4} volts	ΔE (μv)	I (ma)	$\left(\frac{\Delta\rho/\rho\chi}{10^{-11}\ cm^2/dyne}\right)$	ρ (ohm-cm)
			Sample SB-246-1			
49.93	20.03	3.128	0.8044	0.306	5.72	0.0536
52.05	19.21	3.048	0.7538	0.306	5.50	0.0523
54.43	18.37	3.461	0.8063	0.358	5.18	0.0507
56.27	17.77	3.402	0.7331	0.358	4.80	0.0498
59.17	16.90	3.356	0.6944	0.358	4.64	0.0492
62.20	16.08	3.302	0.6394	0.358	4.31	0.0484
65.74	15.21	3.269	0.5925	0.358	4.03	0.0479
69.50	14.39	3.256	0.5588	0.358	3.82	0.0477
73.43	13.62	3.269	0.5400	0.358	3.68	0.0479
77.94	12.83	3.313	0.5269	0.358	3.54	0.0485
77.94	12.83	3.327	0.5400	0.358	3.61	0.0487
82.74	12.09	3.398	0.5194	0.358	3.40	0.0498
84.00	11.90	3.414	0.5413	0.358	3.53	0.0500
90.46	11.05	3.573	0.5050	0.358	3.14	0.0523
97.89	10.22	3.293	0.4781	0.305	3.23	0.0564
105.1	9.51	4.214	0.6094	0.357	3.22	0.0618
113.5	8.81	4.632	0.6900	0.357	3.31	0.0679
124.2	8.05	5.302	0.7894	0.357	3.31	0.0777
137.4	7.28	6.234	0.9244	0.357	3.30	0.0914
153.3	6.52	7.603	1.110	0.357	3.25	0.111
171.8	5.82	9.391	1.491	0.357	3.53	0.138
196.9	5.08	9.203	1.689	0.307	4.08	0.157
295.0	3.39	2.311	0.3381	0.356	3.26	0.0340

Table 14. Results of averaging procedure for the piezoresistance tensor components π_{11}, π_{12}, and $\frac{1}{2}(\pi_{11} + \pi_{12} + \pi_{44})$

1000/T $(^{o}K)^{-1}$	Intercepts of best fit curves with integral values of 1000/T (10^{-11} cm^2/dyne)				Average component (10^{-11} cm^2/dyne)
	Tensor component π_{11}				
	Sample SB-199-311	Sample SB-260-12	Sample SB-228-2	Sample SB-260-43	
20	70.10	73.50	75.3	77.80	74.18
19	67.70	69.90	72.15	74.20	70.99
18	65.25	66.55	69.05	70.60	67.86
17	62.85	63.25	65.90	67.05	65.01
16	59.90	59.90	62.75	63.45	61.50
15	56.50	56.45	59.70	59.85	58.13
14	53.10	52.55	56.50	56.25	54.60
13	49.70	48.70	52.65	52.65	50.93
12	46.25	45.40	48.85	49.05	47.39
11	42.95	42.10	45.05	46.00	44.03
10	39.50	38.70	41.25	42.00	40.36
9	36.15	35.35	37.45	37.65	36.65
8	32.75	30.95	33.60	33.30	32.65
7	28.40	25.70[a]	29.30	29.05	28.52
6	24.70	20.60[a]	24.80	25.25	24.92
5	21.45	15.60[a]	18.80	19.75	20.00
4	12.70	10.45[a]	12.60	12.55	12.62
3.4	7.40	7.60	8.30	8.90	8.05
	Tensor component π_{12}				
		Sample LB-1-22		Sample LB-1-11	
20		38.08		36.70	37.74
19		36.41		34.95	35.68
18		34.75		33.25	34.00
17		33.12		31.55	32.34
16		31.42		29.80	30.61
15		29.80		28.05	28.93
14		28.15		26.35	27.25
13		36.12		24.60	25.54
12		24.05		22.87	23.46
11		22.00		21.25	21.63
10		19.95		19.55	19.75
9		18.00		17.75	17.88
8		15.95		15.95	15.95

[a]Results not included in the average.

Table 14. (Continued)

1000/T (°K)-1	Intercepts of best fit curves with integral values of 1000/T (10^{-11} cm^2/dyne)			Average component (10^{-11} cm^2/dyne)
	Tensor component π_{12}			
		Sample LB-1-22	Sample LB-1-11	
7		13.92	14.10	14.01
6		11.40	11.72	11.56
5		7.18	7.50	7.62
4		3.20	3.00	3.10
3.4		2.10	1.65	1.88
	Tensor component $\frac{1}{2}(\pi_{11}+\pi_{12}+\pi_{44})$			
	Sample SB-245-5	Sample SB-245-1	Sample SB-245-4	
20	18.80	20.40	23.75	20.98
19	18.30	19.55	22.80	20.22
18	17.80	18.75	21.85	19.47
17	17.05	17.95	20.85	18.62
16	16.20	17.10	19.95	17.75
15	15.35	16.25	19.00	16.87
14	14.50	15.45	18.00	15.98
13	13.65	14.60	16.97	15.07
12	12.80	13.80	15.65	14.08
11	12.00	13.00	14.45	13.15
10	11.15	12.05	13.25	12.15
9	10.30	11.15	11.95	11.13
8	9.45	10.20	10.65	10.10
7	8.60	9.20	9.45	9.08
6	8.20	8.35	8.45	8.33
5	7.70	7.80	7.85	7.83
4	5.95	5.20	5.95	5.70
3.4	3.65	4.30	4.70	4.22

Table 15. Sample high stress piezoresistance data. The table shows the high stress results for sample mosaic - 1 at 77.4°K and 50.0°K

X (10^8 dynes/cm^2)	E_u (μv)	E (μv)	E_L/E_u
Sample mosaic - 1 at 77.4°K			
1.90	524.0	56.9	1.109
2.78	523.5	91.1	1.174
3.74	525.2	125.6	1.239
4.70	527.1	163.5	1.310
5.58	624.4	240.0	1.384
6.52	624.5	293.3	1.470
7.47	630.1	335.3	1.532
8.37	614.8	359.3	1.584
9.44	617.4	406.5	1.658
10.22	616.4	443.3	1.779
11.17	615.0	485.6	1.790
12.08	615.2	511.1	1.831
13.00	613.7	541.5	1.882
13.94	511.1	477.8	1.935
14.87	509.3	494.3	1.971
15.81	502.6	518.3	2.031
16.69	511.5	539.3	2.054
17.65	515.8	547.9	2.062
18.58	521.7	562.9	2.079
19.49	504.7	556.9	2.103
20.49	504.9	556.5	2.102
21.35	507.0	555.0	2.095
22.25	508.9	556.5	2.094
23.29	509.2	559.5	2.099
21.37	510.8	568.1	2.112
19.49	516.8	567.8	2.099
17.63	519.2	573.1	2.104
15.83	521.4	560.6	2.075
13.98	523.5	543.4	2.038
12.08	531.0	483.8	1.911
10.23	540.3	446.3	1.826
8.38	543.8	371.3	1.683
6.52	506.0	265.5	1.525
4.69	514.5	181.4	1.353
2.76	517.5	100.5	1.194

Table 15. (Continued)

χ (10^8 dynes/cm^2)	E_u (μv)	E (μv)	E_L/E_u
Sample mosaic - 1 at 50.0°K			
1.32	313.5	33.8	1.106
2.24	312.6	64.0	1.205
3.24	311.1	99.5	1.320
4.18	310.3	134.9	1.435
5.12	309.9	166.9	1.539
6.11	522.3	344.5	1.640
7.04	519.4	378.0	1.728
7.98	516.6	417.0	1.807
8.92	518.4	445.1	1.859
9.91	514.0	468.4	1.911
10.82	513.3	483.8	1.943
11.78	514.2	495.4	1.963
12.77	513.6	499.1	1.972
13.68	513.5	499.1	1.972
14.65	512.7	502.5	1.980
15.81	510.2	507.0	1.994
14.31	509.3	495.4	1.973
13.24	512.0	511.5	1.999
11.78	515.5	505.9	1.981
10.57	515.0	487.5	1.947
9.26	512.4	457.9	1.894
7.97	526.3	427.5	1.812
6.75	526.8	364.5	1.692
5.46	526.7	294.0	1.558
4.15	322.1	132.0	1.409
2.90	522.2	137.8	1.264
1.60	522.4	64.0	1.123